JACOBS
UNIVERSITY

SEA-ICE THICKNESS DERIVED FROM CRYOSAT-2: VALIDATION AND UNCERTAINTIES

by

Robert Ricker

A Thesis submitted in partial fulfillment of the
requirements for the degree of

Doctor of Philosophy in Geosciences

Approved, Dissertation Committee

Prof. Dr. Rüdiger Gerdes
Prof. Dr. Joachim Vogt
Dr. Stefan Hendricks
Dr. Veit Helm

Date of Defense: March 12, 2015

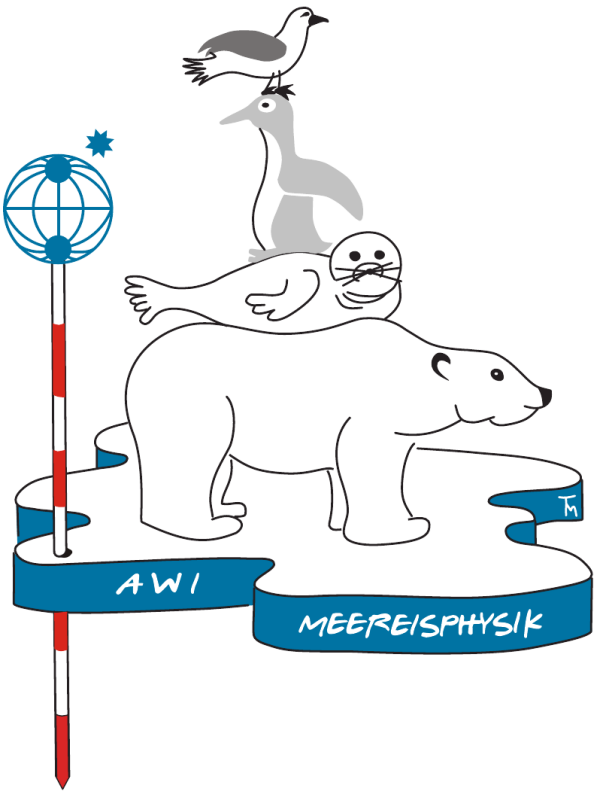
AWI
MEEREISPHYSIK

Abstract

Satellite altimetric measurements by the 2010 launched ESA satellite CryoSat-2 are capable of obtaining the thickness distribution of marine ice fields. With its on-board K_u-band radar altimeter we retrieve the sea-ice freeboard, the height of the ice surface above the actual sea level, and finally the thickness by assuming hydrostatic equilibrium. In this thesis I estimate CryoSat-2 Arctic sea-ice freeboard and thickness and their corresponding uncertainties. In particular I focus on the impact of different retracking algorithms that are used to retrieve CryoSat-2 range estimates. In recent studies, snow is considered as transparent for K_u-band frequencies, although a possible bias is acknowledged. Therefore, another goal of this work is to investigate the impact of snow coverage since it may affect the backscatter of the radar signal due to its physical properties. Likewise we use validation measurements from airborne laser altimetry, ice-mass balance buoys and in-situ drilling to evaluate CryoSat-2 sea-ice retrievals on both hemispheres. The findings show that random uncertainties are dominated by speckle noise and the density of leads along the flight track of the satellite. On the other hand, systematic uncertainties result from the choice of the retracking algorithm and in particular the echo power threshold which is used to determine the main scattering horizon. This bias is accompanied by systematic uncertainties due to scattering within the snow layer in conjunction with surface roughness effects. Moreover, we find observational evidence that CryoSat-2 freeboard increase correlates with snow accumulation events over Arctic multiyear ice, regardless of the used retracking algorithm. Such biases may lead to overestimated sea-ice thickness, as observed in autumn 2013 north of Canada. However, comparisons with airborne laser altimetry data, in-situ drilling measurements and other remote sensing sensors show that the freeboard and thickness retrieval represent the geographical distribution of sea-ice types. In the future, a data fusion with thickness retrievals from other past, present and future satellite sensors has the capability to reduce the uncertainty level and enables the prediction of long-term trends in sea-ice volume.

Contents

1 Introduction **1**

1.1 The role of sea ice in the climate system 1

1.2 Satellite altimetry over sea ice 4

1.2.1 Radar altimetry 6

1.2.2 CryoSat-2 - delay Doppler/SAR altimetry 8

1.2.3 Snow covered sea ice and its impact on radar altimetry 10

1.2.4 Validation activities 13

1.3 Scope of this work 15

1.4 Overview of papers 16

2 Classification of CryoSat-2 radar echoes **19**

2.1 Introduction 22

2.2 Methods 23

2.3 Results 25

2.4 Discussion 26

2.5 Conclusion 28

2.6 Acknowledgements 28

3 Sensitivity of CryoSat-2 Arctic sea-ice freeboard and thickness on radar-waveform interpretation **31**

3.1 Introduction 34

3.2 Data and methodology 36

3.2.1 Radar freeboard 36

3.2.1.1 Sea-surface anomaly 40

3.2.2 Sea-ice thickness 40

3.2.3 Uncertainty of freeboard and thickness 41

3.2.4 Gridding 44

3.2.5 Airborne data 45

3.3 Results 46

3.3.1 Radar freeboard retrieval 47

3.3.2 Comparison with airborne laser altimetry (ALS) 48

3.3.3 Freeboard and thickness from different retracker thresholds and uncertainties . . . 48
3.4 Discussion . . . 54
3.4.1 Differences between the retrievals of different thresholds . . . 54
3.4.2 Major increase of multiyear ice freeboard in November 2013 . . . 57
3.4.3 The retracking uncertainty in the context of the total uncertainty budget . . . 57
3.5 Conclusions . . . 59
3.6 Acknowledgements . . . 60

4 Impact of snow accumulation on CryoSat-2 range retrievals over Arctic sea ice: an observational approach with buoy data 61
4.1 Introduction . . . 64
4.2 Methods . . . 65
4.2.1 Ice and snow freeboard from ice mass balance buoys . . . 65
4.2.2 CryoSat-2 modal freeboard retrieval . . . 67
4.3 Results . . . 69
4.4 Discussion . . . 71
4.5 Conclusion . . . 74
4.6 Acknowledgments . . . 75
4.A Supporting Information . . . 75

5 Evaluation of CryoSat-2 derived sea ice freeboard over fast-ice in McMurdo Sound, Antarctica 79
5.1 Introduction . . . 82
5.2 CryoSat-2 assessment in McMurdo Sound . . . 86
5.2.1 In situ investigations . . . 86
5.2.2 CryoSat-2 . . . 88
5.3 Tracking surface height from CS-2 waveforms . . . 89
5.3.1 European Space Agency Level 2 data product (*ESAL2*) . . . 89
5.3.2 Waveform Fitting Procedure data product (*WfF*) . . . 89
5.3.3 Threshold-First-Maximum-Retracker-Algorithm 40 (*TFMRA40*) . 90
5.3.4 Tracking of sea surface height . . . 90
5.4 Supervised freeboard retrieval procedure . . . 91
5.4.1 Supervised freeboard retrieval results . . . 93
5.5 Automatic freeboard retrieval procedure . . . 99
5.5.1 *ESAL2* automatic SSH identification . . . 100
5.5.2 *WfF* automatic SSH identification . . . 102
5.5.3 *TFMRA40* automatic SSH identification . . . 103
5.5.4 Automatic results . . . 103

5.6 Discussion 107
5.7 Conclusion 111
5.8 Acknowledgements 111

6 Preliminary results and outlook **113**
6.1 Volume time series and combination with other satellite sea-ice thickness data 113
6.2 Radar altimetry/passive microwave synergy 114
6.3 Interpolation techniques 115
6.4 Validation of Antarctic CryoSat-2 freeboard and thickness retrievals . . . 117

7 Summary and concluding remarks **119**

List of Figures **123**

List of Tables **125**

Bibliography **127**

Acknowledgements **141**

Statutory Declaration **143**

Chapter 1

Introduction

This thesis is organized as follows: Chapter 1 gives an introduction to this thesis as well as methodical background information. Section 1.1 provides a brief overview of the field of research. In Section 1.2 it is considered how satellite altimetry and radar altimetry in particular are applied over sea ice. The objectives of this work are formulated in Section 1.3. Section 1.4 then outlines the papers that are presented in Chapters 2 – 5 and describes how they are linked. Preliminary results and an outlook for future work is given in Chapter 6. In Chapter 7 all findings from the papers are summarized and final conclusions are drawn.

1.1 The role of sea ice in the climate system

Sea ice is a prominent feature of the Earth's surface. During the annual maximum extent sea ice covers 5 % of the northern and even 8 % of the southern hemisphere (Lubin and Massom, 2006; Gloersen et al., 1993; Zwally et al., 1983). With its annual cycle of growth during winter season and decay during summer season, the sea ice reveals a seasonality that is very important for climatic as well as for ecological processes. This cycle represents one of the greatest cyclic changes on the Earth's surface. The Antarctic sea-ice extent reaches amplitudes of about $19 \times 10^6\,\mathrm{km}^2$ during September/October and $3.5 \times 10^6\,\mathrm{km}^2$ in February (Gloersen et al., 1993; Lubin and Massom, 2006). Whereas the Southern Ocean is not bounded by any continents, the Arctic Ocean is surrounded by the North American and Eurasian continent. The restriction of maximum sea-ice extent leads to a smaller factor of seasonal variability. The Arctic sea-ice cover varies from a maximum of approximately $15 \times 10^6\,\mathrm{km}^2$ in March to a minimum in September. Twenty years ago this minimum was about $7 \times 10^6\,\mathrm{km}^2$ (Parkinson and Cavalieri, 2002). As recent studies show, the Arctic sea ice extent is decreasing in the last decades and reached a new a record minimum of $3.4 \times 10^6\,\mathrm{km}^2$ for the satellite era in September 2012 (Comiso et al., 2008; Parkinson and Comiso, 2013).

Sea ice affects high latitude ocean-atmosphere interactions, biological, biogeochemical and sedimentological processes (Thomas and Dieckmann, 2010). Its impact is far-reaching and hence sea ice is a key component not only of the global cryosphere but also of the entire climate system (Goodison et al., 1999).

The capability of a surface to reflect radiation is called albedo and is an important factor in the Earth's energy budget. Dark surfaces like open water feature a low albedo. In contrast, sea ice features a high surface albedo, which is even increased if covered with snow. Hence, the high reflection coefficient keeps the amount of absorbed solar energy low. Thus, the sea-ice cover ensures that the polar regions remain colder than without ice cover. This process implies a positive feedback loop which is called ice albedo feedback, meaning that the decline of sea ice is self-compounding (Curry et al., 1995; Perovich, 1996; Perovich et al., 2002; Flanner et al., 2011).

Moreover, the polar regions act as an important component of ocean circulation. Shallow ocean currents transport warm water from the equator towards the Arctic where it cools down and the salinity increases due to ice formation. Hence, the water, while becoming denser, sinks down and leads to the formation of deep water masses, which is one of the main drivers of the process called thermohaline circulation (Aagaard and Carmack, 1989; Barry et al., 1993; Mauritzen and Häkkinen, 1997). Therefore changing ice freezing and melt rates could also affect the thermohaline circulation. The same holds for the heat exchange between ocean and atmosphere. Due to its low thermal conductivity, sea ice damps the heat transport from the warm ocean to the cold atmosphere in the winter season (Maykut, 1978, 1982). Along with the observed loss of sea-ice area during the last decades (Comiso et al., 2008; Comiso and Hall, 2014; Stroeve et al., 2012), more heat can escape to the atmosphere and thus affect the global circulation of the atmosphere (Budikova, 2009).

Sea ice is also a habitat of various plants and animals. It is a living environment for micro organisms like algae (Fernández-Méndez et al., 2014) as well as macro organisms such as penguins, seals and polar bears. For humans it is of fundamental importance as it is a platform for hunting and traveling. At the same time sea ice can be an obstacle for shipping, prospecting and extraction of natural resources from the Arctic sea floor (Gautier et al., 2009; Ho, 2010).

The observed reduction of the Arctic sea ice during the last decades may disturb and alter the processes that are maintained by the presence of sea ice (Serreze and Barry, 2011). On the other hand, vanishing sea ice also offers new possibilities for shipping routes and exploration of natural resources. Figure 1.1 shows the Arctic sea-ice extent in 2012 at the end of the winter season and at the end of the melting season with the record minimum in mid-September. At that time ice-free shipping along the North-East Passage was possible.

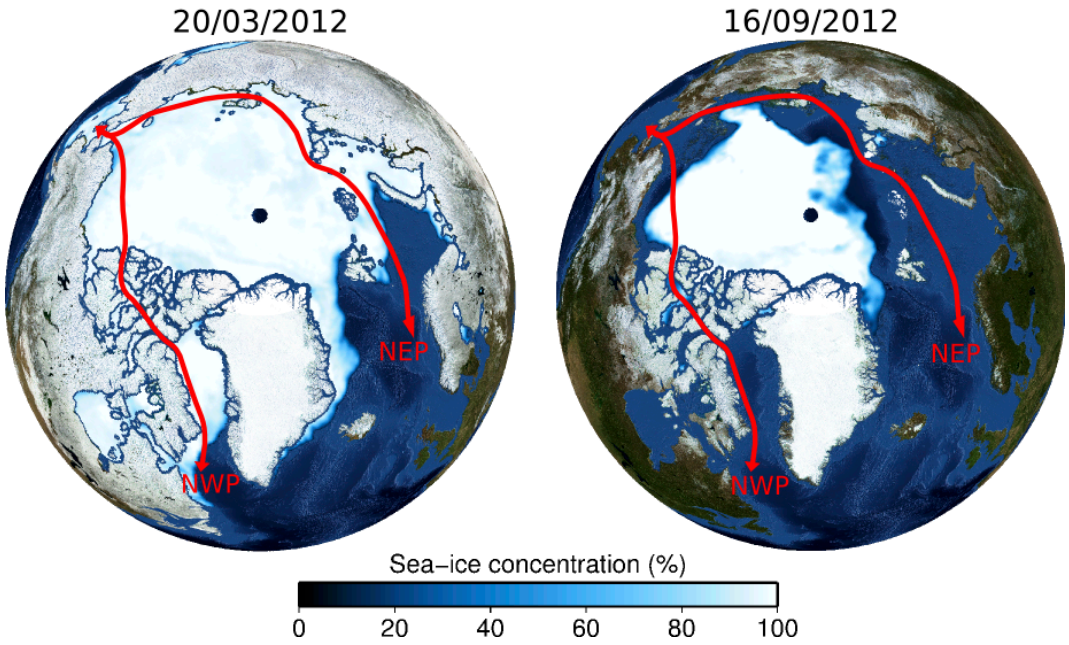

Figure 1.1. Arctic sea-ice cover during the annual ice extent maximum at the end of the winter season in mid-March 2013 and the record minimum at the end of the melting season in mid-September. Red lines represent the prominent shipping routes through the North-West Passage (NWP) and the North-East Passage (NEP). Ice-concentration data are from Ocean and Sea Ice Satellite Application Facility (OSI SAF), (Eastwood, 2012).

The ongoing shrinking of the ice cover (Serreze et al., 2007) might therefore allow for a transpolar shipping route in the future.

One of the most important properties of sea ice is its thickness distribution since many of the above considered processes are thickness-depend. For example, the thinner the ice the more heat is conducted from the ocean to the atmosphere and vice versa. Moreover, recent studies have also shown that due to the change to more seasonal and thus thinner ice, light transmittance and absorption increased (Nicolaus et al., 2012). Sea-ice thickness also becomes more and more important for economical reasons. Information and forecasts about sea-ice conditions and particularly thickness are essential for shipping and prospecting.

There is notable evidence for the thinning of the Arctic sea ice and thus a loss of sea-ice volume during the last decades (Rothrock et al., 1999; Giles et al., 2008; Kwok et al., 2009; Lindsay and Schweiger, 2015). Hence, it is crucial for the future that we continuously monitor sea-ice thickness and improve our thickness retrievals. But observing sea-ice thickness is more challenging than sensing the sea-ice area. Measuring sea-ice thickness through field investigations is limited by their little spatial and temporal coverage (Haas, 2009). Several satellite missions (e.g. ICESat, ERS and Envisat) have demonstrated that remote sensing offers a great potential in monitoring sea-ice thickness but also showed

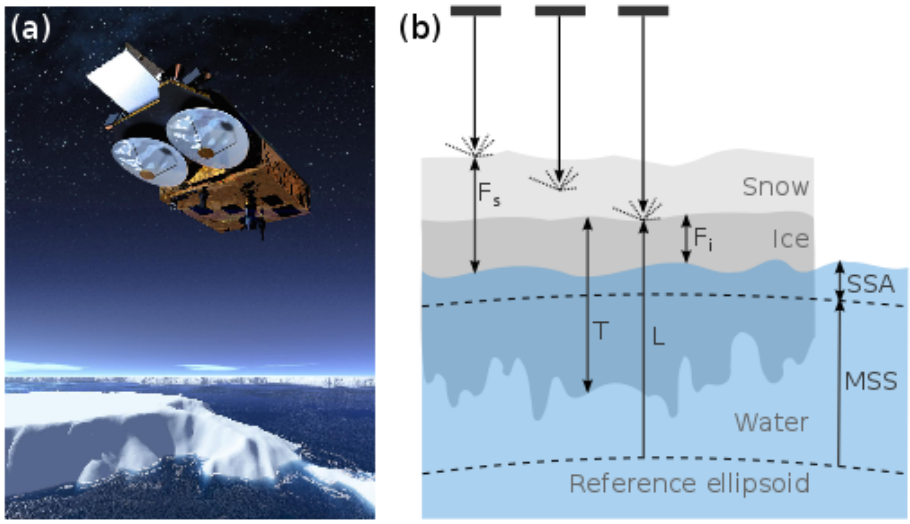

Figure 1.2. (a) CryoSat-2 artwork which shows the transmitter and receiver antenna of the Synthetic Aperture Interferometric Radar Altimeter (SIRAL). Credit: Astrium (EADS Astrium GmbH). (b) Illustration of measurement parameters in satellite altimetry: sea-ice freeboard (F_i), snow freeboard (F_s), Sea-ice thickness (T), mean sea-surface height (MSS), sea-surface anomaly (SSA), and ellipsoidal surface elevation (L).

considerable uncertainties (Haas, 2009), because in contrast to the lateral extent, thickness cannot be observed directly. CryoSat-2, launched in 2010, is a current satellite mission by the European Space Agency (ESA) that carries a radar altimeter that was developed mostly for applications over ice (Figure 1.2a) and is a step forward to fill the gap of information about the thickness of the polar marine sea-ice fields.

1.2 Satellite altimetry over sea ice

Satellite altimeters are able to yield sea-ice thickness on basin scale over a long time span of several years. However, they do not have the capability to measure the thickness directly. They use electromagnetic pulses to measure the time delay of the reflected echo and hence receive the distance between surface and satellite. Figure 1.2b illustrates the measurement parameters in satellite altimetry. With exact positioning of the satellite it is possible to obtain ellipsoidal surface elevations L along the satellite ground track. The first step to retrieve sea-ice thickness is to determine the sea-ice freeboard F_I which is the height of the sea-ice surface above the sea level. Therefore an accurate sea-surface height retrieval at the time of the satellite overflight is crucial. The actual sea-surface height can be formulated as the sum of a mean sea-surface height (MSS) and a sea-surface anomaly (SSA) which represents the actual state of the sea level. This includes tides as well as local anomalies (e.g. eddies). The actual sea-surface height can be retrieved

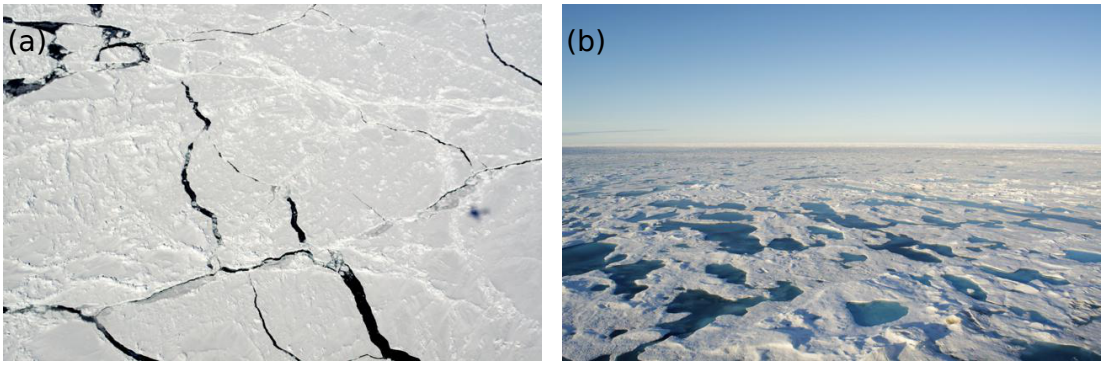

Figure 1.3. (a) Leads are cracks in the sea-ice cover and are crucial for retrieving sea-ice freeboard and thickness from satellite altimetry range measurements. The picture is taken from the Polar-6 aircraft during the Airborne Measurements for Antarctic sea ice monitoring (AMASIM) 2013 over sea ice in the Weddell Sea (b) Meltponds prevent the application of radar altimetry over sea ice during summer melt. The picture is taken from the research icebreaker 'Polarstern' during the ARKXXVI/3 expedition in 2011in the central Arctic.

by a detection of the elevation of the water surface in leads, which are openings in the ice that form due to diverging or shearing of ice floes (Figure 1.3a). Their elevations can be used as tie points to interpolate the sea-surface height along the satellite track. Depending on the utilised wavelength of the electromagnetic pulses and the properties of the snow, the sensed horizon can be the snow surface, the ice surface or a layer in between (Figure 1.2b). In literature the snow freeboard F_{S} is generally associated with laser altimetry. Laser altimeters like on-board the Ice, Cloud and Land Elevation Satellite (ICESat) work with infrared or near-infrared radiation (e.g. ICESAt: 1064 and 532 nm wavelength) and feature a low beam divergence resulting in a narrow, point-like footprint. The laser beam is always reflected at the snow surface. In contrast, radar altimeters use wavelengths in the range of centimetres and exhibit a higher beam divergence and therefore a larger footprint. The ice freeboard is usually associated with radar altimetry due to its capability of penetrating the snow cover, since it utilises centimetre wavelengths. Thus the freeboard can be obtained through:

$$F_{\mathrm{I,S}} = L - (MSS + SSA). \tag{1.1}$$

By assuming hydrostatic equilibrium, the ice/snow freeboard $F_{\mathrm{I,S}}$ can now be converted into sea-ice thickness T as a function of assumptions for water density ρ_{w}, bulk snow density ρ_{s}, bulk sea-ice density ρ_{i} and snow depth S (Laxon et al., 2003; Giles et al., 2008; Kwok et al., 2009; Wadhams et al., 1992):

$$
\begin{aligned}
T =& \frac{\rho_w}{\rho_w - \rho_i} F_{\mathrm{I}} + \frac{\rho_s}{\rho_w - \rho_i} S \\
=& \frac{\rho_w}{\rho_w - \rho_i} F_{\mathrm{S}} + \frac{\rho_w - \rho_s}{\rho_w - \rho_i} S
\end{aligned} \tag{1.2}
$$

Snow depth can feature high variabilities, depending on precipitation, drift and sea-ice freeze up. Typical values for snow depth on Arctic multiyear ice are in the range of 0.35 m for April/May, when it reaches a maximum (Warren et al., 1999). On Antarctic sea ice snow depth can reach higher values due to higher precipitation rates, but little is known about large scale distributions. In contrast to snow depth, the dependency of bulk snow density on the ice age is low and is in the range of 320 kg/m^3 (Alexandrov et al., 2010). Bulk ice densities ρ_{i} depend on the ice age and are typically in the range of 917 kg/m^3 for first-year ice and 882 kg/m^3 for multiyear ice in the Arctic. Ice densities can vary strongly and depend on the salinity and particularly on the fractional volume of air bubbles (Schwerdtfeger, 1963; Cox and Weeks, 1982; Alexandrov et al., 2010). Ice and snow density as well as snow depth affect the buoyancy of the sea ice and hence the freeboard. Since ice freeboard is approximately multiplied tenfold to obtain sea-ice thickness, small uncertainties in densities of snow and ice as well as snow depth can cause large thickness uncertainties (Giles et al., 2007; Alexandrov et al., 2010).

1.2.1 Radar altimetry

Satellite radar altimeters are widely used to measure ocean and ice sheet elevations which has also been their primary application. Altimetric measurements from Seasat (Ulander, 1987) and Geosat (Hawkins and Lybanon, 1989) have been the first that were collected over sea ice. Satellite radar altimeters emit microwaves in short pulses towards the surface. The time delay of the reflected signal is measured and can be converted into range measurements by knowing the exact position of the satellite.

During Arctic summer, when snow melts completely, ponds of melt water form on sea ice (Figure 1.3b). They usually start to form in June and refreeze in September. The water level of melt ponds does not coincide with the actual sea-surface height as long as they are not connected by drain channels to the ocean. Since the backscatter of smooth open water dominates the echoes from ice and because signals from melt ponds cannot be separated from leads, satellite altimeter measurements cannot be used during summer season.

The European Remote Sensing (ERS) missions (Laxon et al., 2003) were the first satellites that have been used to retrieve sea-ice thickness in the Arctic, continued by the

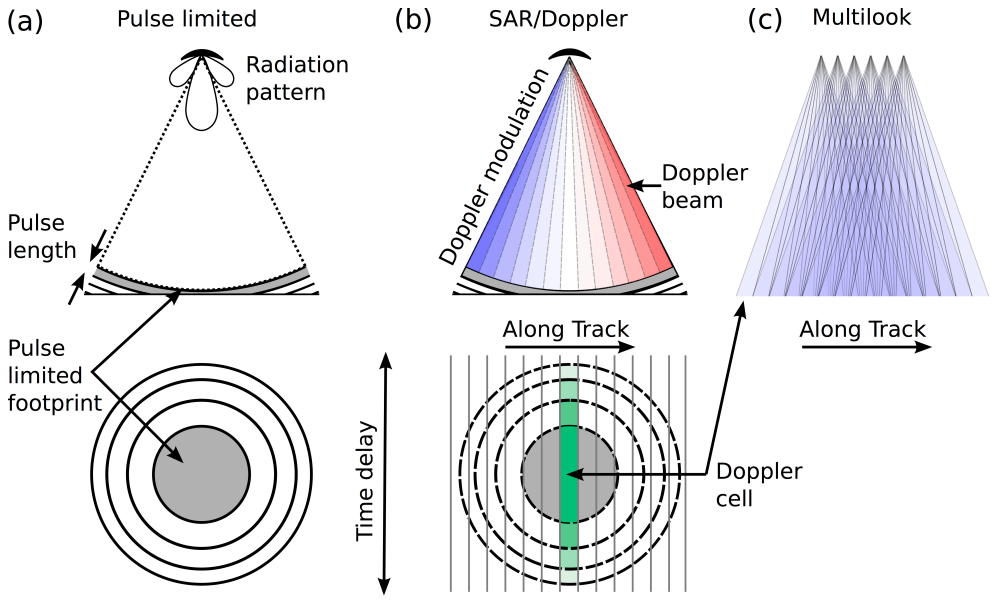

Figure 1.4. Comparison between a conventional radar altimeter (a) and a Delay Doppler/SAR radar altimeter (b). The spatial resolution is increased due to the separation into Doppler beams, that feature a phase shift according to the motion of the satellite. (c) Stacking of multi-looks from different Satellite positions to one target (Doppler cell) reduces noise. Figure similar in Raney (1998).

Environmental Satellite (Envisat) in 2002. They featured a footprint of 2 – 10 km and an orbit coverage limited to 81.5°N. In contrast, the laser altimeter on-board of ICESat had an improved resolution of 70 m and a latitudinal coverage of up to 86°N (Connor et al., 2009). But whereas radar altimetry is not constrained by atmospheric conditions, laser pulses are prevented by clouds so that the coverage of measurements is limited.

ERS and Envisat carried conventional *pulse-limited* radar altimeters. The range resolution δ_r for pulse-limited radar altimeters directly depends on the pulse length τ (Figure 1.4a):

$$\delta_r = \frac{c_0 \tau}{2} \tag{1.3}$$

where c_0 is the speed of light in vacuum. Within the illuminated area the range estimate corresponds to the distance between the antenna and the scattering horizon. After the first arrival of the wave front it takes the pulse length until the inner part of the footprint area is illuminated. According to Eq. 1.3 a short pulse length enhances the range resolution but usually corresponds with a low signal strength and vice versa. On the other hand a high signal strength is essential to discriminate the signal from noise. To achieve both a short pulse length and a sufficient signal strength, the so-called pulse compression is applied.

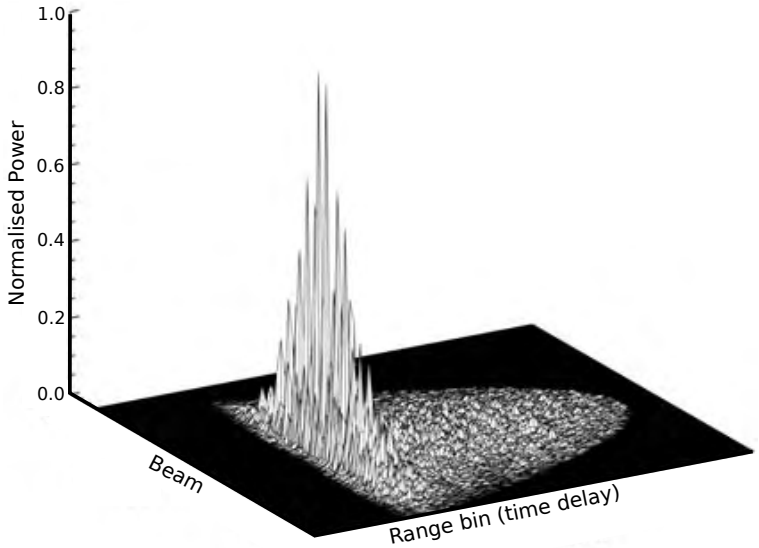

Figure 1.5. Simulated CryoSat-2 beam stack over ocean. Each Doppler beam belongs to a corresponding burst. Credit: ESA (2007).

By using this technique, the transmitted pulse has a sufficient strength and is modulated with a time-dependent frequency (chirping). The received signal is then cross-correlated with the transmitted signal (matched filter), which results in echoes that are shorter in time and therefore allow an accurate determination of the time delay. This finally leads to an increase in the range resolution and signal to noise ratio.

The area, that is illuminated by a pulse-limited radar is typically in the range of kilometres (e.g. 2 – 10 km for ERS1/2 and Envisat). An improvement of the lateral resolution can be achieved by a Synthetic Aperture Radar (SAR) Altimeter like on-board of CryoSat-2.

1.2.2 CryoSat-2 - delay Doppler/SAR altimetry

In order to improve the lateral resolution, an extension of the aperture is necessary. However, a larger aperture is construction-limited. But a long aperture can be simulated by transmitting coherent pulses along track. Therefore bursts of pulses within an interval of 50 μs are transmitted towards the surface. Due to the along-track motion of the satellite, the returning signal experiences a Doppler shift, depending on the viewing direction (Figure 1.4b). Thus, the footprint can be divided into subsections according to the phase shift of the radar return. These series of subsections are called doppler beams (Figure 1.4b). Hence, there is an assembly of Doppler beams from different bursts that steer to the same fixed point on the surface (multi-look) (Figure 1.4c). This assembly

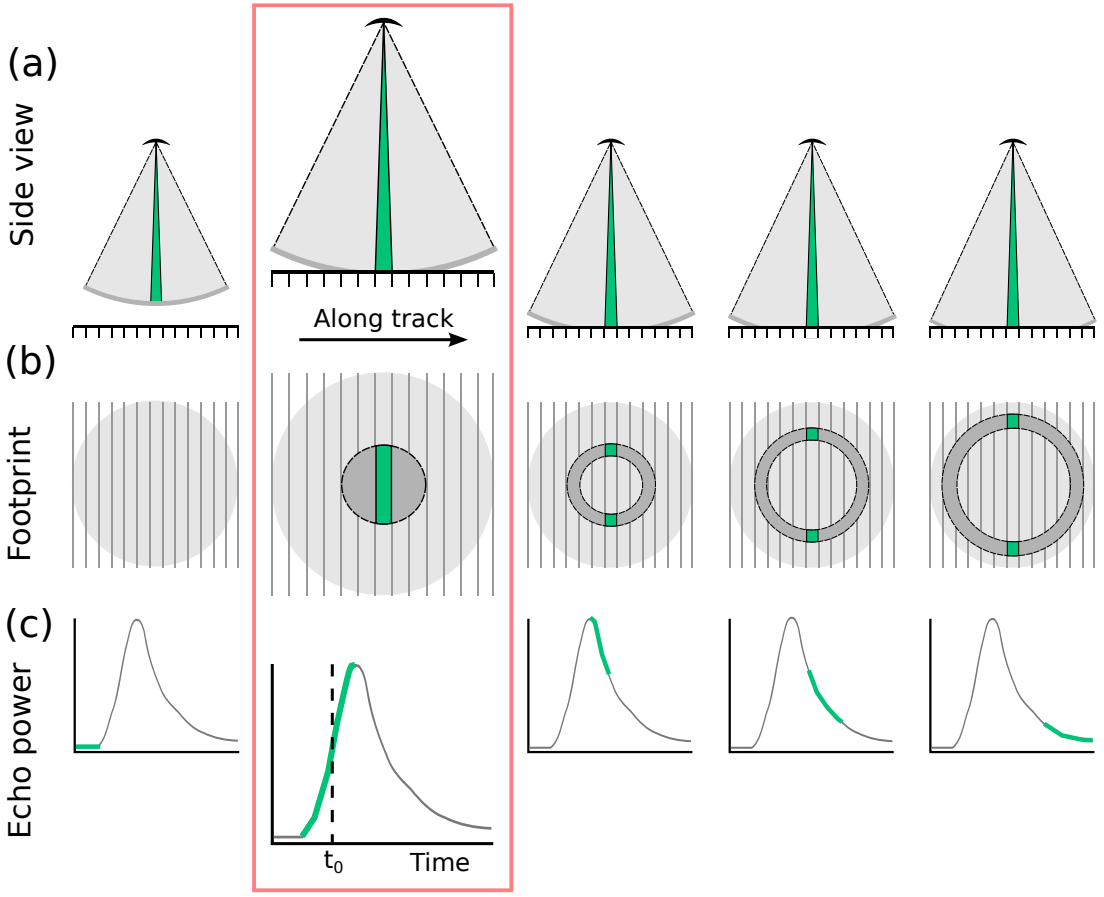

Figure 1.6. Theoretical building of a Delay Doppler/SAR waveform. (a) Side view of the antenna radiation pattern. The green section represents a single Doppler beam. (b) Step-by-step illuminated area (footprint). Due to the Delay Doppler/SAR processing the footprint is only a small part of the ring that is build by conventional radar altimetry. (c) Step-by-step builded waveform, showing the point t_0, where the main scattering horizon is tracked. The red box highlights the development of the leading edge.

of Doppler beams is called *beam stack*. Figure 1.5 shows a simulated beam stack over ocean.

In consequence of the Doppler shift, the received signals are incoherent. By a phase correction the according beams can be stacked, leading to an improved signal-to-noise ratio. This technique is called delay Doppler altimetry (Raney, 1998).

Figure 1.6 shows the theoretical development of the radar return for a delay Doppler/SAR altimeter. When the inner part of the footprint is illuminated, the echo power reaches a maximum (Figure 1.6c). The arrival of the outer part of the wave front then causes off-nadir reflections that are represented in the declining part of the echo power distribution, which can also contain contributions from volume scattering. This temporal distribution of the echo power is called *waveform*. Figure 1.6c only shows a simplified shape of a

waveform over sea ice. In reality they can feature much higher complexity due to noise and surface properties, which can cause multiple peaks for example.

In order to determine the surface elevations, a *retracking algorithm* is applied to waveforms. Various retracking algorithms exist and their field of application depends on the surface type. They fit functions to the received echoes to finally track the main scattering horizon at the leading edge. Then, power thresholds can be used to determine the tracking point at the leading edge (Figure 1.6c)

After the failed first CryoSat mission launched in 2005, CryoSat-2 was launched in 2010 (Figure 1.2a). CryoSat-2 is part of the ESA's Living Planet Program and was dedicated for the observation of changes in the cryosphere. This includes especially the determination of variations in sea-ice thickness in the Arctic Ocean. Wingham et al. (2006) provide an overview of the CryoSat-2 Mission. The satellite is equipped with the K_{u}-band radar altimeter SIRAL (Synthetic Aperture Interferometric Radar Altimeter) (Rey et al., 2001). CryoSat-2 orbits cover the Arctic up to 88°N which is an improvement compared to former missions (e.g. ICESat, ERS and Envisat) that left a broad data gap in the Arctic sea ice. Table 1.1 shows the instrument characteristics of Cryosat-2, that can be operated in three different modes: the pulse-limited Low Resolution Mode (LRM), the Synthetic Aperture Radar mode (SAR) and the interferometric SARIn mode. The LRM mode is used over open oceans and the inner parts of the Greenland and Antarctic ice sheets. Over sea-ice-covered areas CryoSat-2 operates mostly in SAR mode as it provides high resolution measurements. However, within a window north of Canada between 80°– 85°N and 100°– 140°W CryoSat-2 is operated in SARIn mode to study its performance over sea ice. Data obtained in SARIn mode additionally contain phase information of the radar return, that allow for the localisation of radar backscatter within the footprint. This mode is especially suitable for regions with a steep slope (e.g. shelf ice edges and glaciers), but also to study the influence from off-nadir reflections over sea ice (Armitage and Davidson, 2014). By using delay Doppler/SAR altimetry CryoSat-2 reaches resolutions of approximately 300 m along track and 1650 m across track, which is a remarkable improvement compared to former satellite radar altimeter missions (e.g. ERS1/2, Envisat, see Section 1.2.1).

1.2.3 Snow covered sea ice and its impact on radar altimetry

The snow cover is a fundamental component of the polar atmosphere-ice-ocean interaction system that features a high variation on temporal and spatial scale (Eicken, 2008; Sturm et al., 2002; Iacozza and Barber, 1999). It can feature a complex stratigraphy as a result of different conditions. During winter, subsequent depth hoar formation after snowfall occurs due to temperature-gradient metamorphism (Colbeck, 1982; Nicolaus et al., 2009). As a

Table 1.1. Synthetic Aperture Interferometric Radar Altimeter (SIRAL) instrument characteristics, modified from Wingham et al. (2006) and Bouzinac (2012).

	Measurement mode		
	LRM	SAR	SARIn
Carrier frequency (GHz)	13.575		
Antenna Gain (dB)	42		
Along-track antenna 3 dB width	1.0766°		
Across-track antenna 3 dB width	1.2016°		
Transmitted (measured) bandwidth (MHz)	350 (320)		
Transmitted power (W)	25		
Transmitted (measured) pulse duration (μs)	49 (44.8)		
Pulse repetition interval	1971 Hz	18.182 kHz	18.182 kHz
Burst repetition interval (ms)	-	11.7	46.7
Samples per echo	128	128	512
Measurement range window (m)	60	60	240
Measurement range gate (m)	0.46875		
Interferometer Baseline (m)	-	-	1.172
Tracking samples per echo	128		
Tracking range window (m)	60	60	480
Tracking range gate (m)	0.469	0.469	3.75
Data rate	51 kbps	12 Mbps	24 Mbps
Power consumption (W)	95	130	125
Mass (kg)	61		
Altitude (km)	717		
Repeat cycles	369 days with 30 day sub-cycle		

consequence, low-density horizons of faceted crystals with diameters of up to 1 cm can form, whereas a fresh snow layer consists of small grains of millimetre to sub-millimetre dimension. Melting events, the downward transport of moisture and subsequent freezing can cause the forming of ice layers and ice lenses. Moreover, changing radiation and wind compaction also contribute to this high variability and inhomogeneity.

The accuracy of sea-ice thickness retrievals derived from radar altimetry depends on the freeboard retrieval. A snow cover establishes an additional uncertainty contributing to the remote sensing signature of sea ice (Sturm and Massom, 2009). Snow and ice lenses within the snow feature physical properties that affect the scattering of the radar signal (Hallikainen and Winebrenner, 1992), particularly at K_u-band frequency as used by CryoSat-2. In current literature it is widely assumed that the peak power of the returning CryoSat-2 radar echo is expected to originate at the snow-ice interface. This

assumption is based on laboratory experiments by Beaven et al. (1995). They showed that a 13.4 GHz radar echo originates at the snow-ice interface under dry and cold conditions with a uniform snow stratigraphy. Even by considering the increased Arctic melt season length, snow is not melting during the winter (Markus et al., 2009), but metamorphic processes and densification can occur. Data from airborne K_u-band radar altimeters and in-situ field measurements from the CryoVEx 2006 and 2008 campaigns were analyzed by Willatt et al. (2011). They reveal that in Spring 2006, at temperatures around the freezing point, the dominant scattering surface in 25 % of the radar returns is located close to the snow-ice interface whereas in 2008, when the temperatures were lower, this percentage rises up to 80 %. As a consequence an accurate estimation of sea-ice freeboard is only possible under dry and cold snow conditions with a known snow load (Makynen and Hallikainen, 2009) and without a distinct metamorphic history.

In order to isolate effects from scattering within the snow layer, it is useful to compare coincident measurements from laser and radar altimetry (Cullen et al., 2006). Whereas the laser ranges to the snow surface, the radar should measure the distance to the snow-ice interface (Kwok et al., 2004) if internal scattering in the snow is neglected. Hence, the difference in elevation between both sensor retrievals potentially indicates the snow depth, if the lower propagation speed of the radar pulse within the snow layer is considered. Those investigations have been accomplished by Giles et al. (2007) with airborne laser and radar altimeter measurements over the Fram Strait. Connor et al. (2009) compared Envisat radar and airborne laser altimeter measurements over Arctic sea ice and found differences in elevation which they associated with the snow layer to some extent. On the other hand, such comparisons between laser and radar may also serve to evaluate the radar retrieval if information about snow depth exist (Ricker et al., 2013, 2014a).

The snow stratigraphy on Antarctic sea ice features another component that contributes to its complexity. Due to the combination of relatively thin ice compared to the Arctic and high precipitation rates on the other hand, sea ice can be depressed beneath the sea level. Flooding of the ice surface can then occur by lateral incursion and/or by percolation vertically through the ice lattice. The resulting layer of slush is a mixture of ice crystals and water. It subsequently refreezes and builds a layer of snow-ice. Flooded snow layers can reach a height of 0.1- 0.2 m (Massom et al., 2001). The dielectric constant of snow with water inclusion is about 40 times higher than of dry snow (Hallikainen et al., 1986) and hence a radar echo will be reflected by wet snow. Willatt et al. (2010) carried out the first field measurements to evaluate K_u-band scattering effects within the snow layer on Antarctic sea ice during September and October 2007. They conclude that only snow without morphological features or flooding results in a snow-ice interface as the dominant scattering surface. Moreover, 43 % of the returns originated at the air/snow interface, 30 % from the snow/ice interface and 23 % from an internal layer. This results in a mean

depth of the dominant scattering surface that is about 50 % of the mean snow depth (Willatt et al., 2010).

Simulating the interaction of radar waves with snow is a valuable method to get information about the scattering mechanisms at the interfaces within the snow layer. It can also contribute to our understanding of how the scattering horizons depend on the snow properties. Recent Studies about the simulation of K_u-band altimeter echoes from sea ice have been presented in Tonboe et al. (2006); Makynen and Hallikainen (2009). Tonboe et al. (2006) use a radiative transfer model to simulate the sea ice effective scattering surface variability as a function of snow depth and density. They reveal that a snow cover might have a variable but significant impact on the estimation of the sea-ice thickness with radar altimetry. This model does not consider surface roughness and does not account for antenna gain function or pulse shape (Makynen and Hallikainen, 2009). In general this model is similar to Ridley and Partington (1988). Makynen and Hallikainen (2009) have built a simulator for ASIRAS (airborne radar altimeter, see Section 1.2.4) echoes over snow covered first year ice which is also valid for Cryosat-2 echoes. In contrast to Tonboe et al. (2006) they take antenna gain and pulse shape into account. The results show that for dry snow the leading edge originates at the sea-ice surface and the volume echo is negligible. Under moist snow conditions the snow-surface echo dominates. The power level of the echo decreases highly due to the attenuation of snow (Makynen and Hallikainen, 2009). Kwok (2014) analysed airborne snow and K_u-band radar data (Operation Ice Bridge, see Section 1.2.4) and concluded that scattering at the snow surface and within the snow layer is non-negligible.

1.2.4 Validation activities

One primary goal of the CryoSat-2 mission is to resolve trends in sea-ice thickness with an accuracy of 3 cm/year. Therefore it is crucial to calibrate and verify the satellite measurements and processing algorithms. The validation of the freeboard is the first important step in evaluating the CryoSat-2 product since it directly refers to the range measurements whereas the thickness retrieval is also affected by the uncertainties of ice, water and snow densities which are needed for the conversion.

The most accurate freeboard and thickness measurements can be obtained by in-situ drilling (Figure 1.7a). This method is valuable on small regional scales, providing measurements of ice freeboard and thickness as well as snow depth along validation lines. Nevertheless such measurements are time consuming with a substantial logistical effort and restricted spatially and temporally coverage.

Autonomous observations can be made with ice mass balance buoys (IMB's) that monitor seasonal ice growth and melt as well as the accumulation of snow (Figure 1.7b). These

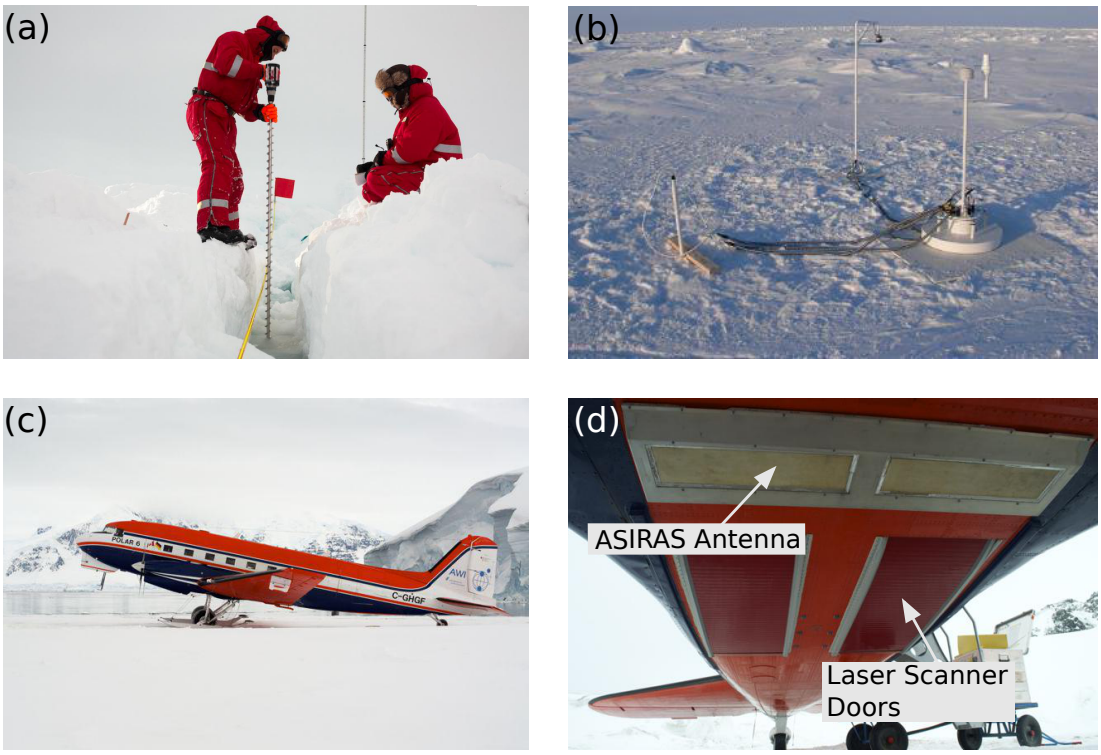

Figure 1.7. CryoSat-2 validation measurements of different temporal and spatial scale. (a) Drilling activities provide only point measurements in a restricted area, but are of high accuracy. (b) Ice mass balance buoys are attached to an ice floe but provide year-round measurements of freeboard, thickness and snow depth. Credit: `http://www.erdc.usace.army.mil/Media/FactSheets/FactSheetArticleView/tabid/9254/Article/553850/ice-mass-balance-imb-buoy-program.aspx` (c) AWI Polar-6 airplane ready for takeoff to go on a validation flight, equipped with a laser scanner and an Airborne SAR/Interferometric Radar Altimeter System (ASIRAS). (d) Airborne validation surveys can be conducted in coincidence with satellite overflights and therefore offer the capability of direct comparisons.

systems are deployed on an ice floe with acoustic sensors above the ice surface and at the bottom of the ice. Changes in snow and ice thickness can be obtained hourly, via a satellite transmitter unit in near-real time. The major advantage of IMB's is the year-round availability of data, although these measurements always refer to the same ice floe.

In contrast, observations from aircraft allow a better spatial coverage along flight tracks of several hundreds of kilometres but can be only carried out in spring/summer and depend on weather conditions. The CryoSat Validation Experiment (CryoVEx) of the European Space Agency is a program that combines field as well as airborne laser (Lidar) and radar altimetry measurements in the Arctic and Antarctic in order to validate CryoSat-2 measurements and retrieval algorithms (Figure 1.7c and d). The conducted airborne laser

measurements provide high-precision range determination and thus are capable to evaluate freeboard measurements of the SIRAL radar altimeter on-board CryoSat-2 on spatial scales comparable to satellite acquisitions. The accuracy for the range measurements is within a few centimetres. The main limitation is due to GPS positioning, especially for a longer baseline of more than 100 km. Then the accuracy is only within 10-30 cm (Forsberg et al., 2002). Laser scanners, used during several validation campaigns, have an angle of beam of 45°-60° and cover typically 400 m broad scan lines at 500 m altitude with a point spacing of 4 m while the scan line spacing along track is less than 1 m.

The Airborne SAR/Interferometric Radar Altimeter System (ASIRAS) was built as a simulator for SIRAL (Cullen et al., 2006; Helm, 2008). It is mounted at the bottom of an aircraft (see Figure 1.7c and d). Since 2004 several validation campaigns took place with ASIRAS, always in combination with the airborne Lidar. ASIRAS can work in two different modes: the Low Altitude Mode (LAM) is usually used to survey the sea ice on an operational altitude between 200 and 1100 m. Only one antenna acts as a receiver, just as the SAR mode of CryoSat-2. Whereas the HAM (High Altitude Mode) mode has an operational altitude between 1100 and 7000 m. Moreover, electromagnetic induction thickness sounding (Pfaffling et al., 2007; Hendricks, 2009; Haas et al., 2010) has been operated during CryoVEx and is an efficient method to measure sea-ice thickness directly from helicopter or aircraft.

The first CryoVEx campaign was launched in 2003 and started with some pre-launch studies of CryoSat-2 over the Arctic Ocean and the sea-ice covered Baltic Sea. Further measurements took place over Greenland, Spitsbergen and Lincoln Sea and are on-going.

In order to bridge the gap between ICESat and the launch of ICESat-2, that is scheduled for 2016, the National Aeronautics and Space Administration (NASA) initialised the Operation Ice Bridge (OIB) mission in 2009. Among various other sensors, OIB aircraft carry a laser altimeter and a snow-radar. They are operated on a yearly basis in spring over Arctic sea ice, particularly multiyear ice, and provide measurements that are also valuable for the validation of CryoSat-2, especially to get additional information about snow depth (Kurtz et al., 2013).

1.3 Scope of this work

First CryoSat-2 thickness and volume estimates have been published in Laxon et al. (2013) and Kurtz et al. (2014). Both studies were based on different interpretations of the waveform. Comparisons between the estimates showed that there are considerable

discrepancies (Kurtz et al., 2014; Ricker et al., 2014a). The main goal of this study is to evaluate uncertainties from various sources and analyse their impact on the freeboard and thickness retrievals. In particular, determining the main scattering horizon to receive geolocated surface elevations depends on the assumption of a power threshold at the leading edge (see Section 1.2). The variation of these thresholds enables to quantify the bias which may arise due to these assumptions.

Another source of uncertainty is the scattering of the K_{u}-band waves in the snow layer. The hypothesis that the main scattering horizon is always located at the snow-ice interface for the period between October and April follows the findings from Beaven et al. (1995) (see Section 1.2.3). On the other hand, studies that analysed in-situ measurements (Willatt et al., 2010, 2011; Kwok, 2014) suggested that this assumption might not be valid in either case. Moreover, due to the footprint size, surface roughness contributes to the uncertainty that cumulates at the leading edge of a CryoSat-2 waveform. Testing this hypothesis using validation data will be another part of this thesis.

Armitage and Davidson (2014) have shown that off-nadir reflections from leads can bias the range retrievals since it is assumed that the main reflector is in the nadir of the satellite. Off-nadir reflectors typically occur when specular reflection on the edge of the main radar lobe still dominate the return signal. These biased waveforms are mostly a composition of reflections of leads and sea ice. They can potentially affect elevations of leads if classified as leads as well as ice elevations if classified as sea ice and cause a considerable range bias. Together with signal noise and the sea-surface height uncertainty it contributes to the total freeboard uncertainty, which is quantified in this thesis. With the conversion from freeboard into thickness additional uncertainties contribute to the error budget. Since little is known about covariances of the different parameters we separate between random and systematic uncertainties and try to quantify all uncertainty contributions.

As a first step, a processing chain has to be established to retrieve sea-ice freeboard, thickness and volume estimates, initiated with geolocated CryoSat-2 waveforms that are provided by the European Space Agency. Here, findings of Helm et al. (2014), who established a processing chain for land ice are used. Finally, sea-ice freeboard and thickness maps with corresponding uncertainty estimates shall be presented.

Validation measurements are essential to evaluate and improve satellite altimetric measurements. Nevertheless, there are various applied validation methods that differ on a spatial and temporal scale as well as in resolution and accuracy (see Section 1.2.4). Eventually the combined consideration of all these methods is a valuable approach to evaluate CryoSat-2 measurements and is presented in this thesis.

Whereas the main part of this study focusses on the Arctic sea ice, the next step is then to transfer these findings to the Antarctic sea-ice cover. Snow on Antarctic sea ice can feature a complex snow stratigraphy due to snow-ice and ice lenses (see Section 1.2.3). In addition little is known about the snow depth distribution on basin scale. Coincident snow depth and ice thickness in-situ measurements at Mc Murdo Sound are used for an initial evaluation of CryoSat-2 measurements in the Antarctic. Findings can then be used to accommodate the processing algorithm to calculate sea-ice thickness and volume estimates for Antarctic sea ice in the future.

1.4 Overview of papers

After retrieving the geolocated ellipsoidal elevations from the range measurements (see Section 1.3), they must be separated according to the respective surface type where the radar return originates. This step is necessary to establish the actual sea-surface height which is needed to derive the sea-ice freeboard. As already shown in Section 1.3 the CryoSat-2 footprint is of significant dimension according to sea-ice surface properties, although the application of Doppler modulation enhances the spatial resolution compared to former, pulse-limited, radar altimeter missions (e.g. ERS1/2, Envisat). Hence, waveforms can be ambiguous if the illuminated area contains not only a closed ice surface but also leads. Furthermore it is generally assumed that the peak power of a waveform originates in the nadir position (see Figure 1.6). This assumption proves to be false however if a lead is located off-nadir within the illuminated area, since it will still dominate the power distribution because of its smooth surface and hence bias the elevation retrieval. In the *first paper*:

Ricker, R., Hendricks, S., Helm, V. and Gerdes, R. (2015): **Classification of CryoSat-2 radar echoes** / G. Lohmann, H. Meggers, V. Unnithan, D. Wolf-Gladrow, J. Notholt and A. Bracher (editors), In: Towards an Interdisciplinary Approach in Earth System Science, (Springer Earth System Sciences), Heidelberg [u.a.], Springer International Publishing, 251 p., ISBN: 978-3-319-13864-0. doi: 10.1007/978-3-319-13865-7_17.

we investigate and present a method for surface classification from CryoSat-2 waveforms and in particular according to biased surface elevations due to off-nadir leads. This paper has been written nearly at the same time as the following one and therefore cross references exist between the two. Once the CryoSat-2 waveforms are classified and leads are detected, the actual sea-surface height can be interpolated along each CryoSat-2 track. With referencing the ice elevations to the sea level, we retrieve the sea-ice freeboard and the sea-ice thickness after the conversion, described in Section 1.3. All these steps introduce

uncertainties that have to be evaluated. Especially the tracking of the main scattering horizon at the leading edge of the waveform is based on first-order approximations and can have a substantial effect on the freeboard and thickness retrieval. Therefore in the *second paper*:

Ricker, R., Hendricks, S., Helm, V., Skourup, H. and Davidson, M. (2014): **Sensitivity of CryoSat-2 Arctic sea-ice freeboard and thickness on radar-waveform interpretation**, The Cryosphere, 8 (4), pp. 1607-1622. doi: 10.5194/tc-8-1607-2014.

we evaluate the uncertainties of sea-ice freeboard and higher-level products that arise from the choice of the retracking threshold. Furthermore random and systematic uncertainties due to the sea-surface height interpolation and snow and ice properties are quantified. Here we also present Arctic wide sea-ice freeboard and thickness maps of monthly averages from CryoSat-2 altimetric measurements. In particular, we find a rise of 0.02 - 0.15 m of freeboard from March 2013 to November 2013 in the multiyear ice region north of Greenland and Canada. The fact that thermodynamic growth of sea ice is unlikely during the melt season between June and September gives rise to the assumption that the CryoSat-2 freeboard retrieval may be biased by the snow cover in November 2013. In order to evaluate this apparent rise of sea-ice freeboard, validation measurements for the end of the winter season in March and begin of the freeze up in September are necessary. Ice mass balance buoys are the only instruments that have the capability to provide year-round measurements in the area of interest. In the *third paper*:

Ricker, R., S. Hendricks, D. K. Perovich, V. Helm, and R. Gerdes (2015), **Impact of snow accumulation on CryoSat-2 range retrievals over Arctic sea ice: An observational approach with buoy data**. Geophys. Res. Lett., 42, 4447–4455. doi: 10.1002/2015GL064081.

we therefore compare time series of freeboard and snow depth from ice-mass balance buoys with coinciding CryoSat-2 freeboard measurements to assess the findings of the 2nd paper with field data.

The state of the Antarctic sea ice is different from the Arctic. There is barely sea ice that survives the Antarctic summer melt. Moreover the snow layer can be much thicker than in the Arctic. Hence the sea ice is usually thinner than in the Arctic and can be depressed below the sea level, causing flooding of the ice surface. In the *fourth paper*:

Price, D., Beckers, J., **Ricker, R.**, Kurtz, N., Rack, W., Haas, C., Hendricks, S., Helm, V., Leonard, G., and Langhorn, P.J. (2015). **Evaluation of CryoSat-2 derived sea-ice freeboard over fast ice in McMurdo Sound, Antarctica**. Journal of Glaciology, 61(226), 285–300. doi: 10.3189/2015JoG14J157.

it is investigated how different CryoSat-2 freeboard processing algorithms perform over Antarctic sea ice and, in particular, land fast ice in McMurdo Sound. Drilling measurements have been conducted through Antarctic summer in 2011 and 2013. One validation line even coincides with a CryoSat-2 ground track. This study provides valuable information for the development of an Antarctic CryoSat-2 freeboard and thickness retrieval by using CryoSat-2 data. My contribution according this co-authorship comprised CryoSat-2 freeboard and thickness processing along CryoSat-2 tracks within the area of interest and algorithm/processing adjustments to accommodate the local surface properties that are dominated by land-fast ice and coastal polynyas which require a modified surface-type classification. Moreover, I was involved in discussions about methods, results and the comparison between the different algorithm retrievals.

Chapter 2

Classification of CryoSat-2 radar echoes

Published in *Springer International Publishing*, 251 p., ISBN: 978-3-319-13864-0. doi: 10.1007/978-3-319-13865-7_17

R.Ricker[1], S. Hendricks[1], V. Helm[1], and R. Gerdes[1]

[1]Alfred Wegener Institute, Helmholtz Centre for Polar and Marine Research, Bremerhaven, Germany

Abstract

Sea-ice thickness at global scale is an important variable in the polar climate system. Only satellite altimeters such as onboard the CryoSat-2 mission allow us to obtain sea-ice thickness on hemispherical scale. Accurate CryoSat-2 altimeter range measurements provide surface elevations which have to be referenced to the local sea level to obtain sea-ice freeboard that can be converted into sea-ice thickness assuming hydrostatic equilibrium. The local sea-surface height is determined by careful detection of leads in the ice surface using the specific characteristics of the radar signal. Off-nadir reflections from leads can significantly affect the range retracking and hence bias the surface elevations of leads and sea ice. This can finally lead to a negative freeboard and hence also affects the thickness and volume retrieval. We present a method for the classification of CryoSat-2 radar echoes to correctly discriminate between valid and off-nadir biased echoes. We apply our classification to a CryoSat-2 track from December 15 where 50 leads over a distance of 2300 km are identified. Overall 22 % of the surface elevations are associated with biased radar echoes.

2.1 Introduction

Several studies have shown considerable evidence that the Arctic sea ice is thinning during the last decades (Rothrock et al., 1999; Kwok et al., 2009; Haas et al., 2010). When combined with the observed rapid reduction of the ice covered area (Comiso, 2002; Comiso et al., 2008; Stroeve et al., 2012) this leads to a decline in sea-ice volume (Laxon et al., 2013). The only remote sensing technique capable of quantifying this ice-volume decrease at global scale is satellite altimetry. This method is based on the retrieval of the sea-ice freeboard, which is the height of the ice-surface above the local sea level (Figure 2.1a). Assuming hydrostatic equilibrium the freeboard can be converted into sea-ice thickness (Wadhams et al., 1992; Giles et al., 2008; Kwok et al., 2009) and with additional information into sea-ice volume (Laxon et al., 2013).

Satellite altimeters are operated in different electromagnetic wavelength ranges. The laser altimeter onboard the ICESat mission featured a small footprint (70 m) but was affected by clouds. Radar altimeters on the other hand are not affected by clouds but have a larger footprint of several kilometres. CryoSat-2 is the current satellite altimeter mission of the European Space Agency (ESA) and was launched in April 2010, with special emphasis on Arctic sea ice. It is equipped with a Ku-Band SAR radar altimeter (SIRAL - Synthetic Aperture Interferometric Radar Altimeter) that uses along-track beam sharpening (Wingham et al., 2006) to reduce footprint size compared to previous radar altimeter missions (ERS1/2, Envisat). By using the effect of the *Doppler shift* the radar footprint can be divided into stripes called *Doppler cells* (for CryoSat-2 approximately 250 m). Each cell is illuminated from different incident angles as the satellite passes by (Figure 2.1a). The echoes of each illumination are stacked to reduce noise. This method results in a higher resolution than pulse-limited radar altimeters like onboard ERS1/2 and Envisat.

Since the uncertainties of freeboard can easily reach the magnitude of freeboard itself, optimized algorithms that reduce errors and uncertainties in CryoSat-2 freeboard retrieval are necessary. The first step in obtaining sea-ice freeboard is to determine the main scattering horizon to receive geolocated surface elevations (Kurtz et al., 2014; Ricker et al., 2014a). In this study a *threshold first-maximum retracker* with a 40% threshold (TFMRA40) (Ricker et al., 2014a; Helm et al., 2014) is applied to the geolocated radar echoes (waveforms) that are provided by the European Space Agency. Within this retracker algorithm the waveform is oversampled and smoothed. We compute the derivative to find the first maximum of the waveform and assign the main scattering horizon at 40% of this first peak. The effects of different thresholds and retrackers on the freeboard retrieval can be substantial and have been investigated in Ricker et al. (2014a) and Kurtz et al. (2014). In the second step the geolocated CryoSat-2 elevations have to be referenced to the sea

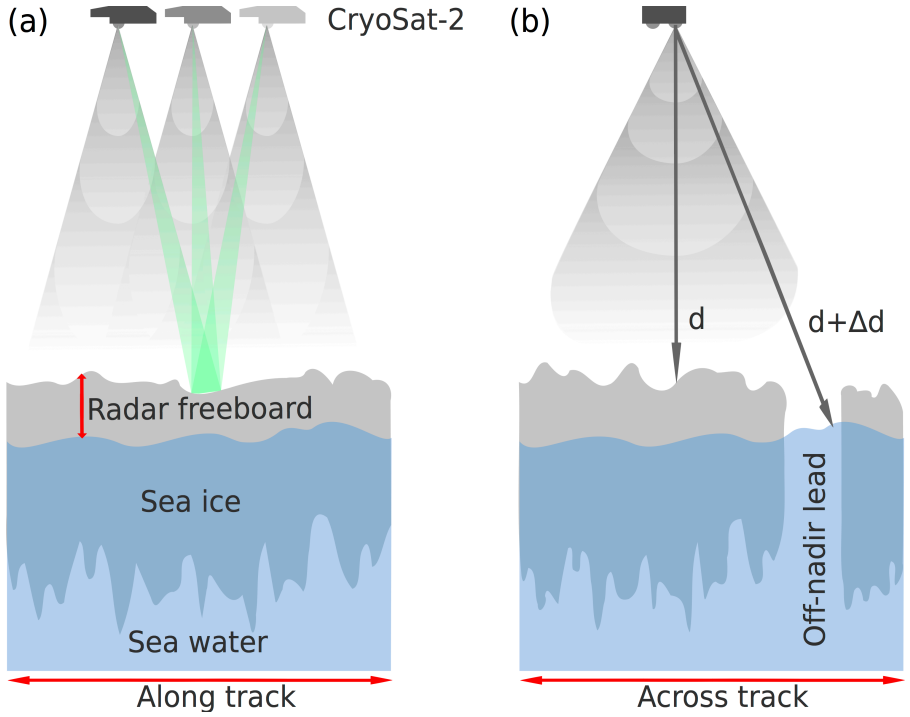

Figure 2.1. (a) Scheme of CryoSat-2 measurements along track. The green illuminated area illustrates a Doppler cell. (b) Scheme of CryoSat-2 measurement across track with an off-nadir lead at the edge of the main radar lobe, causing a range bias of Δd.

level to obtain the freeboard. We apply a waveform classification algorithm (Ricker et al., 2014a) in order to detect leads which are narrow open water areas in the ice surface. At leads the sea level can directly be obtained by the CryoSat-2 range measurement. The lead elevations are interpolated along the CryoSat-2 ground tracks to receive the actual sea-surface height which is then subtracted from the sea-ice elevations to get the sea-ice freeboard.

Armitage and Davidson (2014) have shown that off-nadir reflections from leads can bias the range retrieval since elevation retrievals are based on the assumption that the main reflector is in the nadir of the satellite. They typically occur when specular reflection on the edge of the main radar lobe still dominate the return signal (Figure 2.1b and 2.2). These biased waveforms are mostly a composition of reflections of leads and sea ice. They can potentially affect elevations of leads if classified as leads as well as ice elevations if classified as sea ice and cause a range bias of Δd (Figure 2.1b). In this study we present our method to discriminate waveforms that are biased by off-nadir reflections from leads and valid sea-surface height information. In addition the waveform classification scheme is extended to also discriminate different ice types.

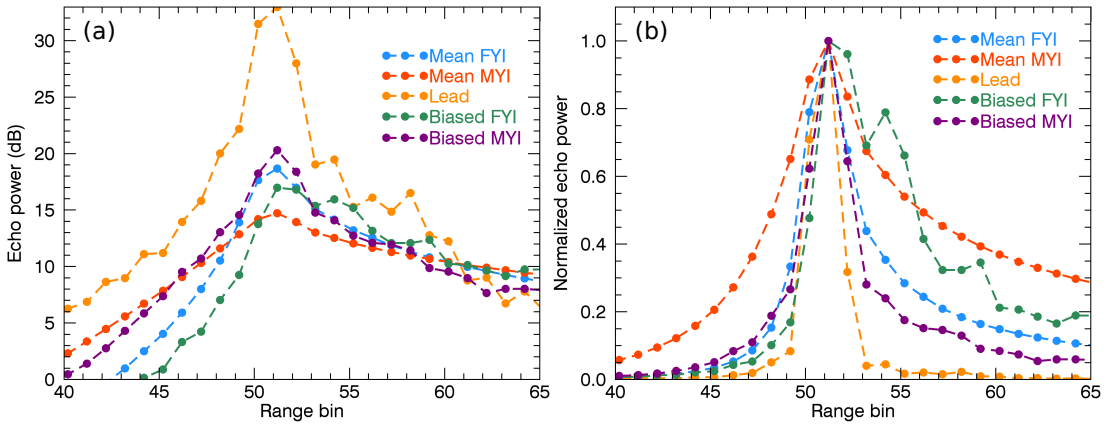

Figure 2.2. CryoSat-2 waveforms from different surface types for the CryoSat-2 ground track in Figure 2.3. The mean first-year ice (FYI) and multi-year ice (MYI) waveforms are an average of all FYI (MYI) waveforms along the track. (a) shows all waveforms aligned to the peak power in dB. (b) shows all waveforms normalized and aligned to the peak power.

2.2 Methods

Before referencing the ice elevations to the local sea level we have to assign waveforms to surface types. In this study we only focus on sea-ice and lead waveforms. Leads show an almost specular reflection due to the absence of surface waves in ice covered areas, because the surface of narrow open water areas is usually smooth. In contrast, reflections from sea ice have diffuse characteristics. Hence the echo power of a lead waveform is significantly higher than for a radar return from sea ice (Figure 2.2a). Radar returns from the open ocean can be also considered as tie points for the sea surface height but are less relevant in referencing the ice elevations because this surface type mostly occurs in the marginal ice zone. Ocean waveforms are highly affected by waves and have different characteristics.

We here use the findings of Zygmuntowska et al. (2013) and Ricker et al. (2014a) and use different waveform characteristics to discriminate between first-year ice (FYI) and multi-year ice (MYI). The pulse peakiness PP is described in Peacock and Laxon (2004) and indicates the shape of the power distribution of the waveform. Since waveforms from leads show specular returns, their PP is higher than those for sea ice with the waveform widened by diffuse reflections. The echo power contribution of an off-nadir lead is registered after the return from the nadir area but is of specular nature. Thus the retracker algorithm will fix the main scattering horizon at the leading edge of the lead. In order to identify those biased waveforms we introduce a *left-* and *right-* peakiness PP_l and PP_r (Ricker et al., 2014a). They are defined as:

Table 2.1. Waveform parameter and ice concentration thresholds used for CryoSat-2 processing to identify the surface types *Lead* and *multi-year* (MYI) and *first-year* ice (FYI): pulse peakiness PP, stack kurtosis K, stack standard deviation SSD, peakiness PP_l left of the power maximum, peakiness PP_r right of the power maximum and sea-ice concentration IC.

Surface type	PP	K	SSD	PP_l	PP_r	IC (%)
Lead	≥40	≥40	≤4	≥40	≥30	≥70
Sea ice (FYI)				≤60	≤25	≥70
Sea ice (MYI)				≤18	≤15	≥70

$$PP_r = \frac{\max(WF)}{\mathrm{mean}([WF_{i_{max}+1}, WF_{i_{max}+3}])} \cdot 3 \tag{2.1}$$

$$PP_l = \frac{\max(WF)}{\mathrm{mean}([WF_{i_{max}-3}, WF_{i_{max}-1}])} \cdot 3 \tag{2.2}$$

where WF_i is the echo power at range bin i and max(WF) the peak power of the waveform. PP_l and PP_r are a measure for the peakiness *left* and *right* of the power maximum as we consider the ratio of the maximum power to the mean power of only three range bins left and right of the maximum. In the case of a nadir lead the waveform power distribution is narrow and shows a high maximum echo power as well as high PP_r and PP_l values (Figure 2.2a and b).

For the lead identification we further use the parameter *stack kurtosis* (K), also a measure of peakiness (Wingham et al., 2006), and the *stack standard deviation* (SSD), which is a measure of the variation in surface backscatter depending on the incident angle (Wingham et al., 2006). The term *stack* refers to the multi-look SAR processing (Wingham et al., 2006). Leads are associated with a high K and a low SSD because of their specular reflection. Table 2.1 shows a set of waveform parameters used for the discrimination between sea ice and leads. The threshold values were determined by test-processing of CryoSat-2 ground tracks. All waveforms that do not comply with these constraints are discarded.

After the identification of leads, the actual sea level can be interpolated and subtracted from the CryoSat-2 elevations that were identified as sea ice. As a result we receive the radar freeboard according to Ricker et al. (2014a).

2.3 Results

Here we show exemplary results from a CryoSat-2 ground track from December 15. The track is directed south-east and first passes the MYI region north of Greenland before it passes over FYI in the marginal ice zone in the Fram Strait (Figure 2.3). For the ice-type discrimination we use the OSI SAF ice-type product (Eastwood, 2012).

Figure 2.4a reveals the range retrieval after subtracting the mean sea-surface height. Applying the waveform discrimination according to Table 2.1 we find 50 leads over a distance of 2300 km. Radar echoes with waveform parameters that do not comply with the thresholds in Table 2.1 were discarded. Overall 22 % of the FYI and 21 % of the MYI waveforms are discarded. The fraction of detected leads is 0.7 % for FYI and 0.5 % for MYI. The difference of waveform characteristics between FYI and MYI can be seen in the fact that if we use the MYI thresholds for FYI we discard 86 % of the FYI waveforms.

Figure 2.4b shows the left- and right-peakiness along the CryoSat-2 track. Within the MYI the left-peakiness reveals a mean value of 9.0 (Table 2.2) whereas for FYI we find a mean PP_l of 32.0. Furthermore the scattering for FYI is higher than for MYI. The right-peakiness PP_r shows overall less scattering compared to PP_l . It reveals mean values of 5.6 for MYI and 10.1 for FYI. The mean difference between FYI and MYI is lower than for PP_l but also shows higher values for FYI (Table 2.2). In coincidence with negative outliers in the MYI zone in Figure 2.4a we find increased values for PP_r and PP_l .

Considering the biased waveforms in Table 2.2 we find PP_l values of 21.5 for FYI and 38.7 for MYI. These values are significantly higher than the mean value for MYI, but in the range of the mean PP_l for FYI. On the other hand, the PP_r for MYI is close to the mean PP_r of the unbiased MYI waveforms.

2.4 Discussion

Waveforms from FYI and MYI are of significantly different nature, which has been already investigated in Zygmuntowska et al. (2013). Surface properties of MYI, involving snow cover and surface roughness, cause a shallow echo power distribution in the waveform whereas for FYI we find a steeper leading edge (Figure 2.2) which results in increased left- and right peakiness values (Figure 2.4b).

This finding has direct consequences for the classification of off-nadir reflections from leads that can either bias the interpolation of the sea-surface, if classified as leads, or affect the

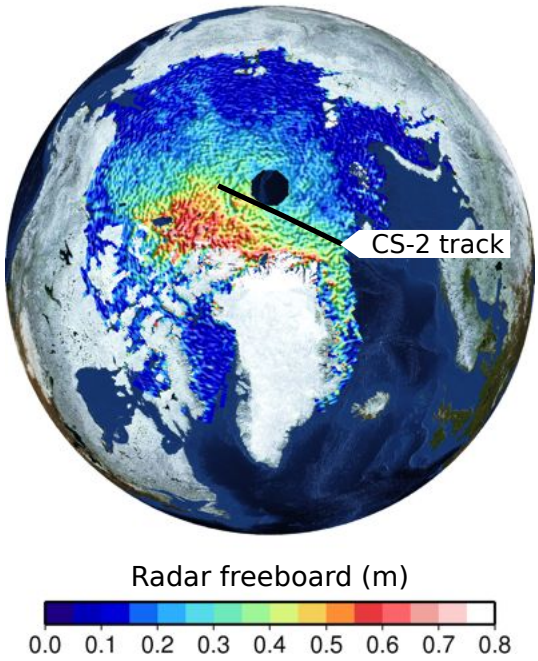

Figure 2.3. CryoSat-2 monthly mean radar freeboard from December 2013, using a 40 % retracker threshold. The black line shows the CryoSat-2 ground track that is considered in this study.

surface elevations of the sea ice, if classified as sea ice. In the first case high thresholds for the peakiness are necessary to exclude off-nadir leads. In the second case off-nadir leads cause decreased ice elevations which is shown in Figure 2.4a for example between 200 and 400 km. In the FYI zone, we do not observe a similar effect. Fig 2.2 shows biased waveforms of FYI and MYI. Both are a composition of an off-nadir lead reflection and reflections from sea ice. The biased MYI waveform shows a high left-peakiness of 38.7 while the right-peakiness is 5.2 which is close to the value for mean MYI. Here the off-nadir lead seems to dominate the peak power. Thus the waveform is dominated by the off-nadir lead reflection and the range is tracked at the leading edge of the lead waveform contribution, resulting in a range bias Δd (Figure 2.1b). Considering PP_l and PP_r allows us to characterize waveforms and to identify biased waveforms.

FYI waveforms can exhibit similar shapes and properties as biased MYI. As a consequence, FYI waveforms might be discarded if they are classified as MYI in the OSI SAF ice type.

We also note that for FYI we find fewer outliers than for MYI (Figure 2.4a). We can speculate that the backscatter from FYI is usually higher than from MYI (Figure2.2a). An off-nadir lead reflection is then in certain cases still distinguishable from the sea-ice echo as shown in Figure 2.2 (green line). We can identify two peaks where the first represents

Table 2.2. Values of left-peakiness (PP_l) and right-peakiness (PP_r) for the different surface types that are shown in Figure 2.2.

Waveform parameter	Mean FYI	Mean MYI	Lead	Biased FYI	Biased MYI
PP_l	32.0	9.0	87.2	21.5	38.7
PP_r	10.1	5.6	109.0	15.1	5.2

the sea-ice reflection and the second the off-nadir lead that is well separated from the ice waveform. Therefore the retracker algorithm captures the leading edge of the sea-ice echo correctly and hence a range bias does not occur. Therefore we can use higher thresholds of PP_l and PP_r for FYI than for MYI to avoid discarding FYI waveforms erroneously. However, another reason for fewer outliers in the FYI zone could be a different pattern and distribution of leads in the considered FYI area.

The uncertainties of the range retrieval are discussed in more detail in Ricker et al. (2014a). Besides a bias due to the choice of the retracker, the uncertainty is dominated by the speckle noise (Wingham et al., 2006; Laxon et al., 2013) that is around 0.1 m for a single measurement. Using the OSI SAF ice-type product for the waveform classification also induces a classification uncertainty (Eastwood, 2012) and might lead to an underrepresentation of FYI within the MYI zone. Therefore a combined ice-type classification using the CryoSat-2 waveforms as well as the OSI SAF ice-type product might be a reasonable approach for the future. The thresholds in Table 2.1 for FYI and MYI are empirical and where chosen considering the distribution of PP_l and PP_r in Figure 2.4b. Valid outliers in Figure 2.4a could not be identified as biased waveforms and still affect the freeboard retrieval.

2.5 Conclusion

In this study we present a method to classify CryoSat-2 waveforms using a combination of parameters that characterize the radar echo. We use a *left-* and *right-* peakiness to characterize surface types and to identify waveforms that are biased by off-nadir-leads. Those waveforms can cause a decrease in surface elevation, especially for multi-year ice while for first-year ice this bias does not have a significant effect. Therefore we used higher threshold values for the left- and right-peakiness for first-year ice to avoid discarding first-year ice waveforms erroneously. Overall we discarded 22 % of the radar echoes of a CryoSat-2 ground track from December 15, 2013. Using the multi-year ice thresholds of left- and right-peakiness for FYI would lead to a rejection of 86 % of the first-year ice waveforms because the shape of first-year ice waveforms is similar to invalid waveforms

from multi-year ice that are biased by off-nadir leads. However, since we rely on the OSI SAF ice-type product valid first-year might be underrepresented if indicated as multi-year ice.

2.6 Acknowledgements

We thank the European Space Agency for providing the CryoSat-2 data. We further thank the Earth-System Science Research-School (ESSRES) for any support during this Phd project. The work of S. Hendricks and V. Helm was funded by the 268 Federal Ministry of Economics and Technology (Grant 50EE1008). For the usage of images of *The Blue Marble: Next Generation* we thank NASA's Earth Observatory.

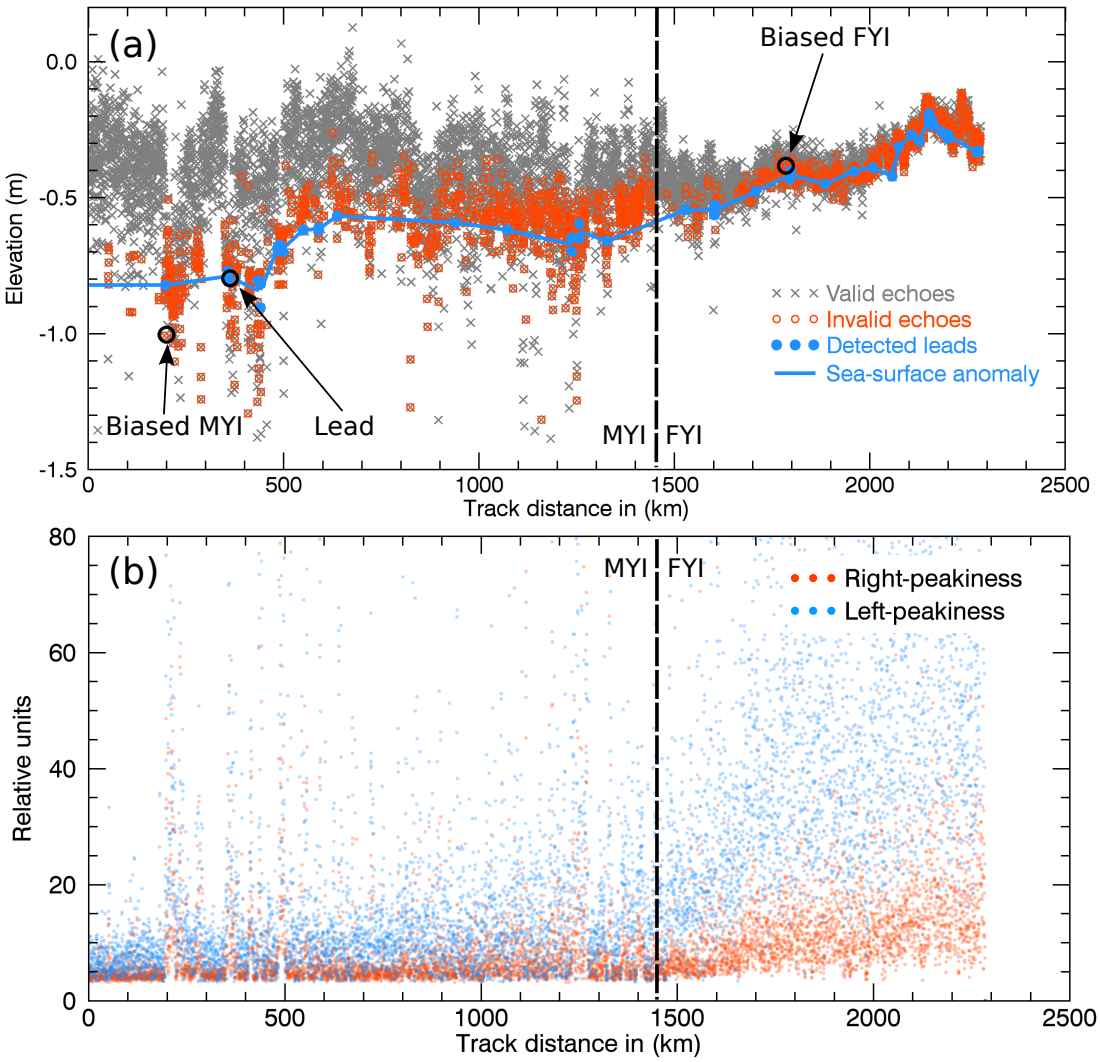

Figure 2.4. a) Geolocated CryoSat-2 surface elevations after retracking with a 40 % threshold and subtraction of the mean sea-surface height which has been interpolated along the CryoSat-2 ground track. Highlighted points belong to the waveforms in Figure 2.2. (b) Right- and left-peakiness along the CryoSat-2 ground track. The dashed vertical line marks the boundary between first- and multi-year ice.

Chapter 3

Sensitivity of CryoSat-2 Arctic sea-ice freeboard and thickness on radar-waveform interpretation

Published in *The Cryosphere*, 8, 1607-1622. doi: 10.5194/tc-8-1607-2014

R.Ricker[1], S. Hendricks[1], V. Helm[1], H. Skourup[2], and M. Davidson[3]

[1]Alfred Wegener Institute, Helmholtz Centre for Polar and Marine Research, Bremerhaven, Germany
[2]DTU Space, Copenhagen, Denmark
[3]ESA (ESTEC), Noordwijk, the Netherlands

Abstract

In the context of quantifying Arctic ice-volume decrease at global scale, the CryoSat-2 satellite was launched in 2010 and is equipped with the K_u band synthetic aperture radar altimeter SIRAL (Synthetic Aperture Interferometric Radar Altimeter), which we use to derive sea-ice freeboard defined as the height of the ice surface above the sea level. Accurate CryoSat-2 range measurements over open water and the ice surface of the order of centimetres are necessary to achieve the required accuracy of the freeboard-to-thickness conversion. Besides uncertainties of the actual sea-surface height and limited knowledge of ice and snow properties, the composition of radar backscatter and therefore the interpretation of radar echoes is crucial. This has consequences in the selection of retracker algorithms which are used to track the main scattering horizon and assign a range estimate to each CryoSat-2 measurement. In this study we apply a retracker algorithm with thresholds of 40, 50 and 80 % of the first maximum of radar echo power, spanning the range of values used in the current literature. By using the selected retrackers and additionally results from airborne validation measurements, we evaluate the uncertainties of sea-ice freeboard and higher-level products that arise from the choice of the retracker threshold only, independent of the uncertainties related to snow and ice properties. Our study shows that the choice of retracker thresholds does have a significant impact on magnitudes of estimates of sea-ice freeboard and thickness, but that the spatial distributions of these parameters are less affected. Specifically we find mean radar freeboard values of 0.121 m (0.265 m) for the 40 % threshold, 0.086 m (0.203 m) for the 50 % threshold and 0.024 m (0.092 m) for the 80 % threshold, considering first-year ice (multiyear ice) in March 2013. We show that the main source of freeboard and thickness uncertainty results from the choice of the retracker and the unknown penetration of the radar pulse into the snow layer in conjunction with surface roughness effects. These uncertainties can cause a freeboard bias of roughly 0.06–0.12 m. Furthermore we obtain a significant rise of 0.02–0.15 m of freeboard from March 2013 to November 2013 in the area for multiyear sea ice north of Greenland and Canada. Since this is unlikely, it gives rise to the assumption that applying different retracker thresholds depending on seasonal properties of the snow load is necessary in the future.

3.1 Introduction

Sea-ice thickness is an important parameter of the polar cryosphere, where changes in its seasonal cycle may cause significant negative feedbacks. There is already notable evidence of thinning of the Arctic sea ice (Rothrock et al., 1999). Together with the rapid reduction of ice-covered area (Comiso et al., 2008), especially during the summer season (Stroeve et al., 2012), the reduction of sea-ice volume in the Arctic might exceed the rate of ice extent decrease. Therefore, long-term observations of sea-ice thickness are required to assess current changes of Arctic sea-ice thickness and its implications for a further reduction of the ice cover.

Basin-scale measurements of sea-ice thickness are currently carried out by satellite altimeter missions. The altimetric sea-ice thickness retrieval is based on measurements of freeboard, the height of the ice surface above the local sea level, which can be used to calculate ice thickness (Kwok et al., 2009; Laxon et al., 2013). The radar altimeters onboard the European Remote Sensing (ERS) satellites (Laxon et al., 2003) are the first that were ever used for Arctic sea-ice thickness retrieval, followed by the Envisat mission. These pulse-limited radar altimeters had a comparably large footprint between 2 and 10 km and a latitudinal limit of 81.5° N (Connor et al., 2009). A better coverage up to 86° N was possible with the ICESat (Ice, Cloud and land Elevation SATellite) mission, which featured a laser altimeter with a significantly smaller footprint (70 m), but could be affected by clouds. The current satellite altimeter dedicated to cryospheric science is CryoSat-2, a mission of the European Space Agency (ESA), which provides improved coverage of the Arctic up to 88° N. It was launched in April 2010 and is equipped with a K_u band radar altimeter (SIRAL – Synthetic Aperture Interferometric Radar Altimeter). Its range retrieval enables the calculation of the sea-ice freeboard, which is the height of the ice surface above the actual sea level. The sea-ice freeboard can be converted into sea-ice thickness, assuming hydrostatic equilibrium (Laxon et al., 2003; Wadhams et al., 1992). Therefore it is crucial to measure the range to the main scattering horizon very accurately.

It has been suggested that K_u band radar waves do fully penetrate dry and cold snow (Beaven et al., 1995). However, field experiments indicate that snow moisture and density layering may prevent a radar from ranging through the snow to the ice surface in Arctic spring conditions over multiyear ice (MYI) (Willatt et al., 2011).

The range to the main scattering horizon is estimated at the leading edge of the radar echo waveforms (Tonboe et al., 2006). In synthetic aperture radar (SAR) altimetry, the waveform consists of a stack of collocated beams, separated from different bursts by their Doppler information. The range to the main scattering horizon is obtained by a retracker algorithm, either an empirical threshold of the peak power or an empirical approximation

of the entire waveform. Theoretical considerations of SAR altimetry suggest that the main scattering horizon is located near the peak power and not at the half power point on the leading edge, as is the case for conventional pulse-limited altimeters (Wingham et al., 2004). However, a variety of assumptions are used in the literature. Laxon et al. (2013) used a leading-edge 50 % threshold retracker, while in a recent study waveform fitting and the usage of a forward model result in an effective retracking near the waveform peak (Kurtz et al., 2014). In order to map land ice elevations, Helm et al. (2014) again focused on the lower part of the leading edge to minimize spatial and temporal variations of the volume scattering contribution. The location of the main scattering horizon below the snow surface depends significantly on the choice of the threshold or the empirical waveform fitting method. Kurtz et al. (2014) found a mean difference of 12 cm between a 50 % threshold and a waveform fitting method with a near-peak threshold during the period 2011–2013. Therefore the choice of retracker adds to the existing uncertainty of physically limited penetration due to increased moisture, ice lenses in the snow layer or stratified high-density snow. In addition, uncertainties arise due to variable footprint-scale surface roughness and inaccurate reconstruction of the local sea-surface elevation.

The conversion of freeboard to sea-ice thickness again depends on the correct knowledge of snow depth and the densities of sea ice and snow, all parameters not very well constrained by observations at basin scale. First comparisons of CryoSat-2 sea-ice thickness data (Laxon et al., 2013) with validation data from airborne experiments and moorings show a good agreement on the large scale, but scatter in the data comparison reflects the residual uncertainties cited above. Quantifying these uncertainties is essential for trend estimates in sea ice and the use of CryoSat-2 data, for example in sea-ice modelling studies, especially for data assimilation.

Here, we present CryoSat-2 freeboard and thickness retrievals with consistent uncertainty estimates in spring/autumn 2013, using different approaches for waveform interpretation. We apply three different thresholds which span the range of values found in the literature and access their impact on CryoSat-2 Arctic sea-ice freeboard and thickness retrieval. The goal of our study is to isolate and quantify the effect of SAR waveform interpretation from other uncertainties that arise from the freeboard processing and the freeboard-to-thickness conversion. We describe the methodology and compare our findings to airborne data sets and other sea-ice remote sensing products. The contributions of different uncertainty sources are analysed for their impact on the freeboard and thickness retrieval relative to assumptions to the CryoSat-2 radar echo interpretation. We therefore investigate the effect of the retracker threshold range on the magnitude of Arctic sea-ice freeboard in spring and autumn.

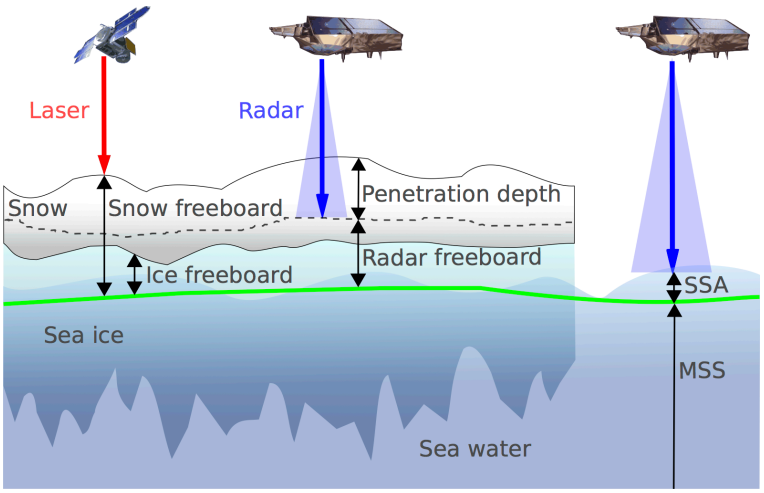

Figure 3.1. Schematic diagram of parameters regarding the CryoSat-2 freeboard and thickness processing. The actual sea-surface height is composed of the mean sea-surface height (MSS) and the sea-surface anomaly (SSA). The radar freeboard is obtained by subtracting the actual sea surface from the range retrieval over sea ice. In contrast to a laser altimeter (e.g. IceSat), the radar altimeter of CryoSat-2 can penetrate the snow cover, depending on the snow properties.

3.2 Data and methodology

3.2.1 Radar freeboard

The term sea-ice freeboard usually refers to the elevation of the snow–ice interface above the local sea level. With different altimetry sensor wavelengths we define the terminology of freeboard (Figure 3.1):

1. The ice freeboard refers to sea-ice freeboard as defined above. The lower wave propagation speed in the snow layer requires a correction based on assumed snow depth.

2. Snow freeboard: elevation of the air–snow interface, which is sensed by laser altimetry.

3. Radar freeboard: since the main scattering horizon may not coincide directly with the ice freeboard, we use the term radar freeboard for range measurements from CryoSat-2 (hereafter called CS-2). As for the ice freeboard the lower wave propagation speed in the snow layer requires a correction based on assumed snow depth and penetration, but is not applied for the radar freeboard in this study.

Figure 3.2 gives an outline of the steps in our data processing chain. To obtain radar freeboard it is necessary first to relate range estimates from the satellite to the main scattering surface. We use geolocated waveforms provided by ESA (L1b data set, baseline

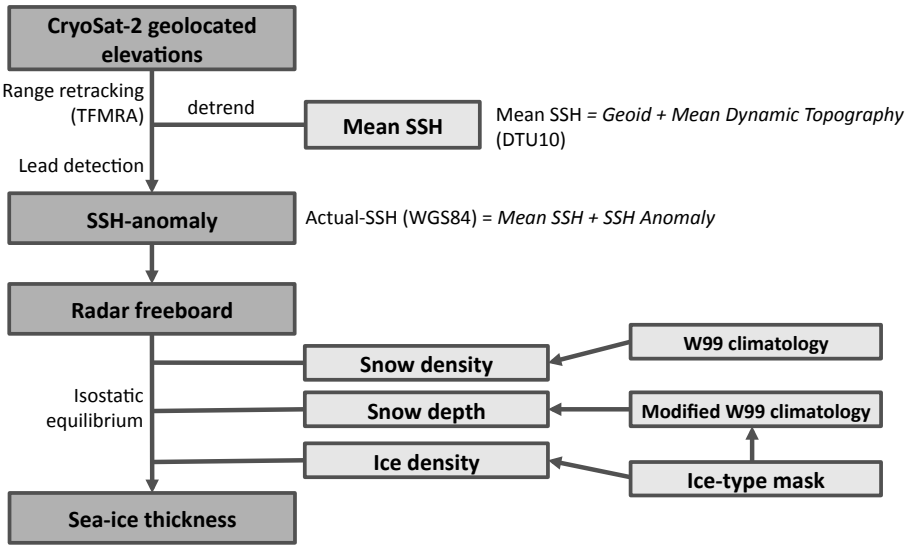

Figure 3.2. Flowchart of the CryoSat-2 data processing algorithm.

B) in both the SAR mode and the interferometric SAR (SARIn) mode which is applied in the western Arctic Ocean and coastal zones. SARIn data additionally contain phase information of the returning echo. Since they are not used in this study and to keep consistency, the phase information is discarded (Kurtz et al., 2014).

We obtain the two-way delay time of the averaged radar echoes (waveforms) by applying a TFMRA (threshold first-maximum retracker algorithm) retracker (Helm et al., 2014). First, the original waveform is oversampled by a factor of 10 and a running mean with a width of 10 bins is applied to smooth the oversampled waveform (grey line in Figure 3.3). The noise in front of the leading edge is suppressed with a power threshold. Then, the first local maximum is determined by the derivative of the curve. In the final step the leading edge of the first maximum of the waveform is tracked at a certain threshold of the maximum power of the waveform. We choose thresholds of 40 % (TFMRA40), 50 % (TFMRA50) and 80 % (TFMRA80) of the first-maximum power to simulate the assumptions in Helm et al. (2014) and Laxon et al. (2013), and to emulate the waveform fitting method used in Kurtz et al. (2014) that tracks the leading edge rather close to the peak.

We assume that the resulting range gives the distance to the main scattering horizon at the individual threshold level. Figure 3.3 shows typical CS-2 waveforms for sea ice and leads and the different applied thresholds. As a result we receive geolocated ellipsoidal elevations of CS-2 data for each orbit over sea ice.

In the following step, the mean sea-surface (MSS) height product DTU10 (Andersen, 2010) is subtracted from the geolocated surface elevations to remove the main 2features

Table 3.1. Waveform parameters and ice concentration thresholds used in the CryoSat-2 processing algorithm to discriminate between the surface types "ocean", "lead" and "sea ice": pulse peakiness (PP), stack kurtosis (K), standard deviation (SSD), peakiness left of the power maximum (PP_l), peakiness right of the power maximum (PP_r), sea-ice concentration (IC) and the width of the OCOG box (OCOG WIDTH).

	Waveform parameter						
Type	PP	K	SSD	PP_l	PP_r	IC (%)	OCOG WIDTH
Ocean	$0 \leq PP \leq 10$		≥ 18.5			≤ 5	≥ 38
Lead	≥ 40	≥ 40	≤ 4	≥ 40	≥ 30	≥ 70	
Sea ice		≤ 8			≤ 15	≥ 70	

of the actual sea-surface height. This is done to reduce errors in regions where the actual sea surface cannot be obtained with sufficient accuracy due to the absence of leads.

Then, by applying a lead detection algorithm, we automatically obtain the actual elevation of the sea level in ice-free sections of the CS-2 ground tracks. Leads between ice floes usually have far less surface waves than the open ocean and thus feature a distinct mirror-like peaky waveform. On the other hand, diffusive radar returns over snow-covered and roughened sea-ice surface lead to a wider angular distribution and a significantly different shape of the radar waveforms. Radar echoes over open ocean with higher significant wave height again show specific characteristics. In contrast to Laxon et al. (2013) we use the same retracker for both leads and sea ice to avoid biases due to the usage of different retracker algorithms.

This surface-type dependance of radar waveforms is traditionally used to automatically classify leads in the ice pack (Laxon, 1994; Drinkwater, 1991). We consider several waveform parameters that are either available in the raw data files or can be computed from the waveforms. Table 3.1 gives an overview of these parameters and their assumed threshold values which are used to distinguish between the surface types "ocean", "lead" and "sea ice". The surface type lead may not represent a single, large lead, but a sea-ice surface that typically includes a few small leads within the footprint. We use the "pulse peakiness" PP that has already been described in Giles et al. (2008) and Peacock and Laxon (2004). It has to be noted that we used a slightly different notation of the pulse peakiness in contrast to Laxon et al. (2013):

$$\mathrm{PP} = \sum_{i=1}^{N_{\mathrm{WF}}} \frac{\max(\mathrm{WF})}{\mathrm{WF}_i} \cdot N_{\mathrm{WF}}. \tag{3.1}$$

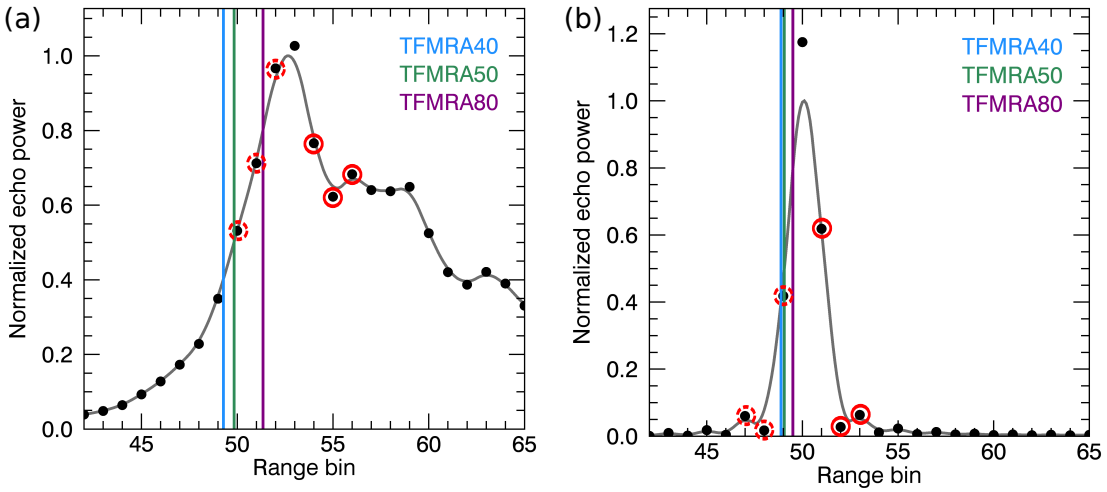

Figure 3.3. Typical CryoSat-2 waveforms for sea ice **(a)** and leads **(b)**. The fitted waveform (grey) is a result of linear interpolation and smoothing of the original CryoSat-2 waveform (black dots). The coloured vertical lines represent the different applied TFMRA (threshold first-maximum retracker algorithm) thresholds in this study: 40 % (TFMRA40), 50 % (TFMRA50) and 80 % (TFMRA80). Red circles mark the range bins that are considered for the "left-hand" (dotted) and "right-hand" peakiness (solid).

Here N_{WF} represents the number of range bins and WF_i the echo power at range bin index i. Thus PP can be transferred to values in Laxon et al. (2013) by multiplication with a factor of $1/N_{\mathrm{WF}}$. The second parameter is the "stack kurtosis" (K), which is a measure of peakiness of range-integrated stack power distribution (Wingham et al., 2006). Here the term "stack" refers to an assembly of beam echoes which steer to a fixed point on the surface from different bursts. Specular reflections (narrow waveforms) from leads cause a high pulse peakiness as well as a small kurtosis. In contrast, echoes from sea ice are defined by waveforms with a wider power distribution and thus a lower peakiness. Further, the "stack standard deviation" (SSD) provides a measure of the variation in surface backscatter with incidence angle of the different beam echoes that are stacked (Wingham et al., 2006). Off-nadir reflections from leads can bias the range retrieval, since only a little area is required in the radar footprint to dominate the waveform (Armitage and Davidson, 2014). Because those echoes do not show the typical specular reflection, they are discarded by introducing a modified pulse peakiness which considers only three range bins on the "left" ($\mathrm{PP_l}$) and on the "right" ($\mathrm{PP_r}$) of the power maximum of a waveform (Figure 3.3):

$$\mathrm{PP_r} = \frac{\max(\mathrm{WF})}{\mathrm{mean}([\mathrm{WF}_{i_{\max}-3}, \mathrm{WF}_{i_{\max}-1}])} \cdot 3, \tag{3.2}$$

$$\mathrm{PP_l} = \frac{\max(\mathrm{WF})}{\mathrm{mean}([\mathrm{WF}_{i_{\max}+1}, \mathrm{WF}_{i_{\max}+3}])} \cdot 3. \tag{3.3}$$

For the coarse discrimination between ocean and sea-ice area (including leads), we use interpolated ice concentration from the daily Ocean and Sea Ice Satellite Application Facility (OSI SAF) ice concentration product (Eastwood, 2012). To identify echoes from the ocean we additionally consider the "OCOG WIDTH", which is derived from the algorithm of the offset centre-of-gravity (OCOG) retracker (Wingham et al., 1986). It provides information about the "width" of the echo. Surface waves on the ocean cause a high OCOG WIDTH which can be used for the surface-type discrimination. Radar echoes that are not assigned to one of the surface types – ocean, lead or sea ice – are assumed to be biased by off-nadir leads and hence are discarded.

3.2.1.1 Sea-surface anomaly

The surface-type classification parameters were initialized based on manual tuning of example CS-2 ground tracks where coincident aircraft validation data (see Sect. 3.2.5) were available. We use a linear interpolation on the ranges of the retrieved open-water spots from leads. We then apply a running mean with 25 km width as a low-pass filter to smooth jumps that occur in dense lead clusters due to the signal noise. This procedure is done for each CS-2 track, yielding the sea-surface anomaly (SSA), the deviation of the actual sea-surface elevation from the mean sea-surface height (Figure 3.1).

As the next step, the remaining anomaly from the mean sea-surface height (sea-surface anomaly), which is obtained by the interpolated lead elevations, is subtracted from the retracked surface elevations L, which were identified as sea ice in the surface-type discrimination. This is done for every single CS-2 track. The radar freeboard (F_R), which is not corrected for the lower wave propagation speed in the snow layer, is then obtained by

$$F_\mathrm{R} = L - (\mathrm{MSS} + \mathrm{SSA}). \tag{3.4}$$

We finally only allow freeboard values within the interval $-\sigma_{l1b} < F_\mathrm{R} < 2\,\mathrm{m} + \sigma_{l1b}$, where σ_{l1b} is the speckle noise (see Sect. 3.2.3) that represents random uncertainty of the range measurement and therefore should represent the lower boundary.

3.2.2 Sea-ice thickness

We consider the ice freeboard as a function of the radar freeboard (F_R), corrected by the penetration depth (c_p), a bias (c_r) due to surface roughness effects and c_w, the correction

for the lower wave propagation speed in the snow layer:

$$F_{\mathrm{I}} = \alpha F_{\mathrm{R}} + c_{\mathrm{p}} + c_{\mathrm{r}} + c_{\mathrm{w}}, \tag{3.5}$$

where α is a factor that represents the uncertainty due to the choice of the retracker threshold. Considering the fact that the values of α, c_{p}, c_{r} and c_{w} are uncertain, we do not apply correction terms in this study to get a consistent comparison. Therefore we assume that the uncorrected radar freeboard F_{R} represents the ice freeboard F_{I}. Nevertheless correction terms have been applied for the AWI (Alfred Wegener Institute) CS-2 freeboard and thickness product (revision 1.0), which is available to the public (Hendricks et al., 2013).

The radar freeboard (F_{R}) can be converted into sea-ice thickness T depending on the snow depth (S) and the densities of snow (ρ_{S}), sea ice (ρ_{I}) and sea water (ρ_{W}):

$$T = F_{\mathrm{R}} \cdot \frac{\rho_{\mathrm{W}}}{\rho_{\mathrm{W}} - \rho_{\mathrm{I}}} + S \cdot \frac{\rho_{\mathrm{S}}}{\rho_{\mathrm{W}} - \rho_{\mathrm{I}}}. \tag{3.6}$$

Corresponding to Laxon et al. (2013), we use the modified Warren snow climatology (W99) to estimate the snow depth (Warren et al., 1999) in the absence of year-round snow-depth observations for the entire Arctic Ocean. The climatology is based on observations from drift stations in a period where the Arctic Ocean was dominated by multiyear sea ice. It is therefore likely that the reduction of multiyear sea ice in the recent decade (Nghiem et al., 2007) may have impacted the distribution of snow depth in areas that are now more often covered by seasonal sea ice. Based on data from an airborne snow-depth radar, Kurtz and Farrell (2011) suggest that, though W99 is still representative for multiyear ice, snow depth has to be reduced in first-year ice (FYI) regions by 50 %. We follow this approach and classify the ice cover in first-year and multiyear sea ice using the daily ice-type product from OSI SAF (Eastwood, 2012) and apply the snow-depth reduction accordingly. This step was introduced by Laxon et al. (2013) for CS-2 data processing. We additionally use the confidence level that is provided in the ice-type product to allow a mixture of both types at the boundaries.

The snow density (ρ_{S}) is adopted from the Warren snow water equivalent climatology (Warren et al., 1999). Both snow depths and snow density are available as a monthly product. Consistent with the approach of Laxon et al. (2013) we use ice densities (ρ_{I}) of $916.7\,\mathrm{kg\,m^3}$ for first-year ice (FYI) and $882.0\,\mathrm{kg\,m^3}$ for MYI (Alexandrov et al., 2010). Furthermore we assume a value of $1024\,\mathrm{kg\,m^3}$ for the water density (ρ_{W}).

The freeboard-to-thickness conversion is applied for each individual CS-2 ground track. We calculate ice thickness from an individual data point and not from a larger-scale

averaged snow freeboard in order to allow estimation of individual uncertainties of retrieved thickness after later spatial downsampling.

3.2.3 Uncertainty of freeboard and thickness

We consider two sources of uncertainties:

1. Random uncertainties that originate from random fluctuations during the measurement and usually can be minimized by increasing the number of measurements.
2. A bias or systematic uncertainty has a assignable cause and the same magnitude for all measurements and thus cannot be reduced by averaging.

In Wingham et al. (2006) different types of errors from CS-2 measurements over sea ice have already been discussed. The first of which are errors that affect the range measurements, e.g. speckle noise. Second, the uncertainty of the actual sea-level height (MSS + SSA), which affects the freeboard retrieval through Eq. (3.4). Third, there is uncertainty as to the location of the reflection horizon depending on the physical properties of the snow cover. It can be combined with the uncertainty of the choice of the retracker threshold. Furthermore there are contributions which arise from uncertainties in densities of the sea-ice layer and snow loading, directly affecting the thickness retrieval through Eq. (3.6). Finally Wingham et al. (2006) considered potential high-level errors due to limited recording of thin ice ($< 1\,\mathrm{m}$). However this was observed for pulse-limited radar altimetry and is still not clarified for CS-2 (Laxon et al., 2013).

Figure 3.4 provides an overview of all individual uncertainties that are incorporated into the freeboard and thickness uncertainty budget in this study. We acknowledge that this is only an approximation resulting from incomplete knowledge of the covariance of individual error contributions.

The random uncertainty of radar freeboard is assumed to be governed by the speckle noise and the accuracy of the actual sea-surface height. The latter depends on the abundance of detected leads, which are needed for an accurate interpolation of the sea-surface anomaly. These two uncertainties are considered to be uncorrelated.

According to Wingham et al. (2006), the speckle noise that originates from instrument system errors is assumed to be $\sigma_{l1b} = 0.10\,\mathrm{m}$ for SAR mode and $\sigma_{l1b} = 0.14\,\mathrm{m}$ for SARIn mode. It affects the lead elevations as well as the ice floe elevations. The lead coverage is variable, depending on season, region and ice type. The SSA uncertainty (σ_{SSA}) is computed by taking the standard deviation of the detected lead elevations within a moving 25 km window. In the absence of leads inside the moving window the uncertainty is given by the deviation of the interpolated SSA from the mean CS-2 elevation. As a consequence

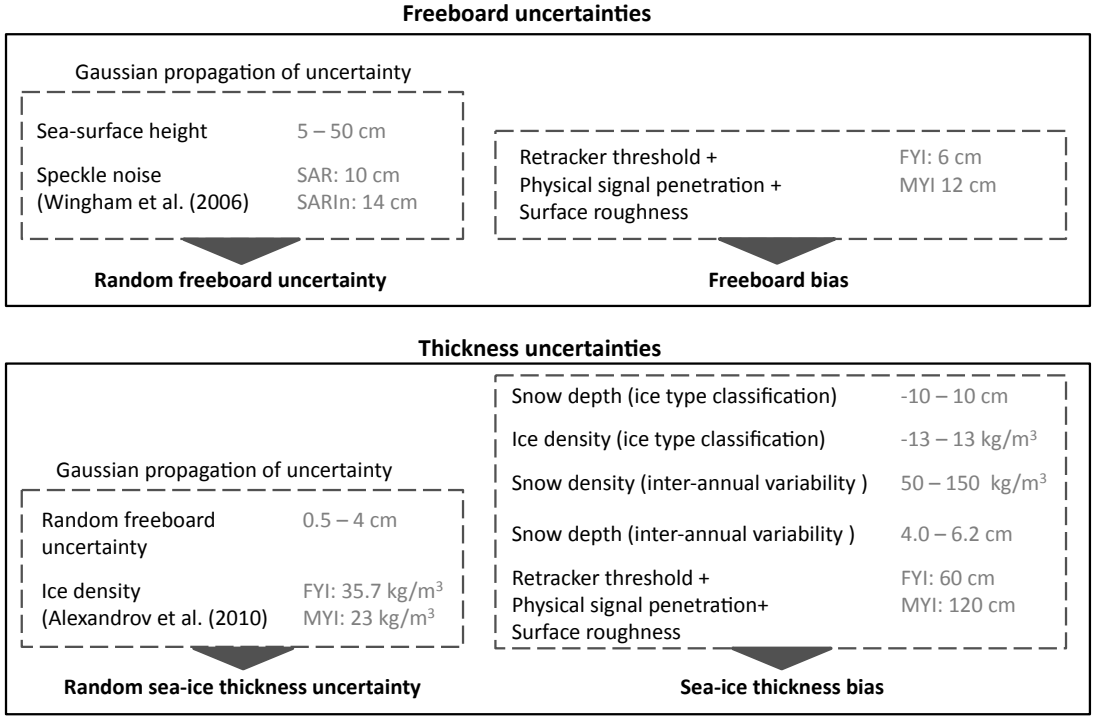

Figure 3.4. Flowchart of the CryoSat-2 uncertainty budget for freeboard and thickness, showing the typical range for the individual uncertainty of each parameter and referring to a single CryoSat-2 measurement.

it rises with decreasing density of detected leads along a CS-2 ground track. We can then estimate the uncertainty of an individual radar freeboard measurement by adding the variances (Figure 3.4):

$$\sigma^2_{F_\mathrm{R}} = \sigma^2_{l1b} + \sigma^2_{\mathrm{SSA}}. \tag{3.7}$$

The choice of the retracker threshold in conjunction with the incomplete knowledge about the penetration of the radar pulse and the effect of surface roughness causes a bias which affects all measurements in the same way. We quantify this bias by comparing the results of using different retracker thresholds.

For the sea-ice thickness uncertainty we again separate between random uncertainties and biases (Figure 3.4). The random uncertainties are assumed to be uncorrelated an can be combined via Gaussian propagation of uncertainty. For both types of uncertainties we have to calculate the partial derivatives of Eq. (3.6) as weights for the variances of the

single variables to get the contribution to the thickness uncertainty:

$$\begin{aligned}\frac{\partial T}{\partial F_\mathrm{R}} &= \frac{\rho_\mathrm{W}}{\rho_\mathrm{W}-\rho_\mathrm{I}} \\ \frac{\partial T}{\partial \rho_\mathrm{S}} &= \frac{S}{\rho_\mathrm{W}-\rho_\mathrm{I}} \\ \frac{\partial T}{\partial \rho_\mathrm{I}} &= \frac{F_\mathrm{R}\cdot\rho_\mathrm{W}+S\cdot\rho_\mathrm{S}}{(\rho_\mathrm{W}-\rho_\mathrm{I})^2} \\ \frac{\partial T}{\partial S} &= \frac{\rho_S}{\rho_\mathrm{W}-\rho_\mathrm{I}}.\end{aligned} \tag{3.8}$$

The random thickness uncertainty of an individual measurement can then be determined by

$$\sigma_T^2 = \left(\frac{\partial T}{\partial F_\mathrm{R}}\cdot\sigma_{F_\mathrm{R}}\right)^2 + \left(\frac{\partial T}{\partial \rho_\mathrm{I}}\cdot\sigma_{\rho_\mathrm{I}}\right)^2 \tag{3.9}$$

using the result for the random uncertainty (σ_{F_R}) of radar freeboard (Eq. 3.7) and the uncertainty of ice density (σ_{ρ_I}) that is adopted from Alexandrov et al. (2010) and is assumed to be 35.7 $\mathrm{kg\,m^3}$ for FYI and 23.0 $\mathrm{kg\,m^3}$ for MYI. The contribution of uncertainties due to the variability of water density is neglected (Kurtz et al., 2013).

Further uncertainties concerning the thickness retrieval are considered as biases and do not decrease due to averaging. As for the freeboard, the choice of the retracker threshold in conjunction with the incomplete knowledge about the penetration of the radar pulse and the effect of surface roughness also affects the thickness retrieval. Furthermore the uncertainties of the modified W99 snow depth and snow density due to interannual variabilities are assumed to be systematic and cannot be treated as random uncertainties. Therefore we use the interannual variability of snow depth and snow water equivalent, provided in Warren et al. (1999), to access this potential bias. The OSI SAF ice-type product is applied to form the modified W99 snow depth and the ice density field. The ice-type product is provided with a confidence level that is used as a measure of uncertainty. A wrong ice-type classification biases both the snow depth and the ice density.

Each of the systematic uncertainties is multiplied with the partial derivative of the respective variable (Eq. 3.8) to obtain the contribution to the thickness uncertainty.

3.2.4 Gridding

Including radar freeboard, snow depth, sea-ice thickness and all auxiliary data products, data for 1 month are averaged on the EASE-Grid 2.0 (Brodzik et al., 2012) with a resolution of 25 km. For averaging radar freeboard and thickness we use the weighted

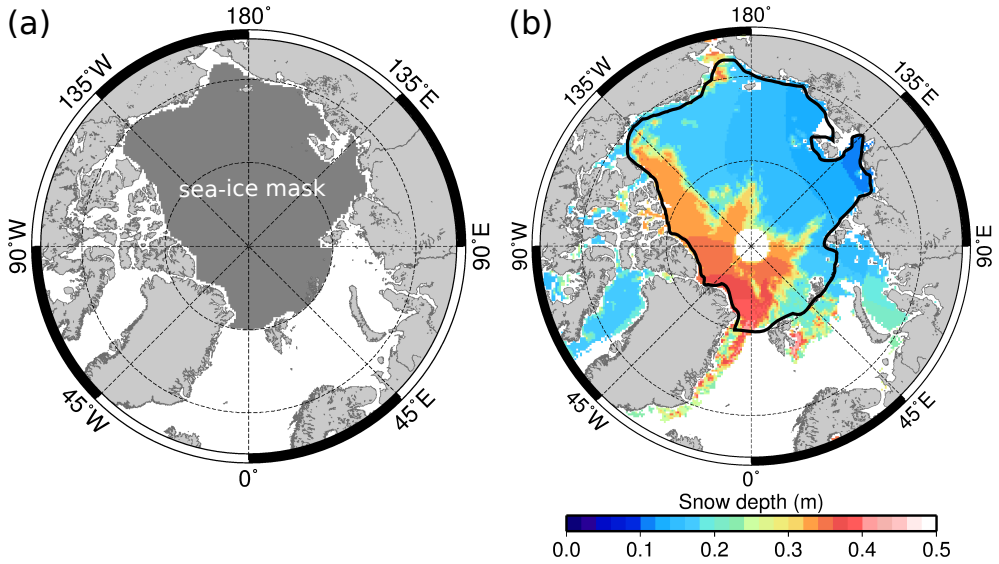

Figure 3.5. **(a)** Data mask, which is applied to calculate sea-ice thickness estimates. Only thickness data within the dark grey area are considered as valid. **(b)** Snow depth from March 2011 and data mask (solid black line). Thickness data in excluded regions are discarded because the W99 snow-depth fit is not valid there.

arithmetic mean, which is calculated from all processed data points within the boundaries of a grid cell. As weights we use the squares of the individual random uncertainties. For mean radar freeboard ($\bar{F}_{\mathrm{R}}$) and mean sea-ice thickness ($\bar{T}$), each grid cell represents the mean value of data points classified as sea ice only, without the open-water fraction:

$$\bar{F}_{\mathrm{R}}, \bar{T} = \frac{\sum_{i=1}^{N} \frac{1}{\sigma^2_{[F_{\mathrm{R}_i}, T_i]}} \cdot [F_{\mathrm{R}_i}, T_i]}{\sum_{i=1}^{N} \frac{1}{\sigma^2_{[F_{\mathrm{R}_i}, T_i]}}}, \tag{3.10}$$

where N is the number of CS-2 freeboard and thickness measurements inside a grid cell. Due to monthly averaging the random uncertainties of the individual measurements decrease with $\sqrt{N}$, leading to the random freeboard and thickness uncertainties of a grid cell:

$$\sigma_{\bar{F}_{\mathrm{R}}, \bar{T}} = \sqrt{\frac{1}{\sum_{i=1}^{N} \frac{1}{\sigma^2_{[F_{\mathrm{R}_i}, T_i]}}}}. \tag{3.11}$$

Since the W99 climatology is based upon in situ measurements (Warren et al., 1999), regions without sampling or with insufficient sampling should be excluded. Therefore we provide a sea-ice mask but exclude certain regions, e.g. Baffin Bay, the Canadian Arctic Archipelago and the region between Greenland and Severnaya Zemlya below 80° N (Figure 3.5a). Figure 3.5b shows the data mask and an example of a monthly average snow-depth field from March 2011.

3.2.5 Airborne data

The penetration of the radar pulse, the effect of surface roughness as well as the choice of the retracking point are still under investigation. Laser altimetry is a valuable technique for their evaluation because it is always referring to the snow freeboard (Figure 3.1).

Since 2003 the CryoSat Validation Experiment (CryoVex) has been carried out over sea ice in the Northern Hemisphere to directly validate CS-2 products. During the CryoVEx campaign in the Lincoln Sea in spring 2011 the first coincident measurements by CS-2 and two research aircraft were accomplished. Besides other sensors a laser scanner was mounted onboard the AWI aircraft "Polar 5".

Airborne laser scanners (ALSs) provide high-precision and high-resolution measurements and thus are capable of evaluating measurements of the radar altimeter SIRAL on CryoSat-2. The accuracy for the range measurements is about a few centimetres. The main limitation is due to GPS positioning, especially for a longer baseline of more than 100 km (Forsberg et al., 2002).

The laser scanner has been operated at an altitude of 300 m with around 370 shot points per scan line and a point spacing of around 0.3 m. The spacing along track has been around 1 m. We include two flights in our analysis where we consider profile sections with a total length of about 450 km in coincidence with CS-2. They were conducted over the Lincoln Sea on 15 and 17 April, operated from the Canadian Forces Station Alert (Figure 3.6a and Figure 3.7a).

Consistent with the CS-2 processing, the geolocated ALS elevations have to be referenced to the actual sea-surface height. Therefore leads are picked manually from the ALS elevation model. The sea-surface height is then determined along the centre shot points by applying a spline interpolation. The snow freeboard is obtained by subtracting the sea-surface height from the geolocated ALS elevations.

In the following step ALS data are averaged over the respective CS-2 Doppler cell, which is assumed to cover an area of 300 m by 1000 m. In order to provide a consistent comparison with CS-2 measurements, the ALS data points are weighted, depending on the distance to the respective CS-2 data point, which we assume to be located in the centre of the CS-2 Doppler cell. The averaging process is applied to accommodate the footprint geometry and therefore the coarser-resolution CS-2 measurements. Finally every averaged value of the ALS data is assigned to a corresponding CS-2 data point.

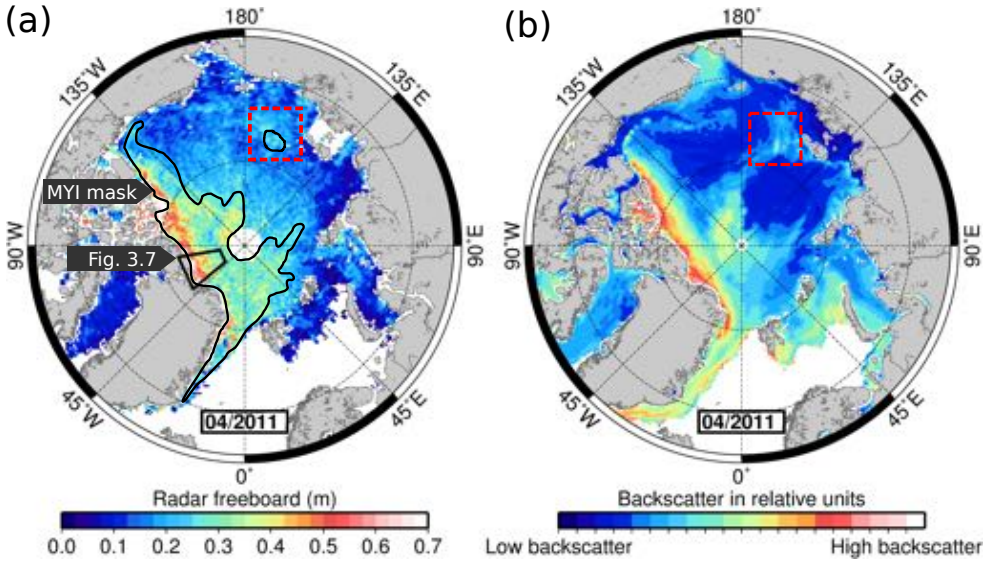

Figure 3.6. **(a)** CryoSat-2 mean radar freeboard of April 2011, retrieved by applying the TFMRA40 retracker. It shows the area of coincident validation flights in April 2011 (black box; see Figure 3.7). **(b)** METOP ASCAT mean backscatter for April 2011. The red dashed box marks a common feature of **(a)** and **(b)**.

3.3 Results

In this section we first describe the results from the CS-2 freeboard processing. Then we consider results of the performance of different CS-2 retracker thresholds and their differences, also using airborne laser altimetry as a reference. Finally contributions of uncertainties in the waveform interpretation are considered in the context of additional random and systematic uncertainties.

3.3.1 Radar freeboard retrieval

Figure 3.6a shows the CS-2 mean radar freeboard retrieval from April 2011 using the TFMRA40 retracker. We find a mean radar freeboard of 0.3 m in the MYI region north of Greenland and Canada and a mean radar freeboard of 0.16 m for FYI. For the discrimination between FYI and MYI we use a monthly mean ice-type product. This originates from the CS-2 data processing where OSI SAF ice-type data are interpolated along each CS-2 ground track. As for the CS-2 freeboard and thickness retrieval, the interpolated ice-type data are averaged on the EASE-Grid 2.0 over 1 month.

Figure 3.6b shows a monthly mean of backscatter from April 2011, obtained from the Advanced Scatterometer (ASCAT) onboard the Meteorological Operational Satellite. The backscatter is affected by the dielectric properties of the snow and the surface roughness

that both change with the ice type. High backscatter indicates a rather rough surface and is usually associated with MYI, whereas low backscatter rather indicates younger FYI. A slightly increased freeboard can be observed in the East Siberian Sea. It occurs as higher backscatter (red dashed square). Together with Special Sensor Microwave Imager (SSM/I) passive microwave radiometer, MESOP ASCAT backscatter is also an input for the OSI SAF ice-type classification that is used to build the modified W99 snow depth as well as the ice density field.

3.3.2 Comparison with airborne laser altimetry (ALS)

Figures 3.7 and 3.8 show ALS snow freeboard and uncorrected CS-2 radar freeboard F_{R} for different retracker thresholds. Gaps in Figure 3.7b originate from discarded CS-2 data that were biased by off-nadir leads, insufficient retracking or poor quality in the ALS data. We additionally smoothed all data sets with a running mean of 10 km width to reduce noise and small-scale artefacts. The along-track comparison in Figure 3.7b shows some long-scale agreement of the freeboard gradient, particularly between 150 and 200 km track distance on ground track 5428. This applies to all of the three threshold retrievals. Nevertheless the magnitude of variations in the ALS retrieval is higher than in the CS-2 freeboard.

The TFMRA40 freeboard is the closest to the snow freeboard. The mean difference to the snow surface is 0.21 m. The TFMRA50 freeboard is 0.1 m below the TFMRA40 freeboard on average. Both show very similar magnitudes of variations. This is also shown in the corresponding probability density functions in Figure 3.8. Here we use a relative probability that reveals the modal freeboard as the peak of the function which represents the level ice. The tail represents the fraction of deformed ice.

In contrast to the 40 and 50 % threshold retrievals, the TFMRA80 is very close to the sea level and deviates by a mean distance of 0.52 m to the snow freeboard. It also shows less variation in magnitude, resulting in a narrow distribution (Figure 3.8).

3.3.3 Freeboard and thickness from different retracker thresholds and uncertainties

Figure 3.9 shows the uncorrected radar freeboard from March and November 2013 for each threshold. Similar to Figure 3.6 we find a significant increase of freeboard for the MYI north of Greenland and Canada of up to 0.55 m (40 %), 0.45 m (50 %) and 0.3 m (80 %), whereas FYI regions (e.g. East Siberian Sea) are characterized by a lower radar

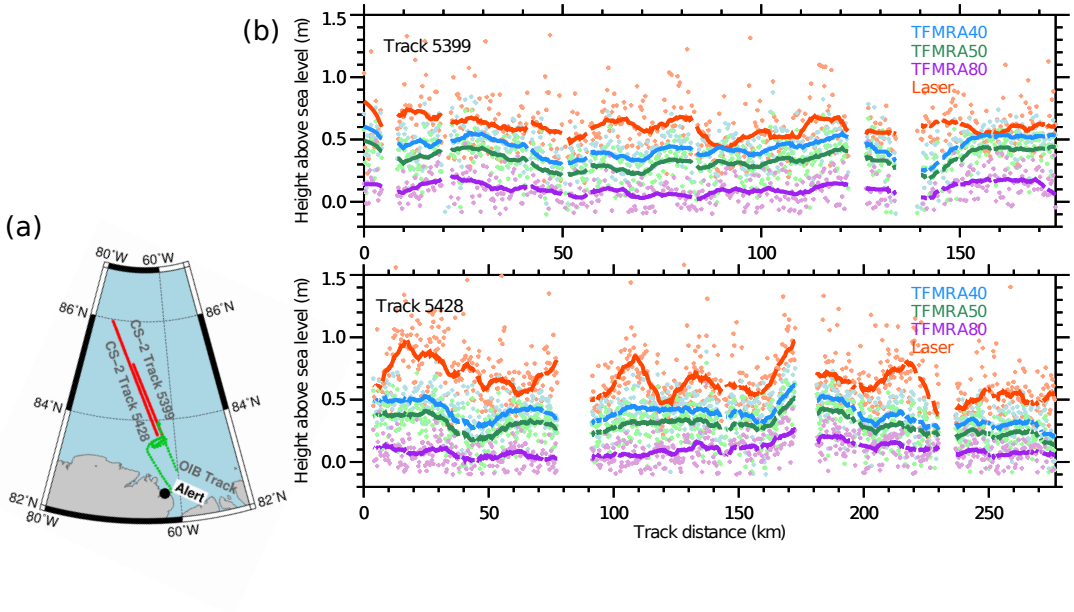

Figure 3.7. **(a)** Area of coincident flights of CryoSat-2 (CS-2) and Polar-5 (black box in Figure 3.6) from 15 and 17 April 2011. The green dotted line shows the track of Operation IceBridge (OIB) flight 1038 that carried a snow-depth radar. The aircraft surveyed the ascending CryoSat-2 tracks from the southeast to the northwest. **(b)** Uncorrected TFMRA40, TFMRA50 and TFMRA80 radar freeboard of CryoSat-2 and snow freeboard from airborne laser altimetry ("Laser") along CryoSat-2 tracks 5399 and 5428. For the comparison only valid data from coincident coverage are considered. The dots represent the original data with a spatial resolution of 300 m. We additionally applied a running mean (10 km width, solid lines).

freeboard, especially in November. The patterns are similar for all applied thresholds, but with different magnitudes.

Figure 3.10 shows the random uncertainties corresponding to Figure 3.9. They result from Eqs. (3.7) and (3.11) and show a latitude-dependent gradient. The mean uncertainties for FYI and MYI do not differ significantly and are between 0.01 and 0.04 m except for the ice edge and land-fast ice regions (e.g. Laptev Sea), where they can reach 0.07 m. Magnitude and pattern of the random freeboard uncertainties are very similar for all applied thresholds.

Table 3.2 summarizes the corresponding mean values classified into FYI and MYI for the use of different thresholds. Considering the results of the TFMRA40 retracker, we find a mean radar freeboard of 0.12 m (0.25 m) for FYI (MYI) in March and 0.08 m (0.26 m) for FYI (MYI) in November. In comparison to the TFMRA40, the TFMRA50 mean radar freeboard is decreased by 0.04 m (0.06 m) for FYI (MYI) in March 2013 and 0.03 m (0.07 m) for FYI (MYI) in November 2013. Considering the TFMRA80 mean radar freeboard, we find a significant decrease in comparison to the retrievals from using the

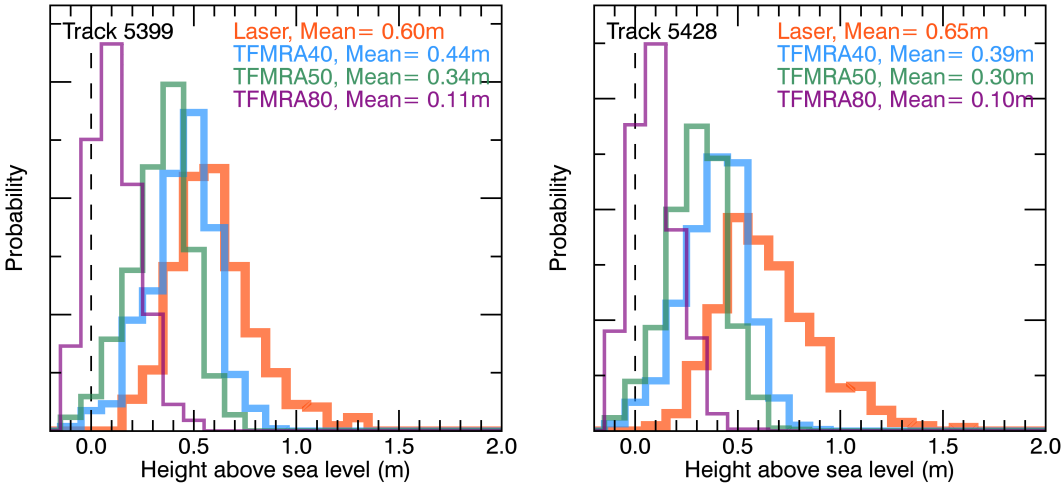

Figure 3.8. Probability density functions corresponding to Figure 3.7b. For the comparison only valid data from coincident coverage are considered.

Table 3.2. Mean radar freeboard F_R of gridded data for March and November 2013, discriminated between first-year ice (FYI) and multiyear ice (MYI).

	March 2013		November 2013	
	FYI (m)	MYI (m)	FYI(m)	MYI (m)
TFMRA40	0.121	0.247	0.077	0.257
TFMRA50	0.086	0.187	0.048	0.190
TFMRA80	0.025	0.076	-0.004	0.065

other thresholds. The TFMRA80 mean radar freeboard is decreased by 0.10 m (0.17 m) for FYI (MYI) in March and 0.08 m (0.19 m) for FYI (MYI) in November compared to the TFMRA40 retrieval. Furthermore the mean radar freeboard for FYI of November 2013 shows a value which is negative and close to the sea level.

Figure 3.11 shows the spatial differences between the freeboard retrievals from using 40, 50 and 80 % thresholds. Consistent with the mean differences in Table 3.2, we find only small differences in the range of 0.05 m for FYI and up to 0.1 m for MYI between the 40 and the 50 % threshold retrievals. Nevertheless the MYI pattern is slightly visible (Figure 3.11a). In contrast the difference magnitudes between the 40 % threshold and the 80 % threshold are higher and reach 0.15 m for FYI and 0.3 m for MYI (Figure 3.11b). Besides the ice-type pattern there is also a visible gradient within the MYI, showing higher differences north of Greenland of up to 0.35 m.

Figure 3.12a shows the sea-ice thickness estimate from March and November 2013 together with the corresponding uncertainty maps (Figure 3.12b), using the 50 % threshold. Areas where the W99 climatology is not valid have been excluded (Figure 3.5). The spatial

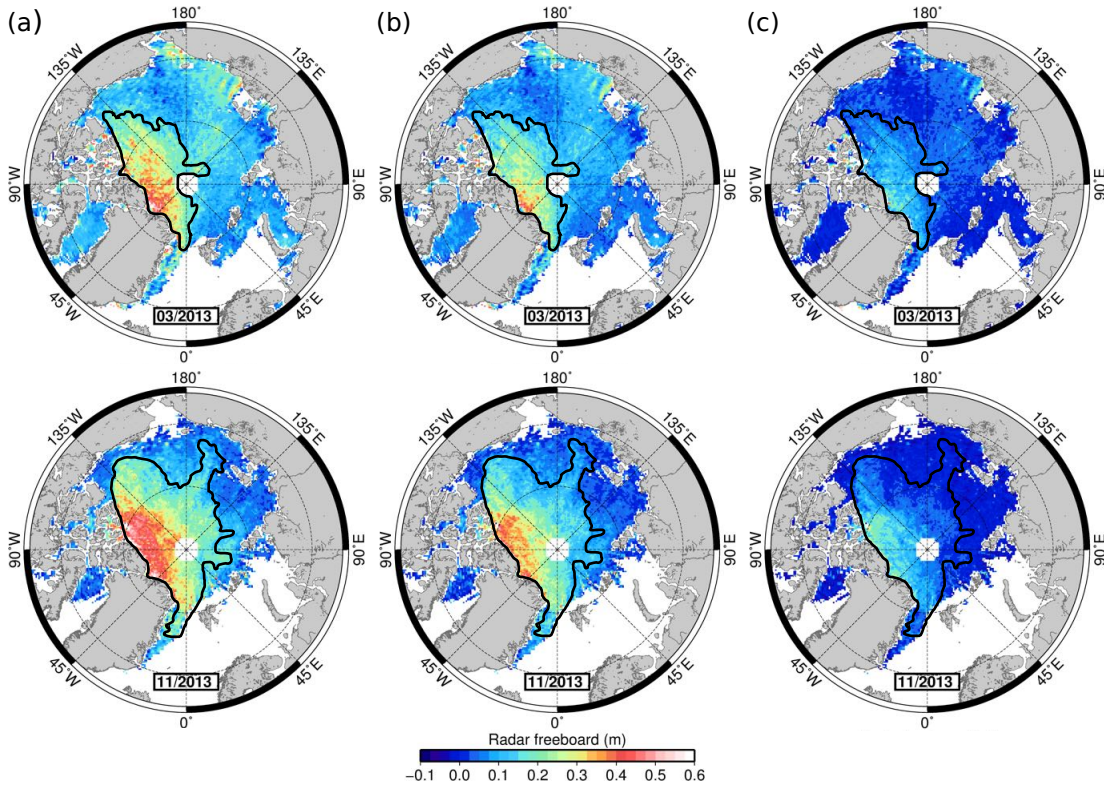

Figure 3.9. Radar freeboard from different TFMRA (threshold first-maximum retracker algorithm) retracker thresholds for March (upper row) and November (lower row) 2013: **(a)** 40 %, **(b)** 50 % and **(c)** 80 % threshold. The black polygon defines the averaged MYI zone, retrieved from the OSI SAF ice-type product.

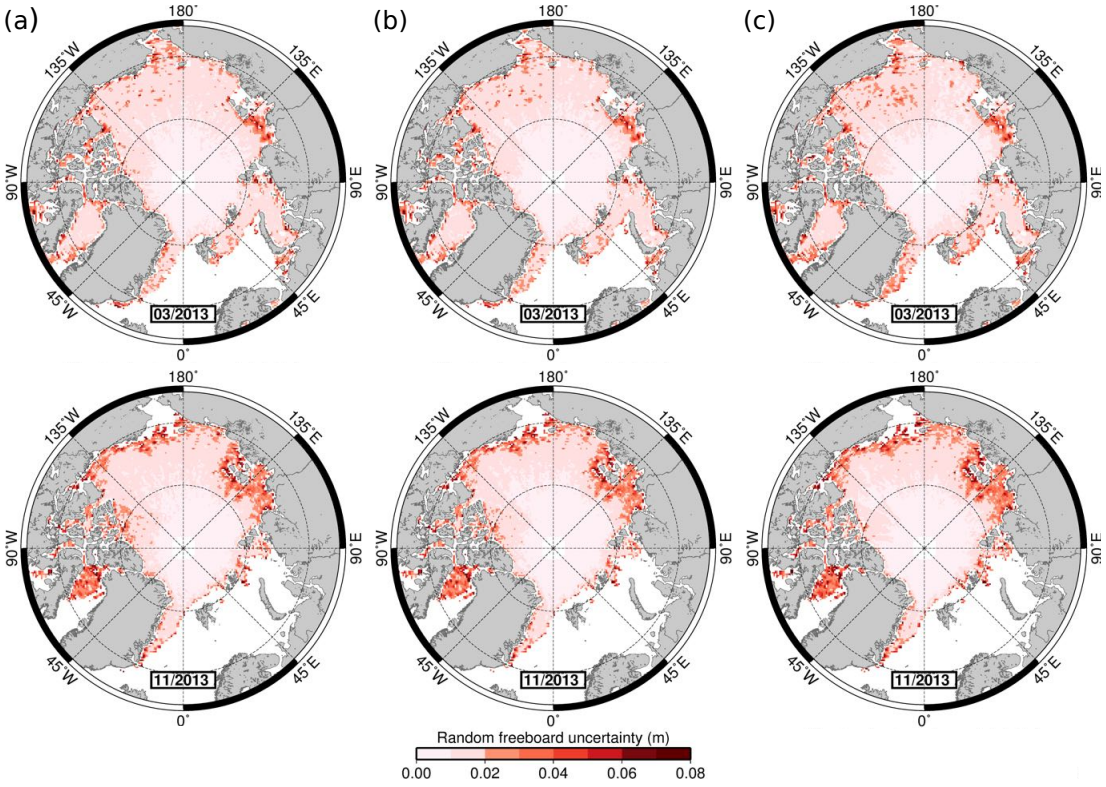

Figure 3.10. Random freeboard uncertainties corresponding to Figure 3.9: **(a)** TFMRA40, **(b)** TFMRA50 and **(c)** TFMRA80. The uncertainties result from Gaussian propagation of uncertainty (Figure 3.4).

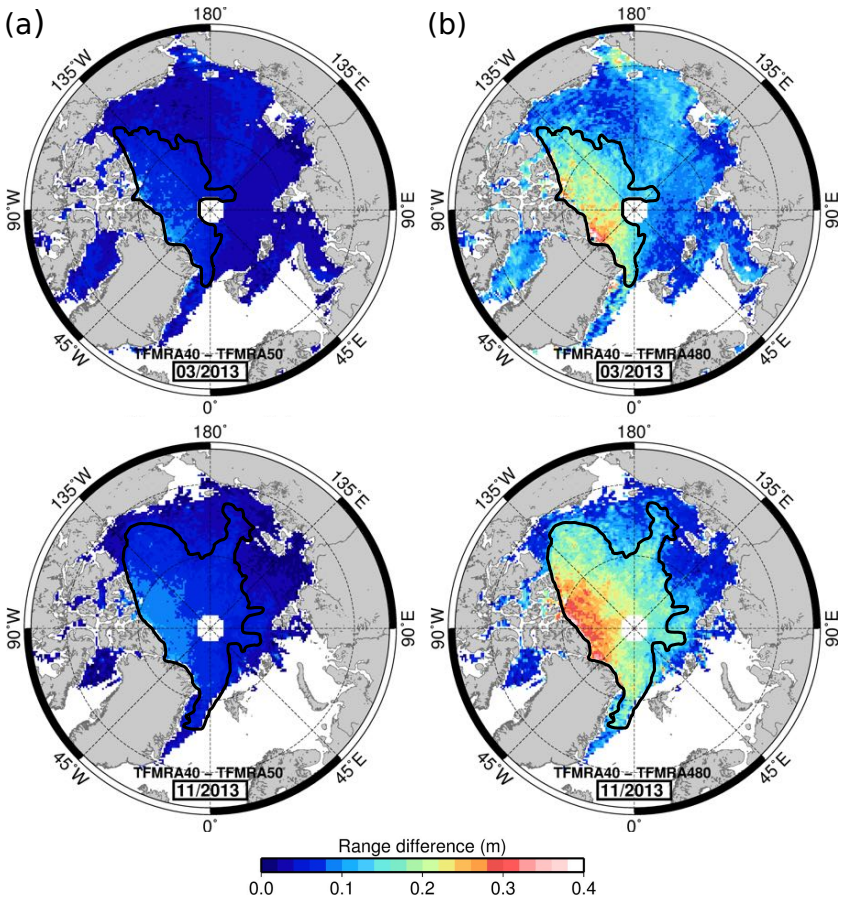

Figure 3.11. Range differences between different TFMRA (threshold first-maximum retracker algorithm) retracker thresholds for March (upper row) and November (lower row) 2013. **(a)** TFMRA40–TFMRA50, **(b)** TFMRA40–TFMRA80. The black polygon defines the averaged MYI zone, retrieved from the OSI SAF ice-type product.

distribution is similar to the radar freeboard retrieval and results from Eq. (3.6), without using a correction term for the signal penetration into snow. The random thickness uncertainties are increased by a factor of around 10 and also feature the same pattern as the random freeboard uncertainties in Figure 3.10.

Figure 3.13 shows contributions to the systematic sea-ice thickness uncertainty for March 2013. The bias uncertainty of each parameter (e.g. snow depth, ice and snow density) is multiplied with the corresponding partial derivative (Eq. 3.8) and hence gives the contribution to the thickness bias. Figure 3.13a shows the bias that results from the interannual snow-depth variability. Here we find values between 0.12 m (FYI) and 0.21 m (MYI) for March 2013. Figure 3.13b shows the bias resulting from the interannual snow-density variability. It is between 0.10 m (FYI) and 0.18 m (MYI). In contrast to Figure 3.13a we find an inverse pattern for the ice-type dependency. Figure 3.13c shows the thickness bias that originates from the ice-type classification which is used to construct

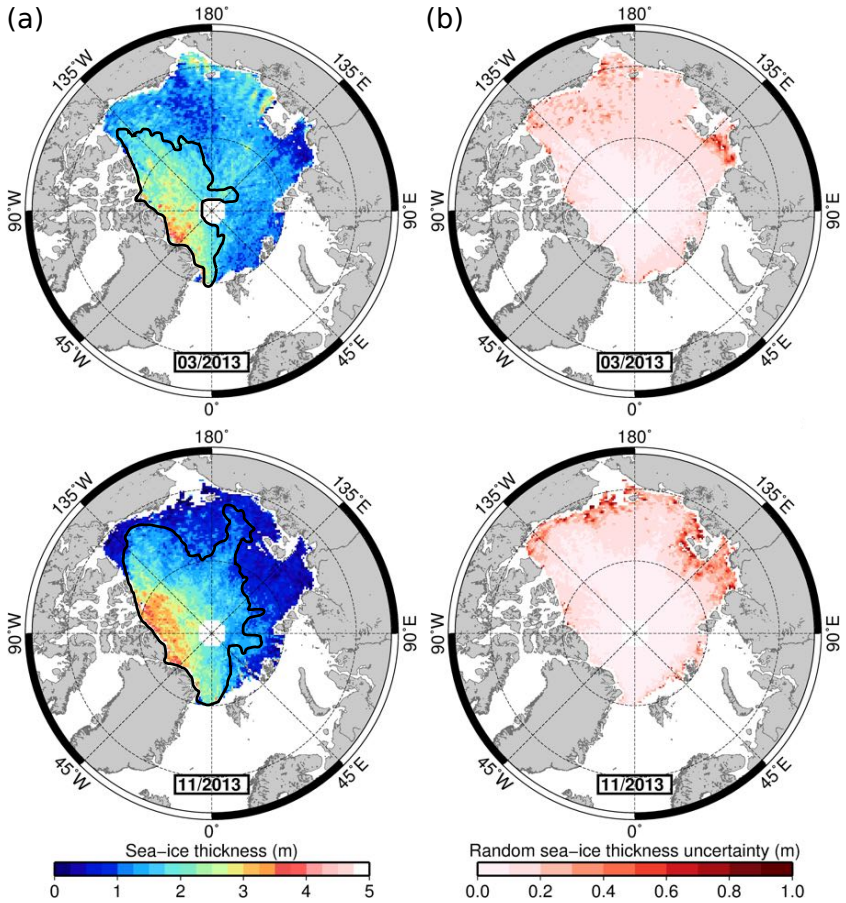

Figure 3.12. **(a)** CryoSat-2 Arctic sea-ice thickness from March and November 2013, applying the 50 % threshold. **(b)** Random thickness uncertainties corresponding to **(a)**. The black polygon defines the averaged MYI zone, retrieved from the OSI SAF ice-type product.

the snow-depth field. In contrast to Figure 3.13a and b the bias features positive and negative values with peaks at the boundary between FYI and MYI where the uncertainty of the ice-type classification is relatively high. There we find values of up to ±0.05 m for March 2013. The same pattern, just inverse, is shown by the ice-density bias, which is induced due to the ice-type classification (Figure 3.13d). Here we find values of ±0.04 m at the ice-type boundaries.

3.4 Discussion

In this section we first focus on the comparison between the retrievals from different retracker thresholds. These results are then discussed in the context of the total error budget of the CS-2 freeboard and thickness retrieval where sources of uncertainty are separated into random and systematic uncertainties.

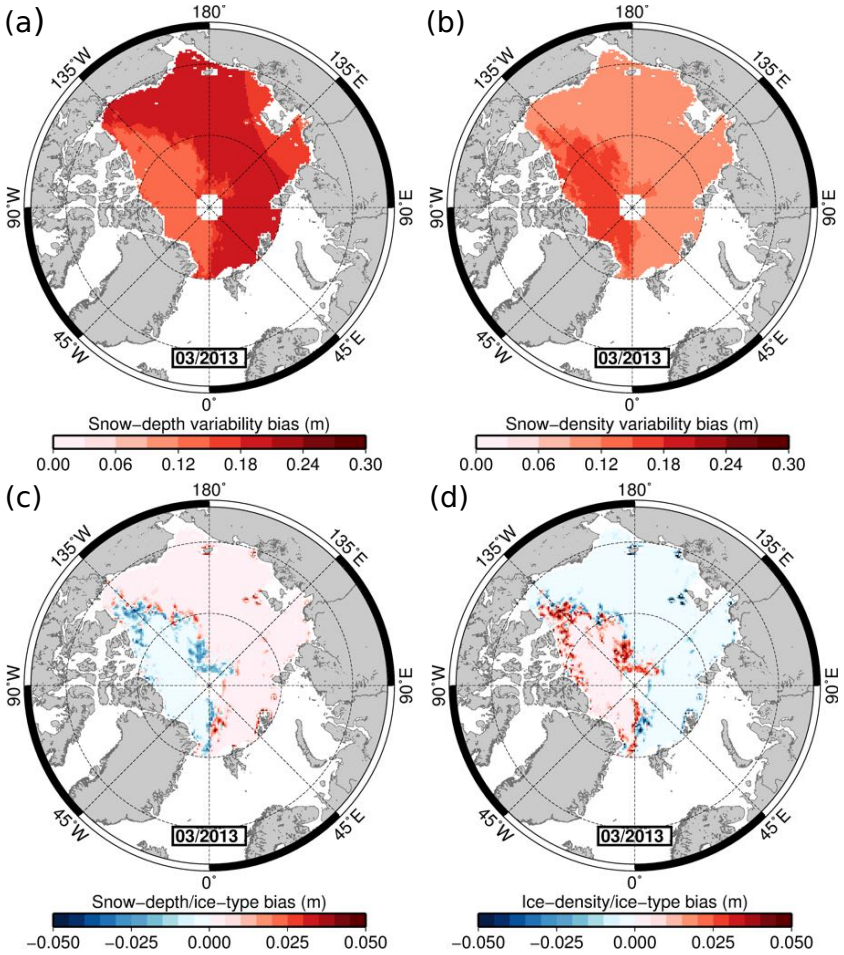

Figure 3.13. Contribution to the sea-ice thickness bias originating from **(a)** snow-depth variability, **(b)** snow-density variability and ice-type-induced uncertainties of **(c)** snow depth and **(d)** ice density.

3.4.1 Differences between the retrievals of different thresholds

The comparison of the regional distribution of the CS-2 freeboard map from April 2011 with ASCAT backscatter data shows similar geographical features. Since MYI is usually associated with higher ASCAT backscatter, both backscatter and freeboard should correlate. Local features, like a small area of potentially MYI in the East Siberian Sea, are visible (red dashed box in Figure 3.6a) in both data sets and give confidence that CS-2 is indeed able to capture the actual distribution of sea-ice types.

Considering the freeboard maps in Figure 3.9 we find negative freeboard from applying the 80 % threshold for FYI. It needs to be taken into account that the CS-2 freeboard retrievals have not been corrected for the lower wave propagation in the snow layer, which may lift up the freeboard. Therefore a correction term has to be added to F_{R}. Regarding Matzler and Wegmuller (1987), the correction can be applied by reducing the range below

the snow–ice interface by the ratio of vacuum speed of light to local speed of light in the snow layer (22 % for a snow density of 300 kg m^3). If the main scattering horizon is located in the snow layer, either due to the physical properties of the snow or due to the choice of a too-low retracker threshold, the snow propagation correction has to be applied by the fraction of penetration into the snow layer accordingly.

Considering the results of the direct comparison with airborne laser altimetry data, we estimate the mean differences between snow freeboard and the CS-2 freeboard retrievals as the distance that the radar signal propagated through the snow. Hence the mean CS-2 retrievals from the different thresholds are elevated to 0.46 m (40 %), 0.39 m (50 %) and 0.22 m (80 %). With regard to the snow freeboard from ALS, this indicates a location of the main scattering horizon of 0.16 m (40 %), 0.24 m (50 %) and 0.4 m (80 %) below the snow surface. Another airborne survey in the framework of Operation IceBridge (OIB) took place in the same area on 15 April (green dotted line in Figure 3.7a). The operating airplane carried a snow-depth radar that is able to map the snow depth along the flight track. The data reveal a mean snow depth of 0.31 m along the track (Kurtz et al., 2012, updated 2014). Furthermore from simultaneous in situ measurements on the ground we additionally know that the mean snow depth exceeded 0.3 m (Willatt and Haas, 2011). Thus if we assume this value as representative for this area, the 40 % threshold does not track the ice surface. Also the 50 % threshold seems to be too low, which is consistent with the conclusions in Kurtz et al. (2014). On the other hand the 80 % threshold seems to be too high considering the estimated snow depths. We acknowledge that the approach of Kurtz et al. (2014) is significantly different and therefore our approach of using an 80 % threshold can yield different results. We also note that this comparison might be only valid for the multiyear ice region north of Alert in spring. This implies that in the case of the 40 and 50 % threshold we need to apply a geometric correction before converting freeboard to thickness (Eq. 3.6). This has been done for the AWI CS-2 sea-ice product where a 40 % threshold was used. Nevertheless the spatial and temporal variation of such a geometric correction term is unknown.

The narrow probability density function of the 80 % threshold indicates less variation in the upper part of the leading edge. We can speculate that the shallow probability density function for the 40 and 50 % thresholds (Figure 3.8) originate from volume scattering through the snow layer which affects the lower part of the leading edge and leads to increased scattering in the range retrieval.

Considering the spatial differences between the retracker thresholds after gridding indicates a flattened leading edge over MYI and a steep leading edge over FYI. A flat leading edge results in increased range deviations between the retracker thresholds, as can be seen in Figure 3.11. This information could be used in the future to obtain an ice-type classification directly from the CS-2 data, similar to the approach of Zygmuntowska et al.

(2013). The gradient inside the MYI area in Figure 3.11b seems to correlate with the gradient of the radar freeboard retrieval (Figure 3.9) and indicates that with increasing radar freeboard the leading edge is flattened, which causes increasing deviations between the retrievals of the different retracker thresholds.

3.4.2 Major increase of multiyear ice freeboard in November 2013

In November 2013 we observe a major increase of radar freeboard in the MYI region north of Greenland and Canada compared to previous November data and even March 2013 (Hendricks et al., 2013). This applies to all thresholds, though for the 80 % threshold this increase is less strong and only significantly appears north of Greenland and Canada. This can be considered as unlikely since March represents the end of the winter season and November a period shortly after the beginning of the freeze-up. We can speculate that this is an effect of a higher-than-usual snow load in combination with a limited penetration of the radar pulse into the snow due to non-negligible volume scattering caused by ice lenses and possibly wet snow in the beginning of the freezing season. This further implies that using retracker with 50 % and also a 80 % threshold does not track the ice surface in these conditions, which was assumed by Laxon et al. (2013) and Kurtz et al. (2014). This agrees with results of recent work by Willatt et al. (2010) and Willatt et al. (2011). They show that the CS-2 range estimates may only partially penetrate into the snow layer; thus a penetration correction would be required. Their findings are based on controlled ground-based K_{u} band radar experiments and aircraft validation data such as from the CryoSat-2 Validation Experiment (see also Sect. 3.2.5). Nevertheless the comparison with airborne laser altimetry and the differences between the threshold retrievals give rise to the assumption that the impact of volume scattering and/or surface roughness is reduced using a threshold close to the peak.

Thus we can speculate how to accommodate the spatial and temporal variability of radar penetration in regions or periods where snow conditions can not be considered as cold and dry without significant internal density contrast by ice lenses. In these scenarios where the main scattering horizon is not penetrating the snow load completely, the usage of a low-threshold retracker might be reasonable to track the snow freeboard. On the other hand, in the case of regions where penetration is physically possible, a high-threshold retracker might be the better choice. It would include volume scattering and thus track the ice freeboard. Such a parametrization is hypothetical at the moment and may result in significant biases if the choice of threshold is not correctly timed with the actual snow conditions.

3.4.3 The retracking uncertainty in the context of the total uncertainty budget

The random uncertainties of the radar freeboard are caused by the signal noise and the sea-surface height uncertainty. They can be reduced by averaging inside a 25 km × 25 km grid cell and decrease with $\sqrt{N}$, where N is the number of measurements to be averaged. Since the CS-2 track density within on month increases with higher latitude towards the North Pole, this results in a latitude-dependent gradient.

The systematic radar freeboard uncertainties originate from the choice of the retracker threshold and both the physical penetration of the radar pulse and the surface roughness. Since these uncertainties cannot be separated with sufficient accuracy, they are treated as a combined contribution. We try to estimate this uncertainty by evaluating the differences between the retrievals of the different thresholds. Between the 40 and the 80 % threshold we find deviations of up to 0.35 m for MYI, whereas for FYI they remain below 0.1 m. This uncertainty can potentially be reduced with the findings from the direct comparisons with laser altimetry where we relate the threshold retrievals to the snow freeboard and estimated snow depths. Considering the mean difference between the 50 and 80 % retrievals, we can roughly estimate an uncertainty of 0.06 m (0.12 m) for FYI (MYI). Since this uncertainty has a systematic nature, it can not be reduced with averaging. Therefore it will dominate the total radar freeboard uncertainty since the random uncertainty contribution is below 0.03 m, neglecting the marginal ice zones.

Considering the sea-ice thickness retrieval, one has to separate again between random and systematic uncertainties. The random uncertainties are composed of the random freeboard uncertainty and the variability of ice density. The composited random thickness uncertainty shows the same pattern and features as the corresponding random freeboard uncertainty and basically is increased by a factor of 10, which is caused by the freeboard-to-thickness conversion.

Due to the usage of auxiliary products (e.g. snow depth, snow and ice densities, ice type) the sea-ice thickness product is affected by several systematic uncertainties. Their impact depends on the one hand on their individual uncertainty and on the partial derivative (Eq. 3.8) on the other hand. Among the auxiliary data products the snow-depth uncertainty that arises from interannual variabilities dominates. With regard to Figure 3.13a the inverse pattern for the snow-depth variability results from multiplication with the partial derivative. The polarity of Figure 3.13c and d is caused by the nature of the ice-type product. Since a measuring point can be flagged as either FYI or MYI, the induced error can only point in one direction. Since the classification uncertainty that we retrieve from the confidence level is most significant at the boundary between FYI and MYI, we also find the peak values in those regions. The ice-type-induced

ice-density uncertainty shows the same features, but with an inverse polarity. To combine these uncertainties it is necessary to introduce covariances, which is beyond the scope of this study. Therefore we only consider the individual contributions of the systematic uncertainties. However, the systematic uncertainties of the auxiliary variables can possibly not be reduced as long as they are used (e.g. W99 climatology, OSI SAF ice-type product). Additionally we have to consider the bias caused by the choice of the retracker threshold in conjunction with the unknown penetration of the radar pulse and the surface roughness. Due to the freeboard-to-thickness conversion it is increased by a factor of approximately 10. This results in systematic uncertainties of 0.6 m (1.2 m) for FYI (MYI). Like for the freeboard retrieval this bias will dominate the total uncertainty.

However we do acknowledge that the assumption of uncorrelated random uncertainties and thus the reduction by averaging might be an insufficient description of certain factors. For example the uncertainty of sea-surface anomaly can only be reduced by gridding if enough lead detections exist. If none are available within one grid cell, the uncertainty contribution due to the lack of leads would be constant for all CS-2 data points and not reduced by gridding. Also temporal variations within 1 month are not included in these considerations, which might be significant during freeze-up and summer melt and result in visible orbit patterns in the monthly means. The temporal and spatial covariances between uncertainty contributions of freeboard and thickness retrievals are only weakly constrained by observations, mainly in Arctic spring, and thus we have limited our uncertainty estimation to a first-order level where we assume correlation (systematic uncertainties) or no correlation (random uncertainties).

3.5 Conclusions

In this study we calculate CryoSat-2 radar freeboard retrievals with consistent uncertainty estimates in spring/autumn 2013, applying three different thresholds for a threshold first-maximum retracker algorithm. The choice of the thresholds is based on current approaches by different scientific groups for CryoSat-2 data processing on Arctic sea ice. In general the application of all thresholds gives confidence that the freeboard retrieval represents the geographyical distribution of sea-ice types. This is shown by direct comparisons with airborne laser altimetry on the local scale as well as with ASCAT backscatter data at basin scale.

Considering first-year ice (multiyear ice) in March 2013 we find mean radar freeboard values of 0.121 m (0.265 m) for the 40 % threshold, 0.086 m (0.203 m) for the 50 % threshold and 0.024 m (0.092 m) for the 80 % threshold. The comparison between the freeboard retrievals from different thresholds and airborne laser altimetry indicates that the 40 and

50 % thresholds are tracking above ice surface, while the 80 % threshold tracks below the ice surface. However, the freeboard maps show that the choice of retracker thresholds does have a significant impact on magnitudes of sea-ice freeboard and thickness estimates, but that the spatial distributions of these parameters are less affected. Analysing the differences between the freeboard retrievals of different thresholds, we find that the leading edge for MYI is less steep compared to the leading edge of FYI. With extraction of this information directly from the CryoSat-2 data the usage of an auxiliary ice-type product would be redundant and could therefore reduce the uncertainties.

Our uncertainty estimates of the gridded data show values up to 0.03 m for random freeboard uncertainties, neglecting the marginal ice zones. The main driver of their geographical pattern is the density of CryoSat-2 ground tracks, which causes a latitude-dependent gradient. In addition systematic uncertainties of roughly 0.06 m (0.12 m) for FYI (MYI) arise from the choice of the retracker and the unknown penetration of the radar pulse into the snow layer. Considering the freeboard-to-thickness conversion we have estimated the resulting uncertainties for the thickness product and find a similar distribution for the random thickness uncertainties, multiplied by a factor of 10. Due to the usage of auxiliary products (e.g. snow depth, ice and snow densities and ice type) systematic uncertainties in the range between 0.01 and 0.2 m from each of this variables have to be taken into account. However, the estimated systematic uncertainty of roughly 0.6 m (1.2 m) for FYI (MYI) due the choice of the retracker and the unknown penetration of the radar pulse into the snow layer clearly dominates the current thickness uncertainty budget.

Depending on the threshold, the comparison between March and November 2013 retrievals shows an increase of 0.02–0.15 m of radar freeboard in the MYI region north of Greenland and Canada from March to November, which is unlikely. It gives rise to the assumption that even by applying an 80 % threshold retracker the radar does not penetrate through the snow layer completely. Therefore we can anticipate a seasonal bias in the CryoSat-2 freeboard retrieval and higher-level products.

Thus, for the future it would be useful to investigate different thresholds depending on the properties of the snow load, e.g. seasonal or location specific retrackers. To support this there is a strong need for more information and measurements on the spatial and temporal variability of snow properties.

3.6 Acknowledgements

The validation measurements in the framework of CryoVEx and PAMARCMIP 2011 campaigns were carried out by the DTU Space and the Alfred Wegener Institute, Helmholtz

Centre for Polar and Marine Research, Bremerhaven, Germany. The CryoVEx campaigns are part of ESA's Living Planet Programme. The CryoSat-2 data are provided by the European Space Agency. The work of S. Hendricks and V. Helm was funded by the Federal Ministry of Economics and Technology (Grant 50EE1008). All of this is gratefully acknowledged.

Chapter 4

Impact of snow accumulation on CryoSat-2 range retrievals over Arctic sea ice: an observational approach with buoy data

Published in *Geophysical Research Letters*, 42, 4447–4455. doi: 10.1002/2015GL064081

R.Ricker[1], S. Hendricks[1], D. K. Perovich[2], V. Helm[1], and R. Gerdes[1]

[1]Alfred Wegener Institute, Helmholtz Centre for Polar and Marine Research, Bremerhaven, Germany
[2]US Army Cold Regions Research and Engineering Laboratory, Hanover, USA

Abstract

Radar altimetry measurements of the current satellite mission CryoSat-2 show an increase of Arctic sea-ice thickness in autumn 2013, compared to previous years but also related to March 2013. Such an increase over the melting season seems unlikely and needs to be investigated. Recent studies show that the influence of the snow cover is not negligible and can highly affect the CryoSat-2 range measurements if it is assumed that the main scattering horizon is given by the snow-ice interface. Our analysis of Arctic ice mass-balance buoy records and coincident CryoSat-2 data between 2012 and 2014 adds observational evidence to these findings. Linear trends of snow and ice freeboard measurements from buoys and nearby CryoSat-2 freeboard retrievals are calculated during accumulation events. We find a positive correlation between buoy snow-freeboard and CryoSat-2 freeboard estimates, revealing that early snow accumulation might have caused a bias in CryoSat-2 sea-ice thickness in autumn 2013.

4.1 Introduction

A rapid reduction of the Arctic sea-ice cover has been observed during the last decades (Comiso et al., 2008; Comiso, 2012; Comiso and Hall, 2014; Stroeve et al., 2012). There is significant evidence that along with the shrinking ice area, sea ice is also thinning. This has been directly observed with upward looking sonar measurements from submarines, aircraft and autonomous stations (Rothrock et al., 1999; Lindsay and Schweiger, 2015; Meier et al., 2014). The only technique however to monitor sea-ice thickness on basin scale are space borne satellite altimeter measurements (Kwok et al., 2009; Laxon et al., 2013). The current satellite altimeter mission CryoSat-2 (CS-2) was launched in 2010 and is equipped with a K_u-band synthetic aperture interferometric radar altimeter (SIRAL). CS-2 measures the ice surface and open water elevations. Subtracted, both quantities yield ice freeboard, the height of the ice above the local sea level. In contrast to a laser altimeter, such as onboard the ice, cloud and land elevation satellite (ICESat), the radar can penetrate the snow cover. The range estimate, and thus the freeboard sensed by the radar altimeter, depends on the actual location of the main scattering horizon (Ricker et al., 2014a) as well as surface roughness within the CS-2 footprint (Hendricks et al., 2010). In previous studies it has been assumed that the main scattering horizon is given by the snow-ice interface (Laxon et al., 2013; Kurtz et al., 2014), though both authors did not rule out an influence of radar backscatter from the snow layer. For K_u-band frequencies (13.5 GHz), this assumption might only be valid for a cold, dry and homogenous snow layer. On the other hand, density contrasts such as compacted snow and/or ice lenses in the snow layer may significantly alter the backscatter or absorption properties for K_u-band signals (Beaven et al., 1995). Kwok (2014) analysed airborne snow and K_u-band radar data from Operation IceBridge and found that the air-snow interface clearly contributes to radar backscatter, causing an alteration of the tracking point. The limited CS-2 range resolution of 0.47 m does not allow to distinguish between the radar return of the snow-ice interface and the air-snow interface. Moreover, backscatter from both interfaces superimpose each other and cause broadened radar returns, which is largest for snow depths >20 cm (Kwok, 2014). As a result, freeboard estimates can be biased high with the presence of thick snow layers. In addition, the effect of multiple backscatter interfaces on the radar waveform is superimposed by the effect of surface roughness in the CS-2 footprint. First retrieval methods obtain freeboard and roughness from CS-2 waveforms (Kurtz et al., 2014), however the scale of snow contribution to the freeboard bias for different regions, ice types and season is currently unclear. We therefore use the term radar freeboard, which is associated with CS-2 freeboard in this paper. It implies that surface roughness affects the range retrieval and that snow plays a role for the the location of the main backscatter interface below the top snow surface. For wet snow at the beginning and the end of the melting season, the dielectric properties of the

snow layer might even limit the physical penetration of radar waves. It is our goal to estimate the uncertainties originating from additional snow backscatter and distinguish their effects from simplification or differences in waveform interpretations from available algorithms.

During the freeze-up in November 2013 we observed increased multiyear ice freeboards compared to March 2013 of the CS-2 monthly gridded sea ice data product of the Alfred Wegener Institute (Ricker et al., 2014a). An increase of freeboard over the melting season is not very likely and has to be investigated. However, few to none aircraft observations are available during this period. Ice mass-balance buoys (IMBs), however are deployed regularly in the Arctic and provide year-round measurements of sea-ice thickness and snow depth. Their acoustic sounder measurements allow to monitor changes at the ice/snow surface and the ice bottom independently (Richter-Menge et al., 2006). Observational data from these buoys offer point measurements of ice thickness changes due to thermodynamic growth and the accumulation of snow. Furthermore, these data can be used to cross-validate satellite data (Nghiem et al., 2007), although the comparison of spatial coarse satellite measurements with point measurements from IMBs can be problematic (Kwok et al., 2007).

The importance of snow accumulation on freeboard retrieval during freeze-up was investigated for the ICESat mission. Its laser altimeter is reflected at the top snow surface and thus the range measurements are a direct function of snow accumulation. Therefore we use the term snow freeboard as the height of the snow surface above the water level. Kwok et al. (2007) compared ICESat snow-freeboard measurements with values derived from IMB records in the Arctic and concluded that snow depth changes account for 90 % of multi-year snow freeboard rise between autumn and late winter. Thus, any contribution of snow backscatter would cause a noticeable and temporal variable freeboard bias that is multiplied tenfold by the conversion into thickness.

In our study, we therefore compare IMB-derived sea-ice thickness and snow depth with coincident CS-2 measurements between 2012 and 2014. This is done to investigate the observed increase of CS-2 multi-year sea-ice freeboard north of Greenland and Canada over the melting season. We use the IMB data to investigate the changes of snow depth and CS-2 radar freeboard, avoiding the comparison between absolute values. We hypothesize that the snow cover significantly affects the CS-2 freeboard retrieval by snow backscatter which would affect also sea-ice thickness and volume, independently of the range retrieval method.

4.2 Methods

4.2.1 Ice and snow freeboard from ice mass balance buoys

IMBs are usually deployed on undeformed sea ice floes of average size and thickness, avoiding deformed ice and melt ponds. The IMBs consist of a main buoy which carries the transmission and data acquisition system and batteries. Among other sensors acoustic rangefinder sounders above the snow surface and below the ice bottom record changes in snow depth and bottom growth or ablation respectively. The accuracy of these rangefinder sounders is 5 mm (Richter-Menge et al., 2006).

We use provisional IMB data provided by Perovich et al. (2013) that are available on the website http://imb.erdc.dren.mil/buoysum.htm. They contain meteorological data and the positions of the snow surface, ice surface and ice bottom. The range measurements are referenced to the initial ice surface. Hence, in the absence of ice surface melt the value of the ice bottom position is identically to the ice thickness. All consistent IMB datasets that were available in the period 2012-2014 are used in this study, in particular the records of 7 IMBs (Table 4.1). Figure 4.1 shows the IMB drift tracks within the considered period. The dataset of IMB 2012G has been divided into two periods (A and B) since it covers two freezing seasons. We excluded data during summer season since CS-2 freeboard retrievals are not available for this period. Furthermore, periods where the rangefinder sensors became unreliable were excluded, except of IMB 2012G where the bottom sounder is unreliable from 7 September 2013 until 23 December 2013. We used a constant ice bottom position over the missing data period by using the last observed ice thickness of 2.16 m from 7 September 2013 on. For an ice thickness of > 2 m and snow depth > 0.4 m the thermodynamic ice growth is < 0.1 m and therefore negligible (Semtner Jr, 1976; Leppäranta, 1993).

The IMBs measure meteorological parameters hourly (position, barometric pressure, air temperature) whereas others are sampled every 4 hours (surface and bottom positions, temperature profiles). We resampled the IMB time series to a temporal resolution of 2 days, because with this period a sufficient CS-2 orbit coverage is given within a search radius of 50 km around an IMB position (Figure 4.2a). Since the IMB only measures ice thickness (T) and snow depth (S) we have to convert them into ice (F_I) and snow freeboard (F_S), assuming hydrostatic equilibrium:

$$F_\mathrm{I} = T \cdot \frac{\rho_\mathrm{W} - \rho_\mathrm{I}}{\rho_W} - S \cdot \frac{\rho_\mathrm{S}}{\rho_\mathrm{W}}, \tag{4.1}$$

$$F_\mathrm{S} = F_\mathrm{I} + S, \tag{4.2}$$

where densities of 320 (Warren et al., 1999) and 1024 kg/m^3 are assumed for snow (ρ_S) and sea water (ρ_W). Since all considered IMBs were deployed at the end of the melting season or beginning of freeze up (see Table 4.1), we assume that the ice survived the summer melt and therefore use a multiyear ice density of 882.0 kg/m^3 (Alexandrov et al., 2010). We acknowledge that values for snow and multiyear ice densities vary in literature but since we consider relative changes, this effect should not be remarkable. We are also aware that the IMB spot measurements might not represent local hydrostatic equilibrium. We however assume that the observed snow accumulation is representative for nearby level ice.

Table 4.1. Linear trends α (cm/month) of buoy snow freeboard (F_S), buoy ice freeboard (F_I) and CryoSat-2 modal freeboard (F_C)[a].

Buoy	Event period $[t_0, t_1]$	α_{F_S}	α_{F_I}	$\alpha_{F_{C40}}$	$\alpha_{F_{C50}}$	$\alpha_{F_{C80}}$
2012G-A	1 Oct 2012 - 30 Nov 2012	6.9±0.6	-2.8±0.3	1.8±1.2	1.9 ±1.2	1.6±1.0
2012H	28 Sep 2012 - 29 Dec 2013	5.2±0.4	-0.8±0.1	4.8±0.8	4.1±0.7	3.3±0.5
2012J	16 Oct 2012 - 13 Dec 2013	5.3±0.7	-1.2±0.4	4.9±2.1	4.2±1.7	3.2 ±0.9
2012L	4 Apr 2012 - 18 May 2012	8.4±0.6	-2.9±0.3	12.9[b]±3.4	9.3[b]±2.3	5.2[b]±1.5
2012G-B	14 Sep 2013 - 9 Dec 2014	11.4±1.0	-5.2±0.4	8.3±1.2	10.0±2.0	6.5±1.0
2013F	20 Sep 2013 - 1 Nov 2013	23.1±1.1	-11.1±0.6	12.5±2.7	9.2±1.9	4.8±1.2
2013H	–	–	–	–	–	–

[a] For F_C different retracker thresholds have been applied: F_{C40} (40 %), F_{C50} (50 %) and F_{C80} (80 %). The linear trends are calculated only during defined event periods (see Figure 4.3).

[b] No correction for lower wave propagation in the snow.

4.2.2 CryoSat-2 modal freeboard retrieval

CS-2 radar freeboard is obtained from ESA geolocated waveform data (Level-1B) and processed as described in Ricker et al. (2014a). We use the Threshold-First-Maximum retracker (Helm et al., 2014) with three different thresholds of 40 %, 50 % and 80 % (Ricker et al., 2014a) of the first-maximum peak power. This is done to investigate the influence of snow backscatter at different parts of the leading edge. We apply a range correction $h_c = h_a(1 - c_s/c_v)$ for a lower wave propagation speed inside the snow layer, where h_a is the apparent penetration, which is the covered distance in the snow when we assume vacuum speed of light (c_v) as propagation speed. It is estimated by the distance between the IMB snow freeboard and the respective CS-2 freeboard retrieval. The ratio of local speed of light in the snow layer (c_s) to c_v is approximately 0.78, assuming a snow density of 320 kg/m^3 (Matzler and Wegmuller, 1987; Tiuri et al., 1984).

For the comparison with the IMB measurements, we apply a search radius of 50 km around each resampled IMB position within the given time window of two days. All individual CS-2 measurements within the search area are collected for further processing (Figure 4.2a).

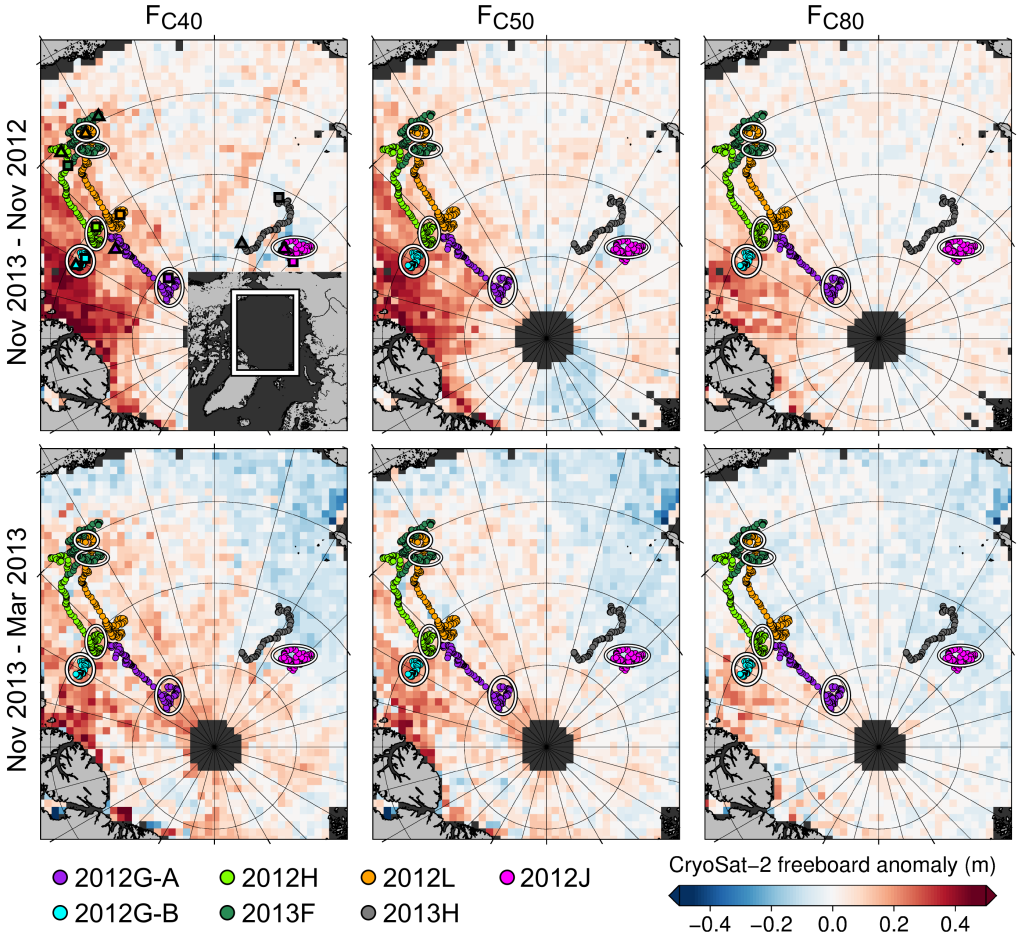

Figure 4.1. The maps show the differences in gridded CryoSat-2 Arctic modal freeboard (F_C) between November 2013 and November 2012 retrievals (top row) and between November 2013 and March 2013 retrievals (bottom row). For F_C different retracker thresholds have been applied: F_{C40} (40 %), F_{C50} (50 %) and F_{C80} (80 %). In addition, buoy tracks are mapped with encircled segments that represent the event periods where significant snow-accumulation occurs (see Figure 4.3). Squares (triangles) in the upper left panel highlight the start (end) of a considered buoy drift.

IMB measurement points are discarded if the number of matched CS-2 measurements is less than 50. The average number of matches is 206 for this analysis.

Since IMBs are usually deployed on level ice, we do not use the average of all collected CS-2 points. Instead we compute the probability density functions of CS-2 freeboard values with a bin size of 10 cm and select the modal value. To enhance the resolution and reduce noise we compute a non-linear least squares fit of a log-normal distribution of the CS-2 freeboard distribution:

$$f(x) = \frac{c}{\sigma(x-\vartheta)\sqrt{2\pi}} \cdot \exp\left(\frac{-(\ln(x-\vartheta)-\mu)^2}{2\sigma^2}\right). \tag{4.3}$$

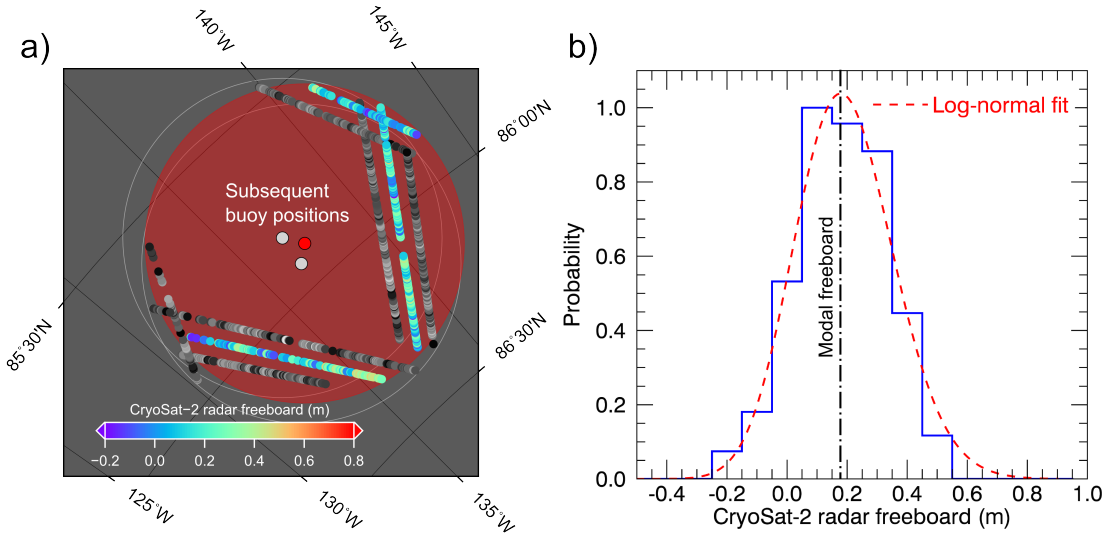

Figure 4.2. (a) Example of matched CryoSat-2 measurements within a 50 km radius (red circle) around a considered buoy position (red dot). Nearby grey dots show the buoy position 2 days before and after the current position, together with the corresponding CryoSat-2 measurements (grey-shaded). (b) Probability density function (blue solid line) of matched CryoSat-2 freeboard measurements for the considered buoy position in (a). The modal freeboard is retrieved by locating the maximum of the log-normal fit.

Fit parameters are given by the logarithmical scale parameter (μ), the shape parameter (σ), the location parameter (ϑ) and a scale parameter for the log-normal distribution (c). x represents the thickness or bin value. The log-normal distribution describes typical sea-ice thickness distributions (Haas, 2009). Figure 4.2b shows an example of a CS-2 freeboard distribution and the corresponding fit within the search radius of a resampled IMB measuring point. We take the maximum of the log-normal fit to obtain the CS-2 modal freeboard at higher resolution than the binned values for comparison with the resampled IMB measurement.

4.3 Results

Figure 4.3 shows the direct comparison between the CS-2 modal freeboard retrievals and IMB snow and ice freeboard. We find high scattering of CS-2 modal freeboard, independent of the used retracker threshold. The sites where the IMBs were deployed show a high variability in ice thickness and snow depth. The observed mean thickness varies between values greater than 3 m (2012L) and less than 1 m (2012J). The thicker ice floes show no substantial growth during most parts of the freezing season (2012L), while snow accumulates mainly at the beginning of the freezing season between September and December. In order to find a correlation between snow depth and CS-2 freeboard, we

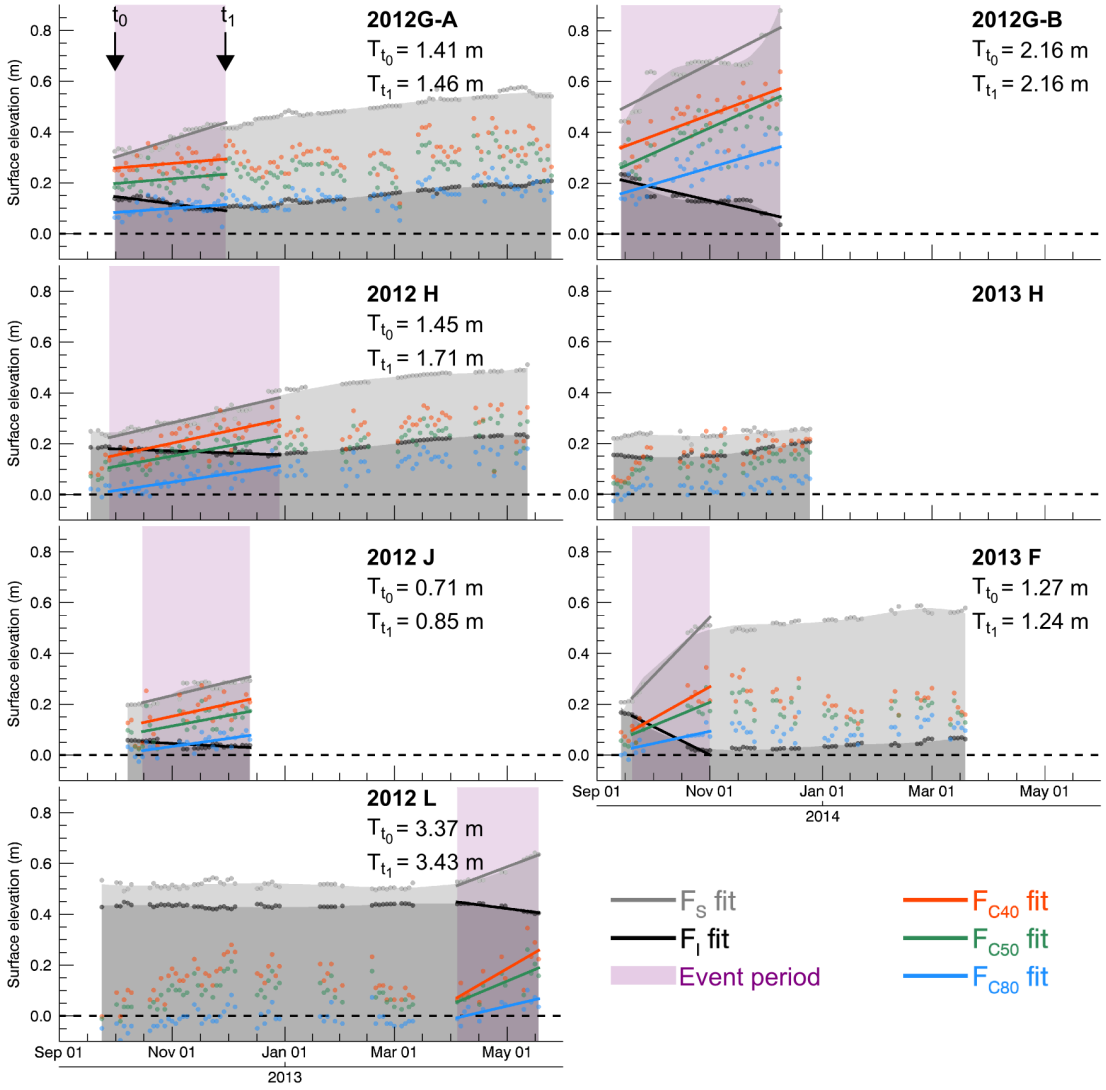

Figure 4.3. Time-series of buoy snow freeboard (F_S), buoy ice freeboard (F_I) and CryoSat-2 modal freeboard (F_C). For F_C different retracker thresholds have been applied: F_{C40} (40 %), F_{C50} (50 %) and F_{C80} (80 %). The solid lines represent the linear regression of freeboard from the individual measurements (dots). The purple boxes represent event periods, starting at t_0 and ending at t_1. During this periods significant snow-accumulation occurred and is considered for the linear regression (Table 4.1). T_{t_0} and T_{t_1} are the measured IMB ice-thicknesses at t_0 and t_1.

focus on periods with substantial changes in snow depth that are marked in Figure 4.3 as event periods. We additionally restrict this periods by taking into account the left pulse peakiness (PP_L) that has been described in Ricker et al. (2014a) and which is a measure of the width of the leading edge of the CS-2 waveforms. High values indicate a steep leading edge and a specular return while low values indicate a shallow leading edge. Specular returns typically originate from open or refrozen leads, or from melt ponds. As for the CS-2 freeboard (see Section 4.2.2), we consider the modal PP_L. For example,

along with IMB 2012J we find high modal PP_{L} values in September and October which gives evidence that open or refrozen melt ponds still dominate the ice surface and bias the CS-2 freeboard retrieval, since we consider waveforms that originate from sea ice only. We therefore exclude all periods from our analysis where the PP_{L} value exceeds 10.

We apply a linear regression model of the form f(t)=c + α t for measurements during the event periods (Figure 4.3) to find correlations between the individual datasets. The obtained linear trends α with 1-sigma uncertainties are presented in Table 4.1. IMB 2013H has been excluded because no significant change of the snow depth has been observed. For IMB 2012L the correction for lower wave propagation in snow has not been applied, since the CS-2 retrievals are consequently below the IMB ice freeboard and the approach according to Section 4.2.2 is not reasonable. However, the impact of this correction on the trend is $<$ 1 cm/month. We find only negative trends for the IMB ice freeboard while IMB snow freeboard is always positive. The negative correlation between IMB snow and ice freeboard occurs due to the fact that an increasing snow load adds weight on the ice floe. On the other hand, we only find positive trends for the CS-2 modal freeboard. For example, along with IMB 2012G-B, we find rates of 8.3, 10.0 and 6.5 cm/month for the CS-2 modal freeboard retrievals by using 40 %, 50 %, and 80 % retracker thresholds. For the same period we find a rate of 11.4 cm/month for the IMB snow freeboard and -5.2 cm/month for the IMB ice freeboard. This noticeable increase of the snow freeboard between September and December 2013 in conjunction with the the simultaneous rise of the CS-2 modal freeboard is also shown in Figure 4.3.

The IMB drift tracks are mostly situated in regions where a positive CS-2 freeboard trend has been observed between March and November 2013 as well as between November 2012 and November 2013. The changes of CS-2 radar freeboard over the melting season in 2013 and between November 2012 and 2013 are shown as gridded freeboard difference maps for all retracker thresholds in Figure 4.1. The gridded differences are also based on modal freeboard, calculated in 5 cm bins, to be in line with the usage of modal freeboard in this study. We find high differences of up to 45 cm (30 cm) for the 40 % threshold retrieval and up to 30 cm (20 cm) for the 80 % threshold retrieval from the comparison between November 2013 and 2012 (November 2013 and March 2013) north of Canada.

4.4 Discussion

In all cases of snow accumulation during the event periods shown in Figure 4.3, the change of CS-2 radar freeboard was positive, while local observations at the IMB sites indicated

decreasing ice freeboard in all cases (see also Figure S1). The result is uniform for the three different retracker thresholds used in this study, which indicates a shift of the entire leading edge of the waveform. The comparison of absolute freeboard values reveals that the CS-2 retrieval using the highest threshold is closer to the IMB ice freeboard in typical cases, but there is no information of the statistical relevance of the IMB point data within its vicinity. In Figure 4.3 we find CS-2 freeboard retrievals located consequently below the ice freeboard of IMB 2012L for the entire considered period. This can have two reasons. Either the buoy is not in hydrostatic equilibrium or the MYI ice floe drifted in a regime of thinner FYI (see Figure 4.1). However, the comparison between the absolute CS-2 and IMB freeboard retrievals can be problematic (Kwok et al., 2007) and is not pursued in this study.

Nevertheless we expect that IMB-detected snowfall is representative for an area of 50 km around the buoy position, given that it is situated in the pack ice. In this case the findings indicate an increasing freeboard bias with snow accumulation and thus a higher bias for thick snow regimes, for example multi-year ice zones. The prominent example for these regions is the IMB 2012G. Its observation period spans two freezing seasons and in the second year it remained in a confined area in the MYI region north of Canada (see Figure 4.1). During this time we also observe a substantial increase of CS-2 radar freeboard in the gridded product in November 2013, relative to November 2012, but also relative to March 2013 (see Figure 4.1). At the same time IMB 2012G shows thicker snow (> 50 cm) in autumn 2013 than for 2012 (≈ 30 cm). Whether the increase of CS-2 radar freeboard is an indication of earlier or heavier snowfall in 2013 or result of changing surface topography is unfortunately not known. In any case the radar freeboard in both years shows a correlation with the snow depth.

The observed average increase in CS-2 radar freeboard from March to November 2013 of about 18 cm north of Canada would imply a gain of at least 0.5 m in ice thickness if we assume typical values for MYI thickness (2 m) and snow depth (35 cm) in March and absence of snow cover in November as least extreme case. With the presence of snow also in November, the implied thickness gain would further increase if hydrostatic equilibrium is assumed. Thus, even a lower snow load in November cannot explain this substantial freeboard increase. Also thermodynamic ice growth can be excluded, considering the absorbed and transmitted energy fluxes in Arctic summer (Arndt and Nicolaus, 2014).

Quick-look snow depth data, retrieved by Operation IceBridge (OIB) campaigns are provided by Kurtz et al. (2012, updated 2014.) and show an increase of up to 20 cm between the freezing seasons 2012/2013 and 2013/2014 in spring north of Canada and in the Beaufort/Chukchi Sea (Figure S2). In contrast, other areas reveal a slight decrease. Willatt et al. (2010, 2011); Kurtz et al. (2014); Kwok (2014) and Ricker et al. (2014a)

showed that the influence of snow depth on the K_u-band is not negligible. Specifically, the simulations of Kwok (2014) reveal that the snow-induced freeboard bias depends on the strength of snow surface backscatter and on the snow depth. The indication of an exceptional high snow depth in the freezing season 2013/2014 north of Canada by OIB strengthens the findings of our analysis. Our study therefore adds observational evidence to the findings of Kwok (2014). Nevertheless, we also acknowledge that the OIB data are only provisional.

It is still difficult to quantify the snow-scatter induced bias without knowledge of the regional distribution and temporal evolution of snow depth and snow stratigraphy. Snow, accumulated early, may undergo a partial melting and subsequent freezing as well as wind compaction. This leads to a very heterogeneous snow density distribution, while for the propagation of the K_u-band signal it is widely assumed that the snow density is homogeneous. In this way formed layers may affect the location of the main reflecting horizon. With snow accumulation starting already in September, when the CS-2 freeboard retrieval is still influenced by freezing or frozen melt ponds as indicated by the PP_L, we are not able to observe the beginning of this process. Likewise, wet snow or the start of snow melt in May defines the limit of retrievable CS-2 freeboard data. A model-based investigation of K_u-band radar backscatter for observed snow condition that includes internal layering and a range of metamorphic states would be helpful as a step towards the quantification of a snow bias on CS-2 data. With the differences between trends α_{F_C} and α_{F_I}, given in Table 4.1, we can estimate the freeboard-induced impact T_{bias} on the CS-2 thickness retrieval within the event periods:

$$T_{\text{bias}} = \frac{\partial T}{\partial F} \int_{t_0}^{t_1} (\alpha_{F_C} - \alpha_{F_I})\, \mathrm{d}t = \left(\frac{\rho_{\text{W}}}{\rho_{\text{W}} - \rho_{\text{I}}} \right) (\alpha_{F_C} - \alpha_{F_I})(t_1 - t_0), \tag{4.4}$$

where $\frac{\partial T}{\partial F}$ represents CS-2 sea-ice thickness (T), derived from Eq. 4.1 and differentiated with respect to freeboard (F). t_0 and t_1 mark the start and end of the event period (see Figure 4.3). Averaged over all three threshold retrievals, we obtain biases T_{bias} between 0.7 m (2012G-A) and 2.7 m (2012G-B) while the mean thickness bias is 1.4 m. Thus, our findings suggest significant thickness biases over multiyear ice with thick snow layers, if it is generally assumed that the main scattering horizon is given by the snow-ice interface during freeze-up.

The CS-2 freeboard retrievals feature random and systematic uncertainties. Speckle noise is the major contribution to the random uncertainties. For the gridded product (Figure 4.1) they are below 5 cm while for a single buoy-referenced modal freeboard retrieval (Figure 4.3) the uncertainty is in the range of 10 cm (1 bin respectively). Any systematic uncertainties are expected to have a correlation length higher than the respective search

area (50 km radius) and thus should not have a significant impact on the linear trends in Table 4.1. The sea-surface height uncertainty can be either random or systematic, depending on the interpolation between leads. In any case this uncertainty is represented by the scatter of the CS-2 modal freeboard values (see Figure 4.3) and in the 1-sigma uncertainties of the trends.

The random uncertainties of the IMB measurements are attributed to their accuracy of 5 mm and hence are negligible in this comparison. Potential biases can occur due to the thickness to freeboard conversion where we use constant values for ice and snow densities. However, relative changes and trends should not be affected remarkably. Another origin of uncertainty is snow drift that occurs on site and counteracts the larger scale correlation of the IMB snow depth measurements. This impact should be reduced by considering measurements of 7 independently operating IMBs.

4.5 Conclusion

We hypothesized that the CryoSat-2 freeboard retrieval is affected by snow accumulation, causing a bias that has contributed to the major increase of CryoSat-2 multiyear ice freeboard north of Canada in November 2013. We compared year-round ice and snow freeboard measurements of Arctic ice-mass balance buoys (IMBs) from 2012 to 2014 with coincident CryoSat-2 measurements. We used CryoSat-2 modal freeboard retrievals by applying three different retracker thresholds to investigate the effect of snow accumulation on different parts of the leading edge.

By defining event periods of substantial snow depth changes, we calculated linear trends of the CryoSat-2 freeboard retrievals and IMB ice and snow freeboard within these periods. We only find negative trends for the IMB ice freeboard while the IMB snow freeboard trends are always positive. Simultaneously we observe only positive trends for coincident CryoSat-2 radar freeboard estimates, regardless of the used retracker threshold. North of Canada we find a mean increase of 18 cm of the gridded CryoSat-2 freeboard retrieval from March to November 2013. From September to December 2013 IMB measurements in this area reveal snow and ice freeboard growth rates of 11.4 and -5.2 cm/month, respectively. At the same time we find a mean CryoSat-2 freeboard growth rate of 8.3 cm/month, averaged over all three retracker retrievals. We do assume that this observation is the result of a snow bias on CryoSat-2 freeboard data, since thermodynamic ice growth over the summer period is not to be expected. The magnitude of this bias is larger than reported values in literature that were based on theoretical considerations (Kurtz et al., 2014; Kwok, 2014). An exceptional high snow depth and early accumulation during the freezing season 2013/2014 north of Canada, shown by IMB measurements and indicated

by Operation IceBridge snow depth retrievals, might have lead to the major increase of CryoSat-2 multiyear ice freeboard in November 2013 for this region. By quantifying the impact on CryoSat-2 sea-ice thickness retrievals we obtain a mean multiyear ice thickness bias of 1.4 m, if it is assumed that the main scattering horizon is given by the snow-ice interface.

We conclude that snowfall can have a significant impact on CryoSat-2 range measurements and therefore on ice freeboard, thickness and volume. The assumption that the CryoSat-2 main scattering horizon is given by the snow-ice interface cannot be justified in regions with a thick snow layer. Finally this study also shows that there is a strong need for more data and knowledge about the seasonal cycle of snow distribution and properties on sea ice.

4.6 Acknowledgments

Ice-mass balance buoy data are provided by the Cold Regions Research and Engineering Laboratory (CRREL). CryoSat-2 data are provided by the European Space Agency (ESA). The work of S. Hendricks and V. Helm was funded by the German Federal Ministry of Economics and Technology (Grant 50EE1008). All this is gratefully acknowledged. Thanks also to Marcel Nicolaus and Sandra Schwegmann for their input.

4.A Supporting Information

Figure 4.4 supports the statement that the CryoSat-2 freeboard shows a positive correlation with the snow freeboard derived from IMB measurements while the correlation with IMB ice freeboard is negative. Figure 4.5 shows the difference in snow depth between years 2013 and 2014 in spring. The snow depth was retrieved by measurements of a snow radar, operated during Operation IceBridge aircraft campaigns over Arctic sea ice and provided as a quick-look product by Kurtz et al. (2012, updated 2014.).

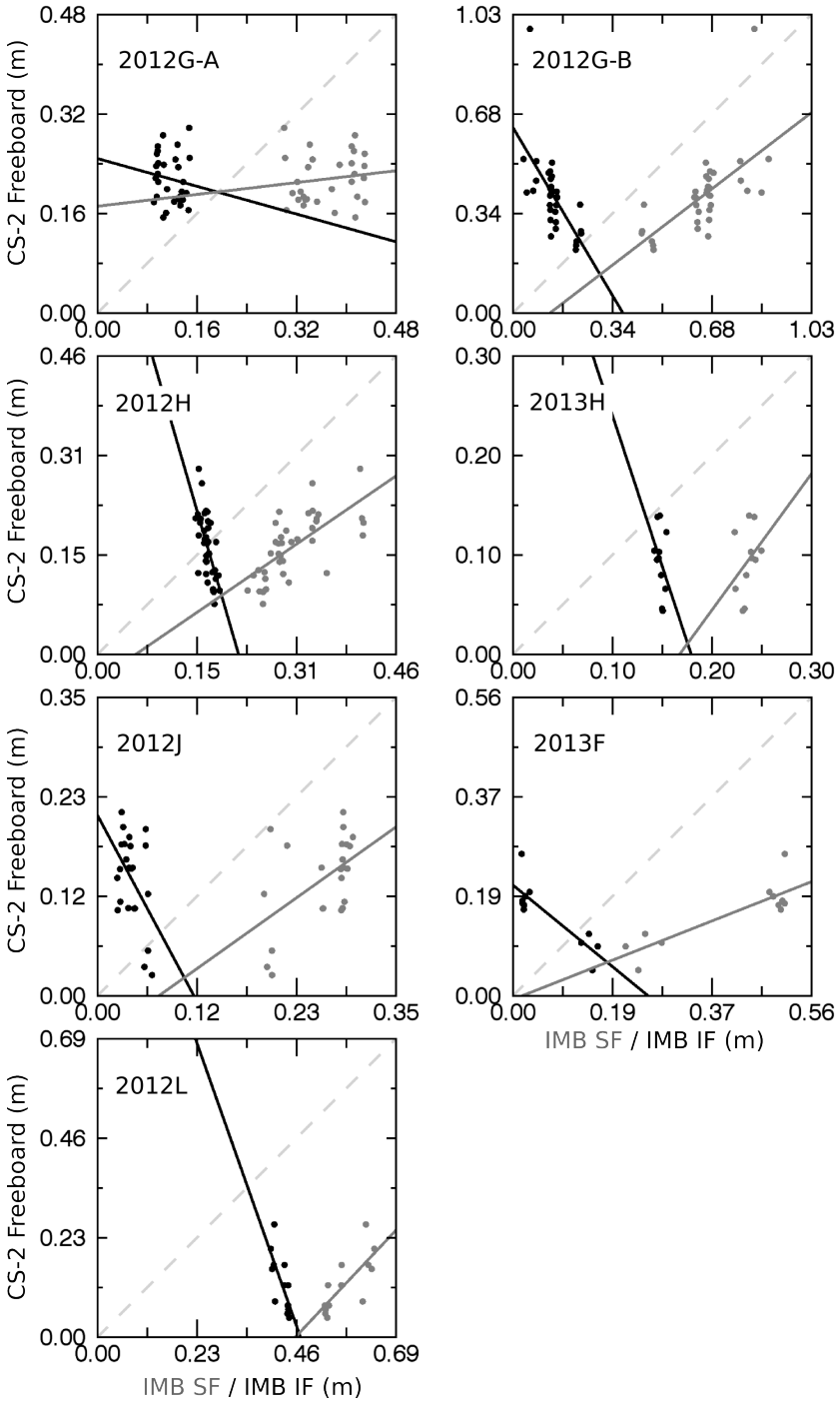

Figure 4.4. Scatterplots of CryoSat-2 freeboard (50 % threshold retrieval) against IMB snow freeboard (IMB SF) and IMB ice freeboard (IMB IF) during the defined event periods. They reveal a positive correlation between CryoSat-2 freeboard and IMB SF, while the correlation between CryoSat-2 freeboard and IMB IF is negative, except for 2012G-A, where correlation is poor in both cases due to the high scattering of CryoSat-2 freeboard.

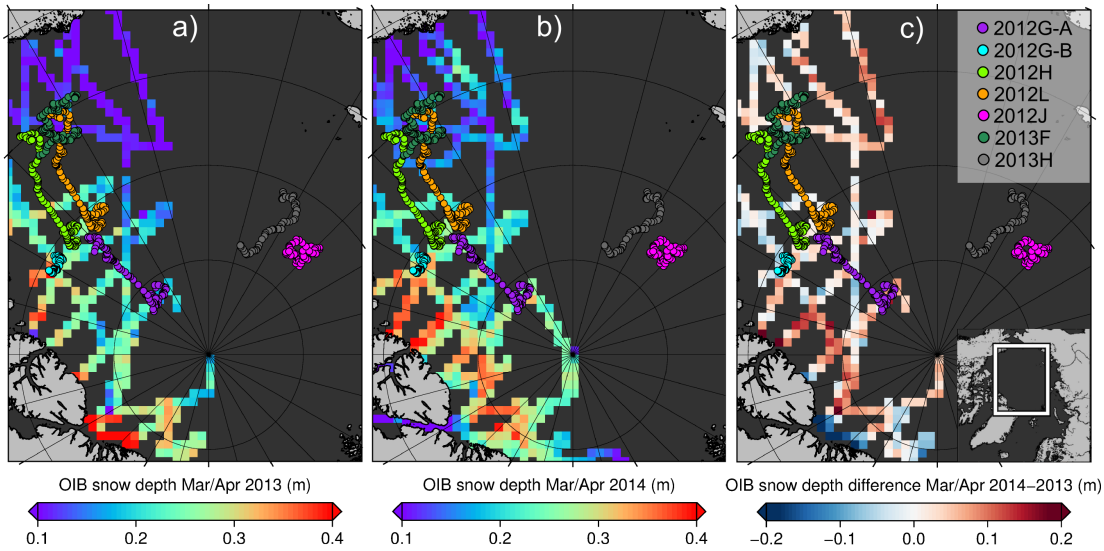

Figure 4.5. Operation IceBridge (OIB) quick-look snow depths from Mar/Apr 2013 (a) and 2014 (b), averaged on a 50 km EASE2 grid and comparable to Figure 1. (c) shows the differences between both years. Red colors indicate an increase of snow depth from 2013 to 2014 for the specific location.

Chapter 5

Evaluation of CryoSat-2 derived sea ice freeboard over fast-ice in McMurdo Sound, Antarctica

Published in *Journal of Glaciology*, 61(226), 285–300. doi: 10.3189/2015JoG14J157

D. Price[1], J. Beckers[2], R. Ricker[3], N. Kurtz[4], W. Rack[1], C. Haas[5], V. Helm[3], S. Hendricks[3], G. Leonard[6], and P.J. Langhorne[7]

[1] Gateway Antarctica, University of Canterbury, Christchurch, New Zealand
[2] Department of Earth & Atmospheric Sciences, University of Alberta, Canada
[3] Alfred Wegner Institute, Bremerhaven, Germany
[4] Cryospheric Sciences Laboratory, NASA Goddard Space Flight Center, MD, USA
[5] Department of Earth, Space Science and Engineering, York University, Canada
[6] School of Surveying, University of Otago, Dunedin, New Zealand
[7] Department of Physics, University of Otago, Dunedin, New Zealand

Abstract

Using in situ data from 2011 and 2013, we evaluate the ability of CryoSat-2 (CS-2) to retrieve sea-ice freeboard over fast ice in McMurdo Sound. This provides the first systematic validation of CS-2 in the coastal Antarctic and offers insight into the assumptions currently used to process CS-2 data. European Space Agency Level 2 ($ESAL2$) data are compared with results of a Waveform Fitting (WfF) procedure and a Threshold-First-Maximum-Retracker-Algorithm employed at 40 % ($TFMRA40$). A supervised freeboard retrieval procedure is used to reduce errors associated with sea surface height identification and radar velocity in snow. We find $ESAL2$ freeboards located between the ice and snow freeboard rather than the frequently assumed snow/ice interface. WfF is within 0.04 m of the ice freeboard but is influenced by variable snow conditions causing increased radar backscatter from the air/snow interface. Given such snow conditions and additional uncertainties in sea surface height identification, a positive bias of 0.14 m away from the ice freeboard is observed. $TFMRA40$ freeboards are within 0.03 m of the snow freeboard. The separation of freeboard estimates is primarily driven by the different assumptions of each retracker, although waveform alteration by variations in snow properties and surface roughness is evident. Techniques are amended where necessary, and automatic freeboard retrieval procedures for $ESAL2$, WfF and $TFMRA40$ are presented. CS-2 detects annual fast-ice freeboard trends using all three automatic procedures that are in line with known sea-ice growth rates in the region.

5.1 Introduction

Although Antarctic sea-ice extent and concentration have been routinely monitored since 1979 (Parkinson and Cavalieri, 2012), the spatial and temporal distribution of sea-ice thickness remains one of the least understood physical components of the global cryosphere (Vaughan et al., 2013). Quantification of thickness is of crucial importance, since when combined with areal data it allows the computation of sea-ice volume. Sea-ice volume provides insight into the heat budget of the Antarctic sea-ice system and quantification of freshwater and saltwater fluxes in the Southern Ocean. Due to the scarcity of in situ measurements of Antarctic sea-ice thickness, there is great demand for improved temporal and spatial thickness data through satellite altimeter observations (Kurtz and Markus, 2012; Xie et al., 2013; Yi et al., 2011; Zwally et al., 2008). Such observations support the capability to monitor trends and in turn provide data to model forecasts of future Antarctic sea-ice properties (Holland et al., 2014; Massonnet et al., 2013).

The use of satellite altimetry for sea-ice thickness estimation is entirely reliant upon the measurement of freeboard (Fig. 5.1). Following this, thickness can be estimated based on the assumptions of hydrostatic equilibrium given input of values for the densities of snow, ice, water and snow thickness (Alexandrov et al., 2010). The ability to accurately measure freeboard and to include information on snow morphology is vital, as any errors in these input factors are greatly magnified in the eventual sea-ice thickness estimation. The European Space Agency's (ESA) Synthetic aperture radar Interferometric Radar Altimeter system (SIRAL) on-board CryoSat-2 (CS-2) is the most advanced satellite radar altimeter instrument for sea-ice freeboard retrieval in operation to date (Wingham et al., 2006; Drinkwater et al., 2004), and at the time of writing is improving understanding of the Arctic sea-ice thickness distribution (Kurtz et al., 2014; Ricker et al., 2014a; Laxon et al., 2013). Given the more heterogeneous and thinner state of Antarctic sea ice, primarily due to its exposed oceanic setting and its highly variable snow distribution and morphology (Ozsoy-Cicek et al., 2013; Massom et al., 2001), the uncertainty in resultant thickness estimates from CS-2 in the Southern Ocean is likely to be higher.

In this study, we validate freeboard measurements from CS-2 over fast ice in McMurdo Sound in 2011 and 2013. The fast ice in this area provides a safe platform for the collation of in situ data (Price et al., 2014), and the area has been well investigated (Gough et al., 2012; Smith et al., 2012; Mahoney et al., 2011; Dempsey et al., 2010; Leonard et al., 2006; Gow et al., 1998; Jeffries et al., 1993). The sea ice in McMurdo Sound is largely uniform and level, with smooth gradients in thickness. The complexity in view of satellite validation is significantly reduced in comparison to the more dynamic pack ice conditions. In common with many other coastal Antarctic regions (Fraser et al., 2012; Fedotov et al., 1998) McMurdo Sound harbors extensive areas of fast-ice neighboring coastal polynyas

and ice shelves as regions of significant sea-ice production (Fedotov et al., 1998; Massom et al., 1998). The performance of radar altimeters for freeboard retrieval in these regions of highly variable ocean conditions is yet to be evaluated, specifically with regard to sea-ice/water discrimination over differing surface types (i.e. leads and polynyas of varying sizes).

Compared to ICESat (the Ice, Cloud and land Elevation Satellite; infrared laser shots with 70m footprints every 170 m along track), the CS-2 radar signal penetrates cloud cover but produces a larger footprint of ∼380 m x 1650 m dependent upon orbit parameters and surface geometry (Bouzinac, 2012). Freeboard retrieval using laser instrumentation is simplified by the fact that the main reflection from the snow surface is well defined. In Ku band (SIRAL center frequency 13.6 GHz) the backscattered radar energy is more susceptible to alteration from surface conditions, but the main reflection is assumed to originate primarily from the snow/ice interface (Laxon et al., 2013). A recent simulation suggests that the influence of snow on sea ice is not negligible as it can broaden the waveform of the returned signal, thus displacing the tracking point (corresponding to the retrieved surface height) toward the altimeter (Kwok, 2014). The influence of snow on the shape of the returned waveform depends on its dielectric properties which are dictated by salinity, liquid water content, density, grain size and temperature (Barber et al., 1995; Hallikainen et al., 1986; Ulaby et al., 1981).

Given the complex snow stratigraphy and snow microwave interaction, there is no consensus on a dominant backscattering surface. For example, no single dominant backscattering surface was found for stratified snow during in situ investigations using a 10-16GHz band instrument, but returns from the snow/ice interface dominated when layering in the snow cover was absent (Willatt et al., 2010). Surface roughness also influences the freeboard retrieval as it directly affects the shape of the returning radar waveform (Hendricks et al., 2010; Drinkwater, 1991; Beaven et al., 1995). Surface roughness may be separated into radar and geometric roughness: the former is associated with small-scale features at length scales comparable to the radar wavelength (in this case 0.02m), and the latter is concerned with large-scale surface undulations (e.g. ridging and cracks). The bandwidth of the compressed high-intensity radar pulse (chirp) of SIRAL (320 MHz) results in a range resolution of 0.47 m. This can resolve neither the air/snow nor the snow/ice interface, making the identification of surface height highly dependent on the slope of the leading edge of the returned waveform (Fig. 5.2). The factors described above exacerbate the accurate localization of a dominant backscattering surface over sea ice, and, in turn, the retracking, a procedure which interprets the waveform to estimate the range to the surface, is complicated (Figs 1 and 2). There are currently two separate approaches using waveform interpretations to establish retracking points: (1) a waveform-fitting approach that takes into account the shape of the returned waveform based on a physical

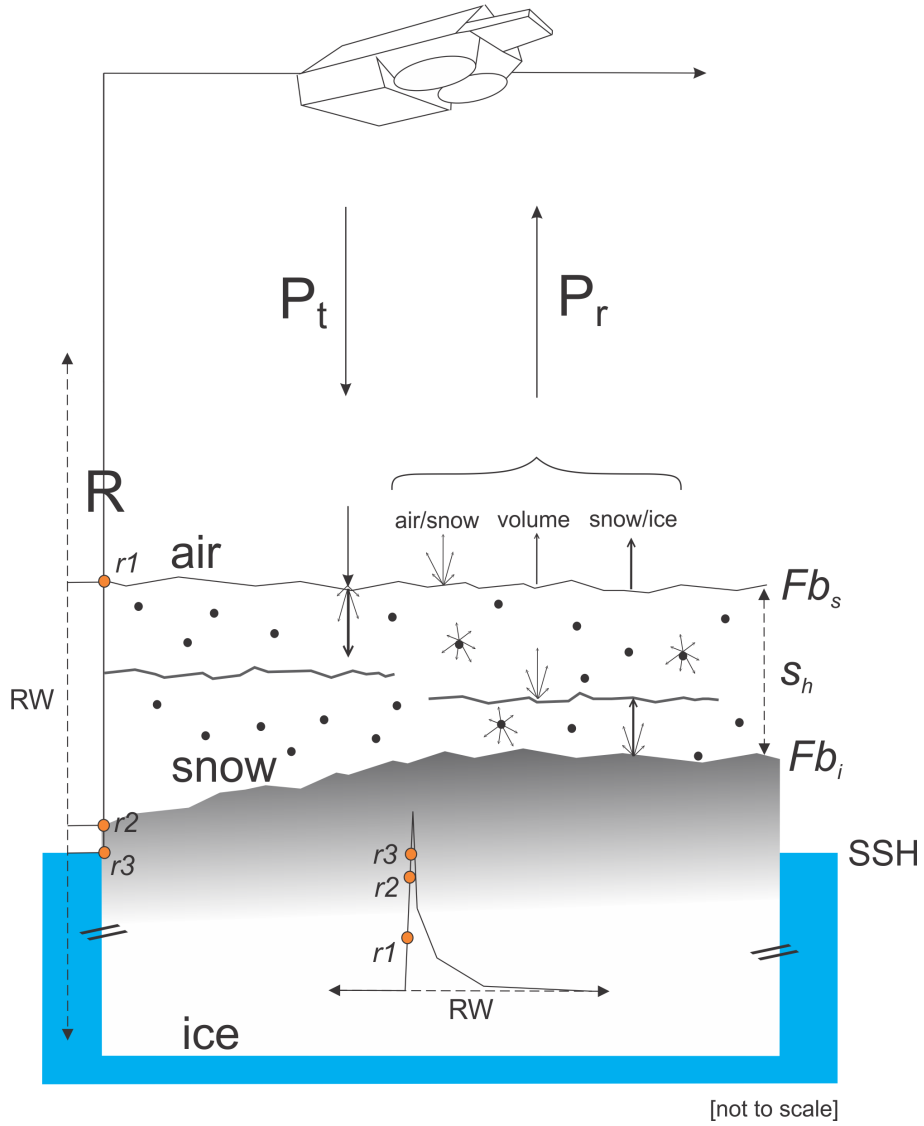

Figure 5.1. Components relating to the interpretation of CryoSat-2 freeboard data. The reception period is maintained by a range window (RW; 120 m in SIN mode) which is constantly adjusted in the vertical dimension to receive echoes from the surface. The transmitted power (P_t) is subject to interaction at the surface from the air/snow interface, volume of the snow cover and snow/ice interface which all influence the power returned to the satellite (P_r). The dominant backscattering surface is variable and is displaced by varying snow depth (s_h), snow layering and snow and ice properties. The retracking procedure is completed, resulting in a range (R) between $r1$ and $r2$ over sea ice ($r3$ over water) dependent upon the assumptions of the respective retracking technique. This range is subtracted from the satellite altitude above the ellipsoid to provide uncorrected height. After application of geophysical corrections, freeboard is obtained by discerning the difference between local sea surface height (SSH) and an interface in the range of the ice freeboard ($\mathrm{Fb_i}$) and the snow freeboard ($\mathrm{Fb_s}$) as measured by the satellite.

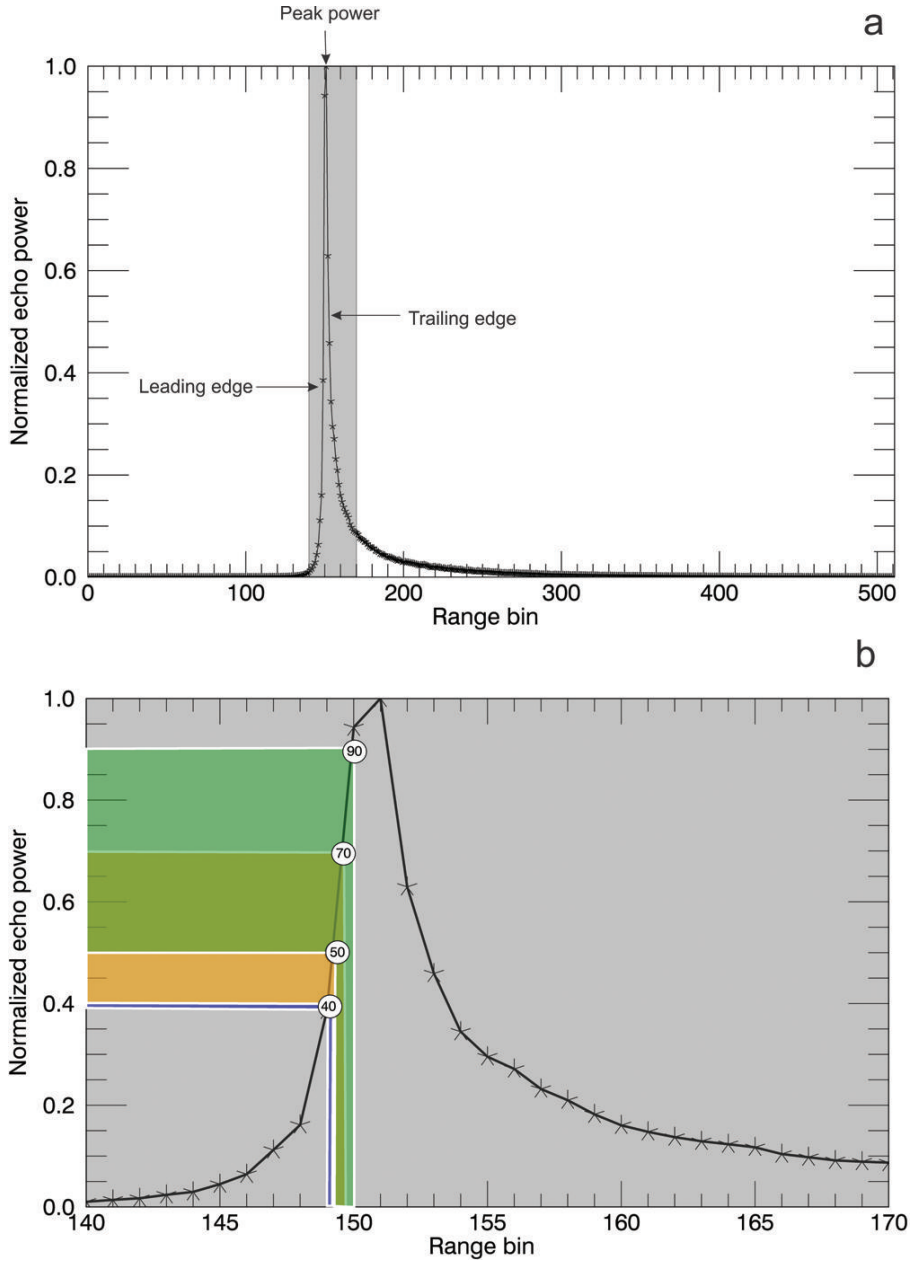

Figure 5.2. Typical CryoSat-2 SIN mode waveform over snow-covered sea ice in McMurdo Sound with labelling of characteristics mentioned in the text. (b) An expanded view of the outlined grey area in (a) from range bins 140-170 (1 bin = 0.234m) and the expected retracking points on the leading edge for the techniques described here: $ESAL2$ (40- 70% orange), WfF (50- 90% green) and $TFMRA40$ (40% blue).

model; and (2) an empirical approach that only considers the leading edge and estimates surface height at a given power threshold. Waveform fitting is the basis for the ESA's Level 2 product (ESAL2) and the Waveform Fitting (WfF) procedure as described by Kurtz and others (2014). The Threshold-First-Maximum-Retracker-Algorithm employed

at 40 % (TFMRA40) is an empirical approach presented by Helm et al. (2014) and applied over sea ice by Ricker et al. (2014a).

In this paper, we assess the assumptions behind the techniques referenced above with a detailed in situ investigation on fast ice in McMurdo Sound. With the addition of Moderate Resolution Imaging Spectroradiometer (MODIS) imagery we undertake a supervised freeboard retrieval procedure in which sea surface height is manually classified on a small number of selected CS-2 tracks. Using this optimal dataset, and additional CS-2 waveform information, we provide insight into the influence of differing surface conditions (snow properties and surface roughness) on the resultant freeboards from each technique: ESAL2, WfF and TFMRA40. This supervised analysis also provides information on the estimated accuracy of CS-2 freeboard retrievals over the fast ice in McMurdo Sound. With information gained in an initial evaluation, we subsequently develop three automatic freeboard retrieval procedures and assess the sea-ice regime in McMurdo Sound for the entirety of 2011 and 2013. First, we describe the study area of McMurdo Sound and in situ information and provide an overview of CS-2 in Section 5.2. In Section 5.3, we describe and discuss the surface height retrieval procedure for CS-2 under each technique. In Section 5.4, we manually identify sea surface height and complete a supervised freeboard retrieval investigation providing freeboard estimates for each technique and report the findings of these results and their implications. Following this, in Section 5.5, we describe the three automatic algorithms used to assess the years 2011 and 2013 in a larger area of McMurdo Sound. Results from these automated procedures are then reported and discussed in the final sections.

5.2 CryoSat-2 assessment in McMurdo Sound

This section describes the study area of McMurdo Sound, the in situ investigation and provides an overview of CS-2. The study area (Fig. 5.3) is located in the southwestern Ross Sea and occupies an area of ∼6400 km^2. McMurdo Sound's proximity to ice shelves and the outflow of cold ice-shelf water from the ice-shelf cavity contributes to sea-ice formation in this area (Price et al., 2014; Gough et al., 2012; Mahoney et al., 2011; Dempsey et al., 2010; Purdie et al., 2006). This influence is hypothesized to be present in similar settings around the Antarctic with potential basin-wide implications (Bintanja et al., 2013; Hellmer, 2004). At the time of writing, McMurdo Sound harbors a first-year (FY) sea-ice regime with extensive areas of highly homogeneous fast ice in its southern and western extremities and the McMurdo Sound Polynya (MSP) at its center. The MSP undergoes complete freeze-up and breakout events throughout autumn and winter but is typically open water during spring and summer. This open-water area can become

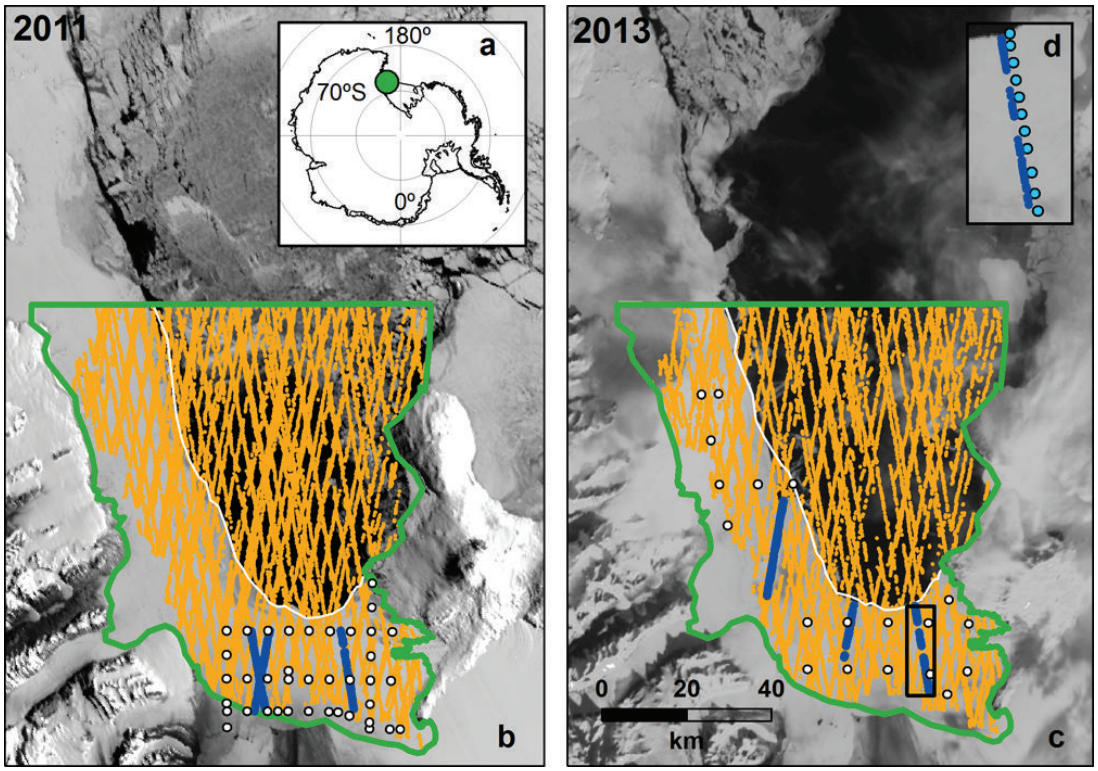

Figure 5.3. (a) Location of the study area within the Antarctic. (b, c) McMurdo Sound and the study area for 2011 (b) and 2013 (c), showing the distribution of CryoSat-2 tracks for those used in the supervised analysis (blue lines), the automatic study period (orange lines) and locations of in situ measurement sites (white dots). The November fast-ice edge is displayed for each year (white line). The full study area for each annual automatic analysis is outlined in green. The validation line in Fig. 5.4 is highlighted by the black rectangle and expanded in (d) to show each in situ measurement point (light blue dots) along the CryoSat-2 track.

intermittently inundated with a cover of sea-ice floes that have drifted south from the Ross Sea.

5.2.1 In situ investigations

During two in situ measurement campaigns in November and December 2011 and 2013, sea-ice freeboard, thickness and snow depth/density measurements were made for comparison with CS-2 freeboard retrievals. The locations of in situ measurements within McMurdo Sound are shown in Fig. 5.3. The in situ measurement campaign in 2011 along with an overview of sea-ice conditions in McMurdo Sound is described in Price and others (2014), and these same measurement procedures were carried out in 2013. Even though the sea-ice conditions in 2013 were very similar to 2011, it is important to note that surface conditions were slightly different with regard to the snow cover and surface roughness.

The first of the differences was related to sea-ice deformation. The sea-ice cover was more deformed in the west in 2013, resulting in higher geometric surface roughness. The second notable difference was in the snow cover. In 2011 the snow was characterized as wind-compacted, with a large variability in hardness, density and grain size. Grain size was generally large near the ice (∼3 mm), and smaller in the upper layers, typically ∼0.5 mm and smaller. Where snow was 0.20 m in thickness we found two to three layers, with densities varying between 330 and 450 kg m^{-3} with no significant correlation between depth and density. In 2013 a similar situation existed, but both thickness and layering were reduced, while radar roughness was likely higher given a less uniform snow surface at the centimeter scale. In both years the distribution was highly variable, with many different snow types present.

5.2.2 CryoSat-2

Launched in April 2010, CS-2 operates in a near-circular polar orbit with an inclination of 92° and has a repeat cycle of 369 days with a subcycle of 30 days. Its on-board altimeter, SIRAL, operates at a center frequency of 13.6 GHz and is normal-incidence, with two receiver chains operating in two modes over sea-ice areas (Bouzinac, 2012). Its dedicated sea-ice mode uses synthetic aperture radar (SAR) processing for height retrievals along-track at an improved spatial resolution. In addition, being pulse-limited across track results in a footprint size of approximately 380 m x 1650 m, with along-track sampling at ∼300 m intervals permitting enhanced along-track ice/water discrimination and higher sampling (Bouzinac, 2012). In Antarctic coastal regions, SIRAL switches to SAR interferometric (SIN) mode for ice-sheet margin investigation. Interferometric processing discerns the arrival angle of radar returns via phase comparison of the returning signal. This permits them to be correctly positioned on the Earth's surface, and off-nadir returns to be accurately ranged (Bouzinac, 2012; Wingham et al., 2006). This is a necessity in complex terrain, where off-nadir reflections can be received by the satellite prior to nadir reflections. The SIN mask extends out to a maximum distance of ∼300 km from the Antarctic coastline and ice-shelf margins. Due to the study area's proximity to the Antarctic continental coast it falls within the SIN mask. To account for the increased range over which the surface may be encountered by the incident radar beam in complex terrain, a longer tracking window is permitted in SIN mode. At the same time the reduction in burst-repetition frequency decreases the number of resulting measurements by a factor of four compared to SAR mode (Bouzinac, 2012; Wingham et al., 2006). The measurement range window is segmented into 512 bins providing a range sampling of 1.563 ns (0.234 m in vacuo). A CS-2 SIN mode example waveform with labelling relevant to the text is shown in Fig. 5.2. The surface is maintained in a range window along track, which constantly adjusts to keep the leading edge at a specific point near the center of the

window (Bouzinac, 2012). Energy from the surface that is returned to the satellite builds above the noise level and increases along the leading edge to the peak power. This then decays (the trailing edge) to the end of the tracking window. The retracking procedure is then used to identify the point on the waveform that provides the range to the surface. Multiple methods exist to execute this procedure based on different assumptions about the interaction of radar energy and the surface.

5.3 Tracking surface height from CS-2 waveforms

We begin our analysis with a description of the respective retracking procedures for each method. The retracking procedure aims to provide the best estimate of range between the satellite center of mass and the dominant backscattering horizon on the Earth's surface. This is achieved by interrogating ESA's baseline B Level 1B (SIR_SIN_L1) waveforms. It results in geolocated surface heights (h^*) which are referenced to the World Geodetic System 1984 (WGS84) ellipsoid after subtracting retracked range from the satellite's altitude.

5.3.1 European Space Agency Level 2 data product (*ESAL2*)

We utilize ESA baseline B Level 2 SIN mode (SIR_SIN_L2) data which have already undergone a retracking procedure (Bouzinac, 2012) . Using SIR_SIN_L1 the ESA processor applies a model fit to determine heights from waveforms fitted to the model echo shape (Wingham et al., 2004, 2006). The ESA waveform retracker is described as a 'customer furnished item' in the CryoSat Product Handbook (Bouzinac, 2012) , but no further information is provided by ESA at the time of this publication. Using SIR_SIN_L1 and SIR_SIN_L2 data in unison from CS-2 data within our study area, the retracking point is shown to vary on the leading edge over a range of 40-70 % of peak power (Fig. 5.2). Using phase information, a correction for off-nadir scattering is also applied in this product. With the available literature we are unable to conclude with confidence which surface (air/ snow or snow/ice) is expected to dominate the backscatter, or what assumptions are made in the model.

5.3.2 Waveform Fitting Procedure data product (*WfF*)

Kurtz et al. (2014) provide an overview of this product. Surface height is estimated by fitting a physical model to the SIR_SIN_L1 waveforms. The model parameters include the surface roughness, which is assumed to be Gaussian, and the variation of the backscatter with incidence angle. Dependent upon the parameters described in Kurtz

et al. (2014), WfF establishes its retracking point at ∼50-90 % (Fig. 5.2) of peak power on the leading edge for non-specular returns and assumes that the dominant backscattering surface is the ice/snow interface. For specular returns, the model converges to the shape of the compressed transmit pulse and the retracking point is near the point of peak power, but can also be beyond the leading edge due to the finite sampling resolution of the waveform. For the SIN mode data used in this product, the phase information is used to determine the angle to the point of closest arrival determined by the retracking point. A correction for the retracked height, due to off-nadir scattering, is determined and applied from the phase information using the procedure described by Armitage and Davidson (2014).

5.3.3 Threshold-First-Maximum-Retracker-Algorithm 40 (*TFMRA40*)

This product is based on SIR_SIN_L1 waveforms, but phase information from the returning echo is discarded. The range of the main scattering horizon is obtained by applying a Threshold-First-Maximum retracker to the waveforms. In this study we use a threshold of 40 %. The processing follows Ricker et al. (2014b) by:

1. Oversampling of the original waveform by a factor of 10 using linear interpolation.
2. Smoothing of the oversampled waveform by applying a running mean with a width of ten range bins to reduce noise.
3. Determination of the first maximum by the derivative of the interpolated curve.
4. Retrieval of the ellipsoidal elevations by tracking the leading edge of the first maximum at 40 % of the peak power (as in Fig. 5.2).

The main scattering horizon is assumed to be close to the surface, whether this is the air/snow interface or, in the absence of snow cover, the ice/air interface.

5.3.4 Tracking of sea surface height

The sea surface state at the time of the satellite overpass can alter the shape of the returning waveform. Over leads, given their small fetch, the surface is typically smooth. This provides a uniform surface with a characteristic specular waveform response, an ideal surface for both discrimination of water from sea ice and the use of consistent techniques for tracking the sea surface. However, as the size of the open-water area being referenced is increased so is its susceptibility to wind. This is clearly evident over the polynya area in McMurdo Sound, which does not exhibit the typical specular waveform expected

from a lead. This is the first of three issues related to the identification of sea surface height (SSH) noted in this study and is described in more detail below. These areas were observed to hamper the identification of SSH in certain sea conditions. When the significant wave height (SWH) is increased by wind forcing, the slope of the leading edge of the radar waveform is flatter due to increasing off-nadir contributions. In the case of $TFMRA40$ this influence resulted in insufficient separation of fast-ice elevation retrievals from sea surface retrievals (i.e. SSH was too high relative to the sea-ice surface). Such an influence was not observed on the $ESAL2$ or WfF techniques that retrack 'higher' on the leading edge and attempt to account for physical differences in surface roughness and incidence angle backscatter variations. This emphasizes the need for the inclusion of an additional surface type to the $TFMRA40$ procedure. The surface type polynya has been added to the original three, ocean, lead and sea ice (Ricker et al., 2014b), to accurately record SSH for the open-water area in McMurdo Sound. Over surfaces flagged as polynya the surface is tracked at 60 %, as opposed to 40 % over leads and sea ice. This increase in the retracking threshold accommodates for the flatter leading edge forced by a higher SWH. This amendment improved agreement between $TFMRA40$ freeboard retrievals and in situ measured freeboard data.

Secondly, the occurrence of 'mixed' surface types within the CS-2 footprint produces noisy waveforms. Regions in which larger open-water areas are intertwined with sea-ice floes and smaller open-water areas, more representative of leads, caused complications with the retracking procedure. These conditions were more prevalent in 2011, when ice floe conditions were more variable in the regions classified as open-water areas. The WfF procedure was influenced by this, which led to SSH retrievals being too low. Slight amendments were applied to attempt to discard noisy waveforms that were causing a delay in range. These amendments, which attempted to remove noisy waveforms by assessing the occurrence of early peaks in power before maximum power, and altering the initial guess of the power to be retracked, resulted in negligible improvements. Further improvement of this procedure is a current research focus. Thirdly, as the leading edge is not necessarily affected over its entire height in the same manner, this can result in the influence of sea conditions being variable between retrackers that are operating at different positions on the leading edge (Fig. 5.2). This introduces an inter-retracker bias given the same sea surface conditions. The quantification of these errors is not within the scope of this study given our inability to confidently establish sea surface conditions at the time of data acquisition. Although we are not able to fully resolve all the issues discussed in this section we include them here to provide context for the discussions which follow.

5.4 Supervised freeboard retrieval procedure

The retrieval of sea-ice freeboard from radar altimetry requires multiple processing steps. These steps remove spurious influences on the height profile, revealing desired variations driven by freeboard. At this stage the main uncertainties in the CS-2 freeboard retrieval are driven by:

1. The ability of an algorithm to distinguish between water and sea ice and therefore accurately establish SSH.
2. The availability and accuracy of snow depth information.
3. The limited understanding of the reflected waveform as a function of surface and volume scattering.

Here we minimize the uncertainty under point 1 with the use of MODIS optical imagery by undertaking a supervised identification of the sea surface, establishing a more accurate SSH. We greatly reduce the uncertainty from point 2 with available in situ snow depth/density information. We use these additional data sources, and retrieve a supervised freeboard ($\mathrm{Fb_{sup}}$) for six CS-2 tracks, three from each year 2011 and 2013, for the period mid-November to early December (Fig. 5.3). This places the in situ measurements in near temporal coincidence with the CS-2 data which were acquired between 21 November and 4 December. The uncertainty introduced by point 3 is expanded upon in Section 5.6.

We begin our analysis using h^* estimated for each technique in Section 5.3, which is first corrected for varying influences on the transmitted radar wave as it propagates through the atmosphere (cr_t): dry tropospheric, wet tropospheric and ionospheric corrections (Bouzinac, 2012). The ellipsoidal height is then reduced to a quasi-orthometric height (h) after subtracting geoid height (N) provided by the Earth Gravitational Model 2008 (EGM2008). This approximates mean sea level (MSL). To construct a SSH from this, further information is needed to quantify the sea surface height anomaly, which is the sum of the varying influences of tides (t) and atmospheric pressure and wind (i). No corrections are applied for t at this stage, as the tidal gradient was found to be negligible over the spatial area in the supervised assessment. This was determined through the use of global navigation satellite systems (GNSS) stations deployed on fast ice in McMurdo Sound which showed no tidal gradient across the assessed distances (Price et al., 2014). Given the ∼50 km distance, we also expect the influence of i to be negligible. We therefore arrive at h with

$$h = h^* + cr_\mathrm{t} - N \tag{5.1}$$

Using MODIS imagery we identify open-water areas along each CS-2 track and manually prescribe surface types of water or sea ice to each h value. The construction of SSH requires the removal of surface height outliers over the water surface type. The mean is largely biased by such outliers, so, in this case, where we are confident open water dominates, we use the median to establish the supervised SSH ($\mathrm{SSH_{sup}}$). We sample ∼25km sections along track, which provides ∼100 individual h values from which to construct $\mathrm{SSH_{sup}}$. Radar freeboard ($\mathrm{Fb_{radar}}$) is then derived by

$$Fb_{\mathrm{radar}} = h - \mathrm{SSH_{sup}} \tag{5.2}$$

Given the assumptions about each retracker with regard to snow penetration, we follow Kurtz et al. (2014) and freeboard is then derived with the addition of a correction for the speed of light in snow. This correction (h_{c}) over sea-ice areas is given by:

$$h_{\mathrm{c}} = s_{\mathrm{h}} \left(1 - \frac{c_{\mathrm{snow}}}{c}\right) \tag{5.3}$$

where s_{h} is the snow depth, c the speed of light in a vacuum, and c_{snow} the speed of light in the snowpack following Tiuri et al. (1984) parameterized as

$$c_{\mathrm{snow}} = \frac{c}{\sqrt{1 + 1.7\rho_{\mathrm{s}} + 0.7\rho_{\mathrm{s}}^2}} \tag{5.4}$$

where ρ_{s} is the snow density ($\mathrm{gcm^{-3}}$) measured as 0.385 $\mathrm{gcm^{-3}}$ in McMurdo Sound (Price et al., 2014). This value was also measured as the mean snow density from in situ measurements in 2013. s_{h} is provided by the spatial interpolation of in situ snow depth measurements. With regard to snowpack penetration by the incident radar wave we assume full penetration for $ESAL2$ and WfF and no penetration for $TFMRA40$. The reduction of c in the snow cover results in an increased range estimate from satellite to surface. This will force a negative bias in the resultant freeboard if uncorrected; we therefore arrive at $\mathrm{Fb_{sup}}$ for each respective retracker under the manual assessment over fast ice with

$$Fb_{\mathrm{sup}} = Fb_{\mathrm{radar}} + h_{\mathrm{c}} \tag{5.5}$$

Table 5.1. Mean freeboard values, standard deviations and sample sizes (n) derived by each retracker by the supervised procedure in austral spring (November and December) 2011 and 2013 and comparison to interpolated in situ mean ice (F_i) and snow freeboards (F_s) . The satellite tracks from which each (Fb_{sup}) mean is derived are displayed in blue in Fig. 5.3.

Retracker	Spring 2011 (m) Fb_{sup} n = 148	Spring 2013 (m) Fb_{sup} n = 163
Fb_i	0.22 ± 0.07	0.21 ± 0.04
Fb_s	0.33 ± 0.01	0.26 ± 0.04
$ESAL2\ Fb_{sup}$	0.29 ± 0.14	0.24 ± 0.17
$WfF\ Fb_{sup}$	0.36 ± 0.13	0.17 ± 0.13
$TFMRA40\ Fb_{sup}$	0.36 ± 0.15	0.29 ± 0.11

We treat Fb_{sup} outliers by removing any retrieval that deviates by >3 standard deviations from the mean over the sea ice area. Finally we ensure data sets are comparable with the manual removal of Fb_{sup} values that are not available for all three products.

5.4.1 Supervised freeboard retrieval results

In this subsection, we provide results from the supervised analysis of CS-2 derived freeboards from each retracker. We compare these results to in situ freeboard measurements and use this in combination with complementary field and satellite data to relate the effect of surface conditions on the resultant Fb_{sup} values. In situ ice freeboard (F_i) and snow freeboard (F_s) are provided from the interpolation of in situ measurements and extracted to be spatially coincident with each individual CS-2 Fb_{sup} retrieval (the tracks of which are shown in Fig. 5.3). This step was undertaken to provide a better spatial comparison between in situ measurements and CS-2. The mean values of the interpolated points extracted at each Fb_{sup} retrieval agree to within 0.01 m of the in situ mean values. The variability introduced by the interpolation is largest with regard to Fb_s driven by variations in s_h. Leave-one-out cross-validation indicates that a maximum deviation of 0.05 m can be expected (Price and others, 2014). Fb_{sup} which are the mean values of the three CS-2 tracks in each year are shown with in situ means in Table 5.1. The retracking techniques produce Fb_{sup} mean values ranging from 0.17 to 0.36 m which are in line with the range of in situ measured freeboards in McMurdo Sound of 0.21 to 0.33 m. All retrackers provide higher Fb_{sup} estimates in 2011 than in 2013 when the snow was deeper. 2013 Fb_{sup} values for each technique are in agreement with what is expected given the assumptions of the described retrackers (see Fig. 5.2 and difference in range),

WfF the lowest and TFMRA40 the highest. WfF shows closer agreement with F_i while $TFMRA40$ freeboards are closer to F_s. $ESAL2$ Fb_{sup} is established between F_i and F_s. Therefore, the trivial relationship between differences in retracked range and resultant freeboard values is maintained in 2013. The comparison is complicated in 2011 with regard to WfF, as its Fb_{sup} value is 0.19 m higher than in 2013 with only a 0.01 m change in F_i recorded in situ. The cause of this discrepancy is unclear. It is likely that interference with SSH_{sup} establishment, as alluded to in Section 5.3.4, played a role in the high freeboard value for WfF , but we also need to consider the influence of the snow cover. The full snow-cover penetration assumption of the WfF method may not be fulfilled given a smooth snow cover that can be an effective scatterer of the incident radar energy. When the echo power from the snow/ice interface and that from the air/snow interface have a similar magnitude, a positive freeboard bias may be introduced (Kwok, 2014; Kurtz et al., 2014). This bias is estimated to reach a maximum of 0.04 m for homogeneous snow conditions (Kurtz et al., 2014). It is likely to have played a more significant role here due to the snow stratification and wind crusts at the surface. From the limited information about the retracking procedure for $ESAL2$ we would expect to see a similar relationship. Such a relationship is observed, with $ESAL2$ Fb_{sup} 0.05 m higher in 2011 than in 2013.

To provide further insight into the influence of snow cover and ice conditions on the radar signal, we show Fb_{sup} along a coincident in situ validation line on 27 November 2013 (Fig. 5.4). The validation measurements along this line were temporally coincident to within 3 hours of the CS-2 overpass. It should be noted that due to a satellite orbit maneuver the validation line was ∼1km east of the CS-2 ground track. Visually we observed no significant changes to the characterized sea-ice surface conditions or snow depth over this distance and therefore find the in situ and CS-2 datasets comparable. The surface conditions on the sea ice varied along the validation line from north to south. Clear differences in Fb_{sup} are displayed between the techniques. Mean Fb_{sup} for WfF shows good agreement with F_i. $ESAL2$ mean Fb_{sup} is in better agreement with Fs, but the response of the height retrievals to surface conditions follows a similar pattern to that observed for WfF. $TFMRA40$ has a very consistent Fb_{sup} profile which exhibits minimal response to changing surface conditions, producing values that closely agree with Fs across the whole profile. We are able to assess the response of each of the retracking techniques to the presence of a homogeneous section of dry snow in segment 4 (Fig. 5.4). For all techniques, Fb_{sup} appears to track an interface which is in good agreement with measured in situ Fi over segment 4. $ESAL2$ and WfF record the in situ measured decrease in Fb_i in the central part of the segment. Further in support of WfF assumptions, its mean Fb_{sup} value agrees to within 0.01 m of in situ measured Fi with no positive bias as CS-2 passes over this area of relatively homogeneous snow cover (segment 4: mean WfF Fb_{sup} =0.19m, in situ F_i =0.20m, in situ F_s = 0.37 m). However, for the 2011 WfF

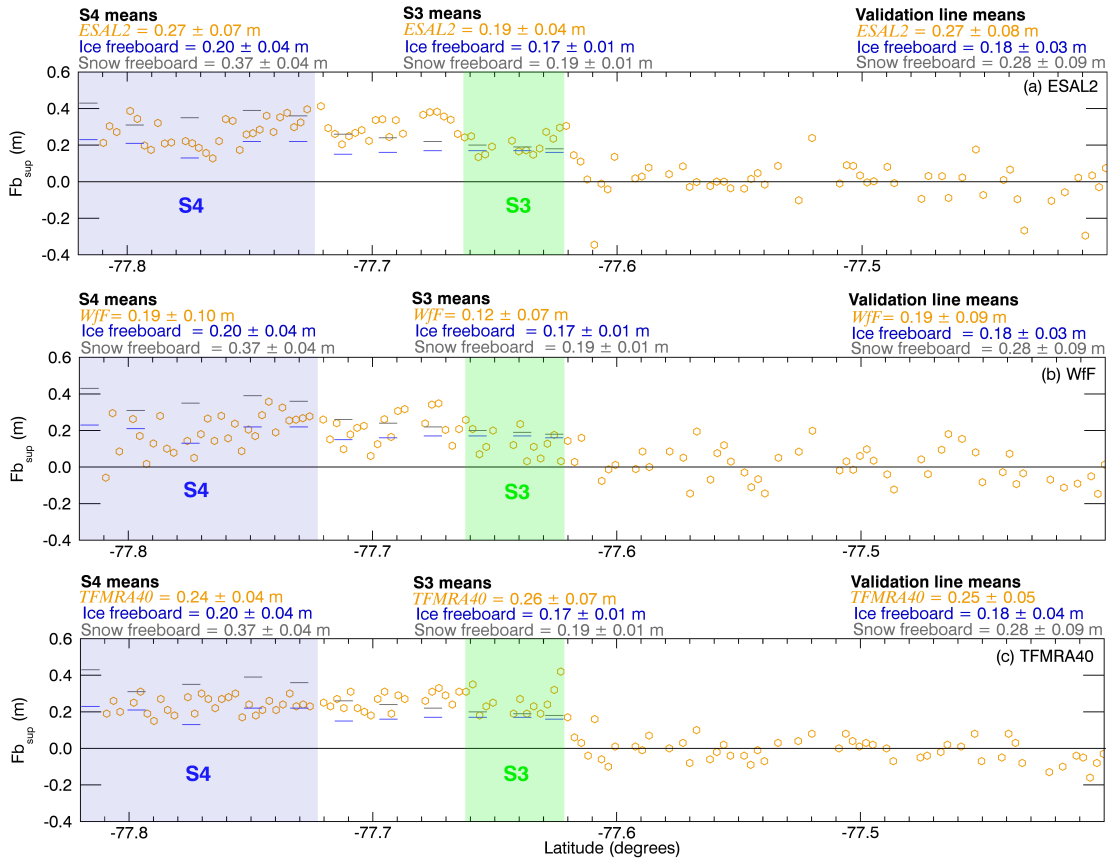

Figure 5.4. Comparison of each method along a validation line coincident with a CryoSat-2 overpass on 27 November 2013 for (a) $ESAL2$, (b) WfF and (c) $TFMRA40$. In situ measured ice and snow freeboards are shown as blue and grey horizontal lines respectively. Segments 3 (S3) and 4 (S4) in Fig. 5.5 are also shown. Sea surface height was identified using the supervised procedure. The CryoSat-2 height profile begins in the north over open water and progresses south over the fast-ice edge at the beginning of segment 3. The freeboard retrievals for each respective retracker are displayed as orange circles, and the validation line statistics describe the sea-ice area only. S3 and S4 means are also displayed for each technique, along with the ice freeboard and snow freeboard measured in situ.

freeboard, measured when the snow cover was smoother and more layered in comparison to segment 4 in 2013, the mean WfF $\mathrm{Fb_{sup}}$ value is 0.36 m, 0.14 m higher than $\mathrm{F_i}$ (Table 5.1). Both $ESAL2$ and WfF clearly exhibit a large variability in freeboard retrievals over sea ice in response to either snow or ice conditions.

We attempt to separate the influences of snow and sea-ice conditions using near-coincident TerraSAR-X (X-band) imagery, in situ measurements, and observations. We provide four segments in McMurdo Sound in 2013 over which sea-ice geometric roughness (GR) and radar roughness (RR) varied. Considering the similar wavelengths in X band (∼0.03 m) and Ku band (∼0.02 m), and also assuming the incidence angle dependence of

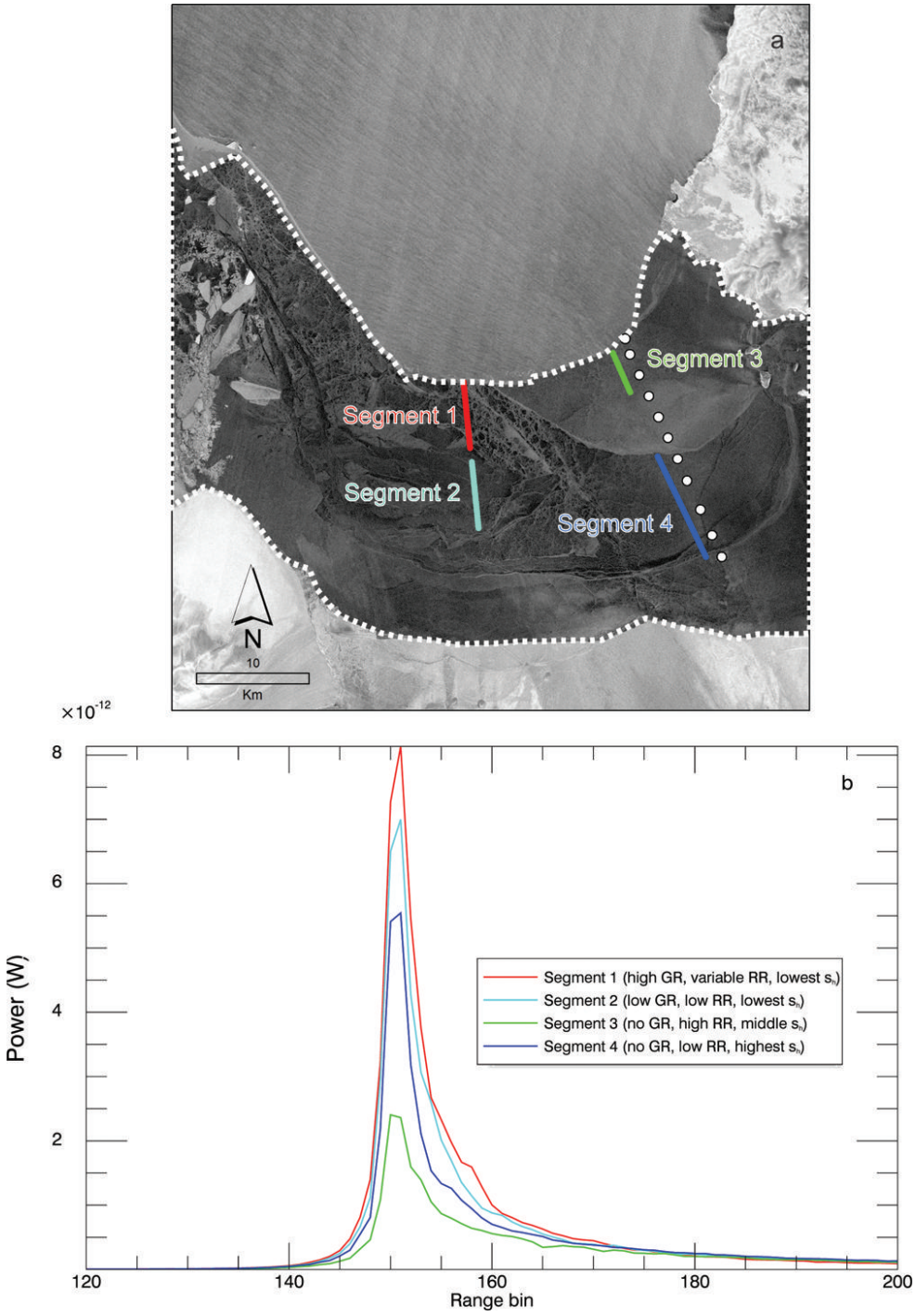

Figure 5.5. (a) Segments 1-4 over the first-year sea-ice area (bounded by white dotted line) overlaid upon a TerraSAR-X radar image from 28 November 2013. TerraSAR-X image (courtesy DLR (German Aerospace Center)). (b) Mean waveforms from these segments plotted as power for multiple sea-ice surface conditions with variable geometric roughness (GR), radar roughness (RR) and snow depth (s_h).

backscattering properties is dominated by surface scattering, a near-inverse relationship between backscattered power between TerraSAR-X (40° incidence angle) and CS-2 (normal incidence) can be expected (Ulaby et al., 1982). In the TerraSAR-X image the relatively bright areas on level sea ice (bounded by a white dotted line in Fig. 5.5a) are rough with respect to the radar wavelength, and the dark areas are smooth. For the sea-ice area, we assess the differences in CS-2 waveforms that have been averaged and stacked to represent these different segments. The numbers of waveforms averaged to create each representative waveform were between 15 and 28. We identify an area of high GR (segment 1: FY ice that has likely been deformed by storm activity) and low GR segment 2: older FY ice which was less deformed) over the FY fast-ice area. These were established primarily from field observations, with the TerraSAR-X image as support. Segment 1 (high GR, variable RR, lowest s_{h}) causes the largest power return, closely followed by segment 2 (low GR, low RR, lowest s_{h}). It is clear that other variables also influence the signal return, which is evident from comparison of segments 3 and 4. Segment 3 has the lowest power return of the assessed waveforms and exhibits high radar backscatter in the TerraSAR-X image. This indicates that RR is high. These observations are supportive of the fact that RR is the dominant influence on the power returned to the satellite and that GR is playing a secondary role. It is difficult to attribute the influence of volume scattering from snow, as no areas with the same RR are available with large differences in snow depth.

In an attempt to assess the influence of snow depth, we look at two tracks in 2011 that exhibited a larger difference in snow depth for which we expect RR to be less variable. For these example tracks, the waveforms retrieved over snow (mean depth 0.20 m) and those retrieved over reduced snow (mean depth 0.07 m) are displayed in Fig. 5.6 with the retracking points for each technique. These waveforms are the mean normalized echo power of ∼50 waveforms and are aligned by peak power to achieve comparativeness between each technique. The mean retracking point for each waveform for each technique is also displayed. It should be noted here that comparison of their absolute range differences cannot be inferred from the available information, only the inter-example variation in the waveform shape. It is shown that in the presence of a snow cover of ∼0.20m the slope of the leading edge becomes shallower, and that the power of the trailing edge is increased along with the overall width of the waveform. This finding is comparable to results of simulations of CS-2 waveform responses to increasing snow cover provided by Kwok (2014).

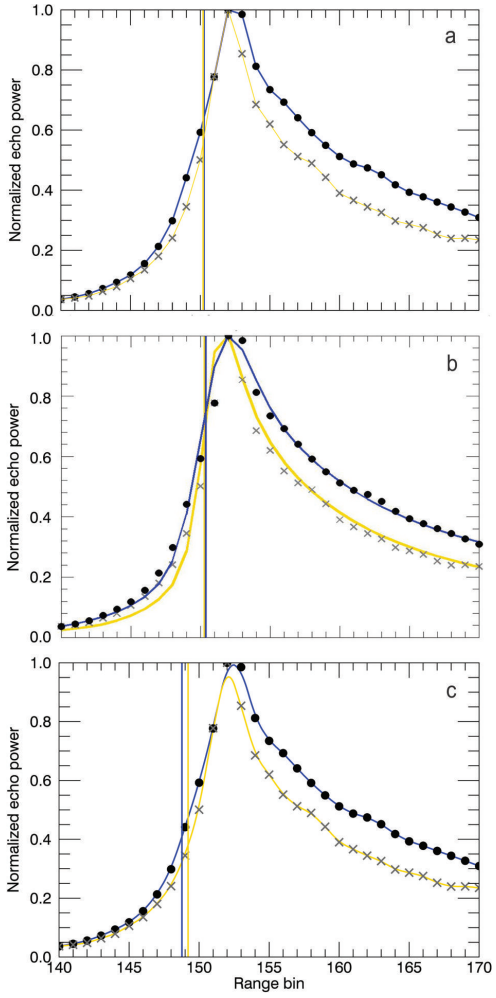

Figure 5.6. Mean waveform examples for sea ice in 2011 with significant snow cover (circles and blue fits) and minimal snow cover (crosses and orange fits). The area with significant snow cover had a mean snow depth of 0.20 m with consistent coverage. Over the minimal area a mean snow depth of 0.07 m was measured with a patchy distribution. (a) The retracking points for $ESAL2$ with linear fits between each bin; (b) the retracking points for WfF with respective model fits; and (c) the retracking points for $TFMRA40$ with interpolated curves.

5.5 Automatic freeboard retrieval procedure

In this section we develop automatic freeboard retrieval procedures without the prerequisite for coincident satellite imagery for the establishment of SSH. The automatic differentiation of sea ice and water is a fundamental requirement for large-scale altimetric sea-ice freeboard retrieval. Automated methods generally fall into two categories, the first relying on the use of information received in the returning signal from the surface and the second on mathematical generalizations that approximate expected surface conditions, or, a combination of the two. In the case of CS-2, methods currently presented in the literature

(Kurtz et al., 2014; Ricker et al., 2014a; Laxon et al., 2013) fall into the first category, following similar investigative procedures initially demonstrated by Peacock and Laxon (2004). These contemporary methods use the pulse peakiness and stack standard deviation, among other parameters, to differentiate between radar returns from small open-water leads in the sea-ice cover and sea-ice floes. In the second category, the expected amount of water along-track is given a value, and the heights of this lowest percentage are averaged for a certain segment of track, giving a sea surface height (Zwally et al., 2008; Price et al., 2013). This approach, commonly termed along-track filtering, is yet to be examined in the literature with respect to CS-2. The three automatic retrieval procedures used for each retracking method are described in the following subsections.

Following from h established in Section 5.4, all data undergo the same additional corrections to produce comparable datasets. h is further corrected for t and i to give H:

$$H = h + t + i \tag{5.6}$$

The influence of i is accounted for using a dynamic atmosphere correction and compensates for the influence of barometric pressure and winds on the sea surface. t is the sum of corrections for ocean tide, long-period equilibrium tide, ocean loading tide, solid earth tide and the geocentric pole tide. Further details on the corrections applied for t and i are given in Bouzinac (2012). These additional corrections accommodate for the larger geographical region under investigation in the automatic procedure (Fig. 5.3) over which tidal and atmospheric effects will be influential on the 'flattening' of the height profile. Each method then produces its own automatic SSH ($\mathrm{SSH_{auto}}$) to provide $\mathrm{Fb_{auto}}$ as

$$Fb_{\mathrm{auto}} = H - \mathrm{SSH_{auto}} \tag{5.7}$$

No adequate snow depth information is available for the two annual periods assessed by the automatic procedure, so no correction is applied for h_{c}. The procedures for attaining $\mathrm{SSH_{auto}}$ for each technique and other relevant amendments are described in the following subsections.

5.5.1 *ESAL2* automatic SSH identification

Measurement quality flags provided in the CS-2 Level 2 record structure were used to improve the quality of the dataset. H values are discarded if the following parameters in the product are flagged as poor: block degraded, orbit error, orbit discontinuity, height

error, calibration caveat, backscatter error, peakiness error, SIN cross-track angle error, SIN receive channel 1 error, SIN receive channel 2 error, mispointing error and delta time error which are given in Bouzinac (2012). In SIN mode, the off-nadir location of the height retrieval can be determined from phase information of the dominant scattering in the power echo, which over sea-ice areas can be significantly off-nadir (Armitage and Davidson, 2014). This ability prevents underestimations of ocean elevation as a result of 'snagging' from leads located off-nadir, providing a reduction in noise over height profiles. According to the across-track offset computed from the phase difference, open water and level sea-ice areas also produce echoes geolocated off-nadir. From assessment of ∼800 separate elevation retrievals over open water in McMurdo Sound from two tracks in 2013, identified by comparison with near-coincident MODIS imagery, the mean deviation from nadir was 270 ± 70 m. We apply a removal threshold of ± 750 m from nadir simply to limit information to the expected nadir footprint area, maintaining comparativeness to the TFMRA40 method and to in situ measurements.

To remove height outliers we apply a vertical threshold of ± 2 standard deviations of the mean to each track. Heights outside this threshold are discarded.

We use the Level 2 parameter peakiness (P) to differentiate between three surface types: open water, leads and fast ice. P is suggestive of how sharply peaked the returning waveform is, and is defined as the ratio of the highest bin value to the mean of all bins above the retracking point (Bouzinac, 2012). P ranges between 0 and 120 in our investigation area (Fig. 5.7). High P values are indicative of leads, which are geometrically of similar size to the radar footprint and typically have specular surfaces. Low P values are indicative of open-water areas that are geometrically larger than the radar footprint and are typically diffuse surfaces. Fast-ice P values are between these two extremes but are affected by sea-ice surface conditions. We establish thresholds for these surface types after comparison of P values over certain surface types in the study region as indicated by MODIS and TerraSAR-X imagery and knowledge of the sea-ice regime. P has a large standard deviation even when a certain surface type is completely isolated, indicating it is highly sensitive to small changes in surface conditions.

First we assessed the P threshold for leads. It is very challenging to constrain such a value, due to the difficulty of achieving coincidence between CS-2 measurements and satellite imagery. Therefore, we investigated P values in March when sea ice in McMurdo Sound starts to freeze and the surface is dominated by developing ice floes. At this time, leads are abundant and we take the upper quartile of P values as representative of the leads surface type ($P > 90$) for both years.

The two remaining surface types require further scrutiny due to overlaps in their P distributions. McMurdo Sound was assessed in February 2013 when it was dominated by

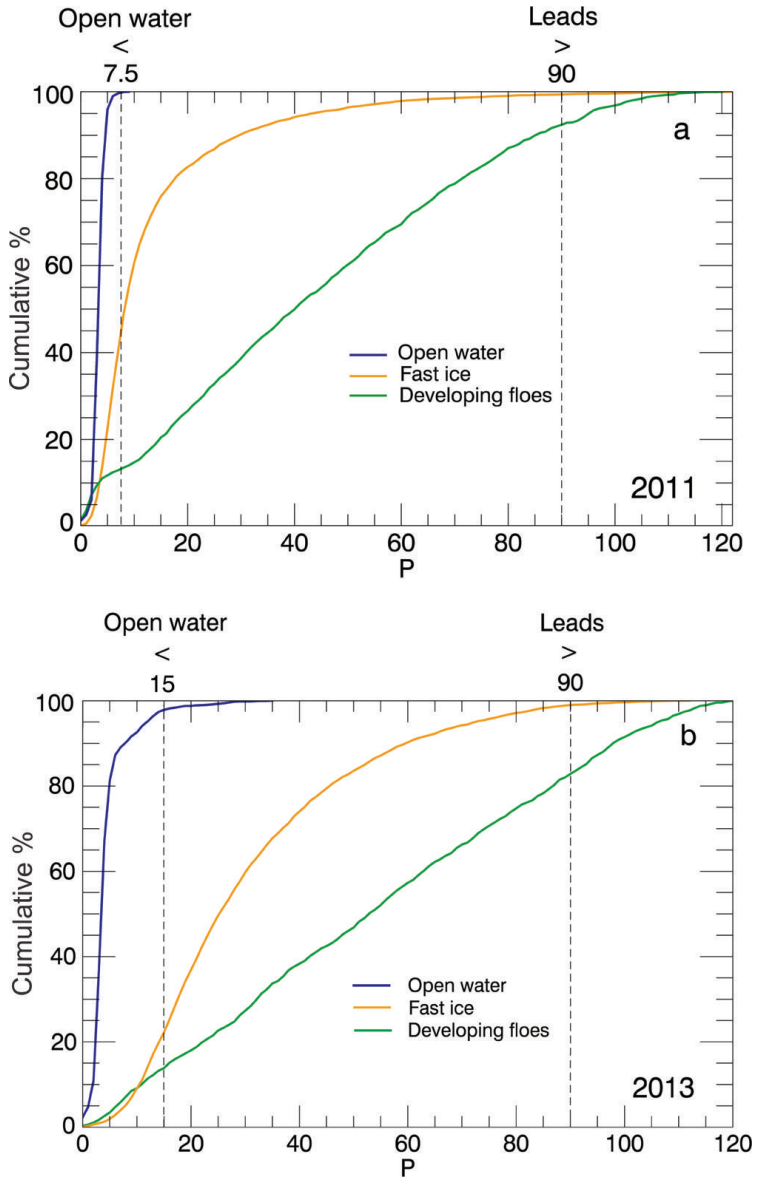

Figure 5.7. Surface type discrimination as indicated by Level 2 parameter peakiness (P) displayed as a cumulative percentage. Surface types, open water, fast ice and developing floes are displayed for 2011 (a) and 2013 (b). In 2011, surface conditions made the discrimination of open water and fast ice more difficult. This resulted in a change in the thresholds between the years. The expected inclusion of sea ice in the open-water surface type is indicated by the percentage overlaps.

open water. In both 2011 and 2013 the majority (>95 %) of P values were <15. However, in 2011 the surface types open water and fast ice overlapped, whereas in 2013 a clear separation is achievable (Fig. 5.7). This is a result of fast-ice surface conditions differing in 2011 that lowered values in the P distribution. We are unable to fully establish the cause of this change. The pulse shape and, thus, P are largely determined by variation

of backscatter with incidence angle (Wingham et al., 2006). This is related to RR, and, given the differing conditions over the fast ice between the two years, a change in RR at the dominant backscattering surface was likely the cause. In 2013 it is possible to clearly differentiate and establish open water as $P < 15$ and fast ice as $15 < P < 90$. In 2011 we lowered the threshold for open water to $P < 7.5$ to reduce the amount of fast ice potentially included in the expected open-water retrievals. 2011 fast ice is therefore given thresholds of $5 < P < 90$. We appreciate these thresholds for open water and fast ice overlap, but if a higher bound is taken for the lower limit of P for fast ice in 2011, ∼60 % of height retrievals identified as fast ice will be discarded. The fast-ice P distributions were established from assessment of the fast-ice area. The sea-ice growth season in McMurdo Sound begins in March, but fast ice does not become fully established for some time. We are confident that fast ice is fully established by August and derive a P value for this surface type by masking fast-ice area from August to December. We assume the fast-ice area is also representative of P values for ice floes in McMurdo Sound. Finally, due to the discussed overlaps of open water and fast ice (Fig. 5.7), and potential inclusion of sea ice in expected open-water retrievals, it is necessary to filter H values with regard to their heights. This approach is altered for each year to account for the expected inclusion of ice in the open-water retrievals (Fig. 5.7; 40 % in 2011 and 20 % in 2013). We calculate the means of the lowest 60 % of H values in 2011 and 80 % in 2013 that meet the open-water and lead criteria and establish $\mathrm{SSH_{auto}}$ for each track from this.

5.5.2 *WfF* automatic SSH identification

We attain $\mathrm{SSH_{auto}}$ by using a similar parameter to ESA Level 2 P, the pulse peakiness (PP) as described by Armitage and Davidson (2014). The assigned values for the discrimination of each surface type were chosen after comparison of PP values over surface types in the study area using the same method as described for $ESAL2$ in Section 5.5.1. We flag leads as PP > 0.30 and open water as PP < 0.05. Sea ice is classified as $0.08 <$ PP < 0.30. Overlaps of sea-ice and open-water surface types were noted as in Section 5.5.1. To remove this height bias from inclusion of sea ice, we establish $\mathrm{SSH_{auto}}$ from the mean of the lowest 60 % and 80 % of elevations flagged as leads of open water in 2011 and 2013 respectively. Phase information is also used in this product in the same manner as $ESAL2$. We again remove elevation outliers with application of a vertical threshold of ± 2 standard deviations of the mean to the track.

Table 5.2. Mean automatic procedure freeboard values and standard deviations derived by each technique for each year for the entire study area and fast ice only (bold). The total number of measurements (n) for each year is also displayed. The spatial distribution of the satellite tracks from which the Fb_{auto} means are derived are shown in orange in Fig. 5.3.

Retracker	2011 (m)	2013 (m)
$ESAL2$ Fb_{auto}	0.09 ± 0.25	0.08 ± 0.24
	0.11 ± 0.27	**0.09 ± 0.26**
	(n = 16611)	(n = 12884)
WfF Fb_{auto}	0.12 ± 0.24	0.10 ± 0.23
	0.11 ± 0.25	**0.10 ± 0.22**
	(n = 7094)	(n = 9439)
$TFMRA40$ Fb_{auto}	0.16 ± 0.35	0.11 ± 0.38
	0.23 ± 0.36	**0.15 ±0.46**
	(n = 7532)	(n = 8244)

5.5.3 *TFMRA40* automatic SSH identification

We use the algorithm described in Ricker et al. (2014a) but amend the procedure, as surface conditions differ in the investigation area from those for which the technique has previously been applied. As mentioned in Section 5.3.4 we maintain the inclusion of the additional surface type, polynya, and its amended 60 % retracking threshold. The elevations retrieved for both leads and polynyas in close proximity should be of the same mean value to construct a consistent SSH_{auto}. We compared the elevations of detected leads that were in close proximity to the polynya surface type for several CS-2 tracks and found sufficient agreement using a 60 % and 40 % threshold for each surface type in conjunction. Track sections with a significantly inaccurate SSH_{auto}, as a consequence of sparse lead/open-water coverage, have been discarded.

5.5.4 Automatic results

The application of the three retracking techniques produced Fb_{auto} datasets for McMurdo Sound for 2011 and 2013 (Table 5.2). All techniques show a decrease in freeboard in McMurdo Sound from 2011 to 2013 over the study area as a whole, and the fast-ice area when assessed alone. The magnitude of this change varies between methods. $ESAL2$ and $TFMRA40$ both identify the fast-ice area as having a higher freeboard than the mean of the entire study area. WfF does not show such a relationship, with fast-ice mean Fb_{auto} being 0.01 m lower in 2011 and the same value in 2013. A lower mean freeboard is expected for the entire study area, as sea ice in the dynamic MSP area is

included. Sea ice in this area is expected to be thinner than the fast ice that has undergone near-continuous and stable growth over winter. This discrepancy may be driven by the identified problems with surface type discrimination. Open-water areas may have been erroneously included as sea ice, lowering the Fb_{auto} averages. Clearly apparent are the large standard deviations of the CS-2 data (Table 5.2).

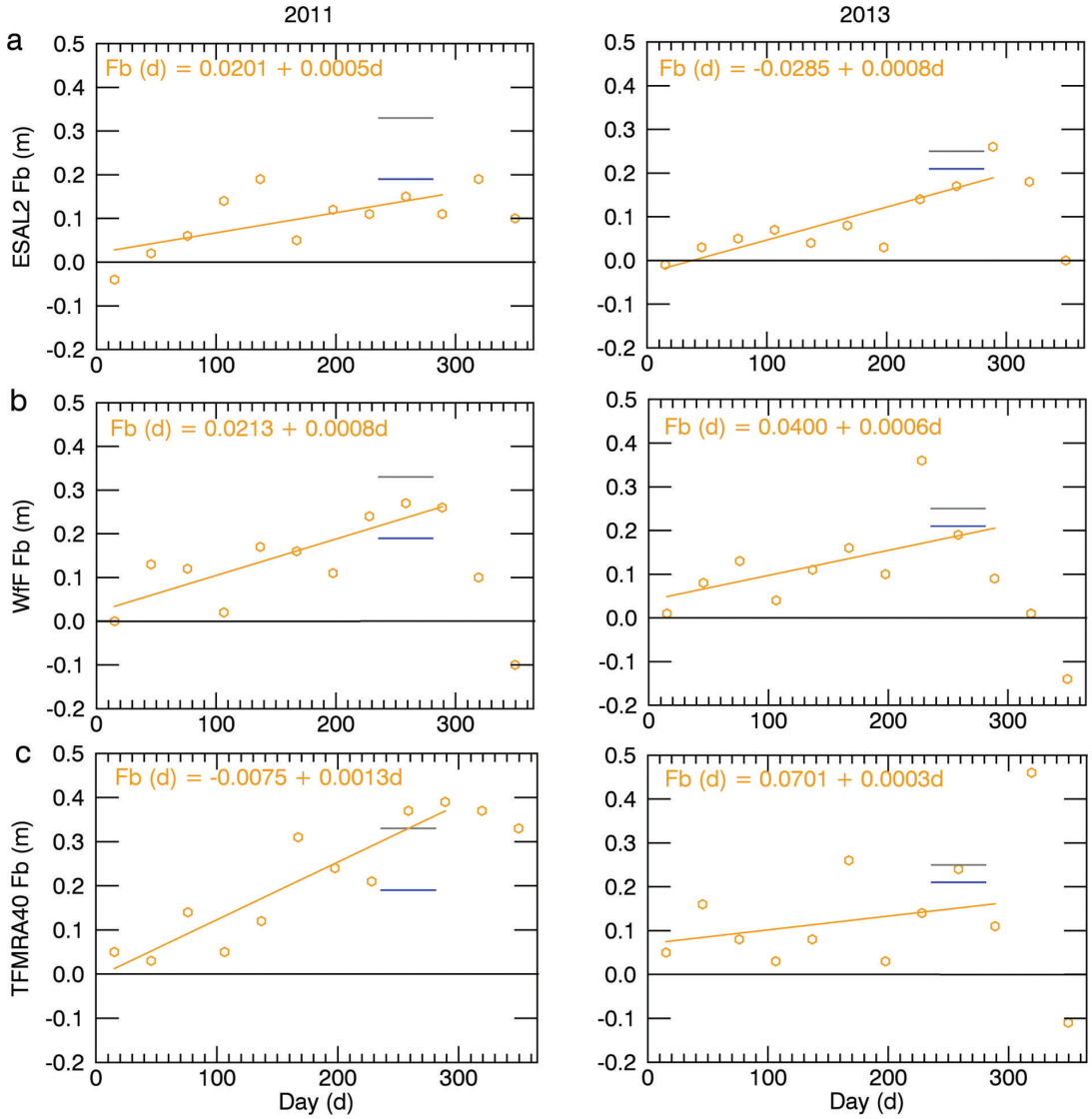

Figure 5.8. The development of the McMurdo Sound fast-ice cover from mean automatic procedure freeboard values for each month for 2011 and 2013 over the expected sea-ice growth period (day zero = 1 March) for $ESAL2$ (a), WfF (b) and $TFMRA40$ (c). A linear fit from the beginning of mid-March (∼day 15) to mid-December (∼day 290) defines the expected sea-ice growth period. Mean in situ measured ice and snow freeboards measured in November/December of each year are shown by the blue and grey lines respectively. The standard deviations for each mean value are provided in Table 5.3.

To investigate the ability of CS-2 further and to minimize the influence of the MSP sea-ice

area, we assess the fast-ice area with regard to its seasonal development. The FY fast-ice regime in McMurdo Sound typically breaks out in February, and often in one of every two years (Heine, 1963) leaves McMurdo Sound nearly entirely ice-free. Sea ice begins to form in March when air temperatures are low enough to initiate freezing as indicated by field studies (Purdie et al., 2006; Leonard et al., 2006) and MODIS imagery. This was also the case in 2011 and 2013. The sea ice develops into a fast-ice cover in a coastal band (Fig. 5.3) around McMurdo Sound, with fast-ice establishment intermittently interrupted by storm events (as indicated by optical and SAR imagery). Sea-ice growth continues until about mid-December (Jeffries et al., 1993). We use the region of McMurdo Sound that is covered by fast ice at the end of the growth season as a mask for the entire year. We expect to observe a signal in the recorded Fb_{auto} datasets indicative of increasing freeboard from March to December. Such findings are displayed in Fig. 5.8, where we clearly see this development using all three retracking techniques. Fb_{auto} increases through autumn and winter toward Fb_i and Fb_s in situ measurements in spring. We apply a linear trend from the beginning of March to mid-December to capture the sea-ice growth measured by Fb_{auto}. Using this trend to compare Fb_{auto} results in mid-November (∼day 260 in Fig. 5.8) to the mean of all in situ measurements in each year, we find ESAL2 Fb_{auto} underestimates Fbi in both years by 0.04 m. In 2011 WfF Fb_{auto} overestimates in situ measured sea-ice freeboard by 0.08 m and in 2013 underestimates it by 0.02 m. TFMRA40 provides a mean Fb_{auto} value of 0.37 ± 0.22 m in 2011, 0.04 m lower than Fb_s. In 2013 TFMRA40 Fb_{auto} underestimates Fb_s by 0.01 m. All techniques also display a decrease in Fb_{auto} after reaching their respective maximums in line with the observed breakout of the fast-ice area in late February/early March of each year. Mean values and standard deviations for each month are displayed in Table 5.3. We are able to evaluate the performance of the automatic procedures by comparison of the CS-2 mean Fb_{sup} over the validation line (Fig. 5.4) against the Fb_{auto} mean over the same track. With the application of a correction for c in snow, Fb_{auto} overestimates Fb_{sup} by 0.07, 0.05 and 0.01 m for ESAL2, WfF and TFMRA40 respectively. The overestimation of freeboard by Fb_{auto} for ESAL2 and WfF is driven by the auto applied along-track filtering of H. The filtering assumes a percentage inclusion (20 % for 2013) of sea ice within the total sampled area over water along each track. In this case, the open-water area to the north has an ice concentration of zero and therefore SSH_{auto} is established too low, and subsequent Fb_{auto} is too high. This simple comparison showcases the additional error which can be expected by applying fully automatic methods for the identification of SSH which only generalize expected open-water availability.

Table 5.3. Mean automatic procedure freeboard values (m), standard deviations and number of measurements (in parentheses) used to derive the statistics for each technique in each year over the fast-ice area. The data are binned into calendar months. The day corresponding approximately to the middle of each calendar month from the start of the analysis (day zero = 1 March) is also displayed.

Month	2011 (m)			2013 (m)		
	$ESAL2$	WfF	$TFMRA40$	$ESAL2$	WfF	$TFMRA40$
MAR (+15.2)	-0.04 ± 0.16 (494)	0.00 ± 0.35 (232)	0.05 ± 0.29 (105)	-0.01 ± 0.30 (394)	0.01 ± 0.21 (260)	0.05 ± 0.19 (271)
APR (+45.6)	0.02 ± 0.24 (560)	0.13 ± 0.18 (400)	0.03 ± 0.15 (317)	0.03 ± 0.12 (480)	0.08 ± 0.15 (488)	0.16 ± 0.43 (362)
MAY (+76)	0.06 ± 0.14 (537)	0.12 ± 0.16 (296)	0.14 ± 0.38 (526)	0.05 ± 0.26 (623)	0.13 ± 0.15 (508)	0.08 ± 0.19 (238)
JUN (+106.4)	0.14 ± 0.31 (400)	0.02 ± 0.30 (246)	0.05 ± 0.22 (204)	0.07 ± 0.24 (543)	0.04 ± 0.21 (409)	0.03 ± 0.19 (267)
JUL (+136.8)	0.19 ± 0.25 (859)	0.17 ± 0.18 (395)	0.12 ± 0.12 (221)	0.04 ± 0.22 (732)	0.11 ± 0.17 (531)	0.08 ± 0.32 (266)
AUG (+167.2)	0.05 ± 0.23 (838)	0.16 ± 0.17 (165)	0.31 ± 0.35 (443)	0.08 ± 0.16 (604)	0.16 ± 0.13 (486)	0.26 ± 0.41 (588)
SEP (+197.6)	0.12 ± 0.25 (952)	0.11 ± 0.26 (199)	0.24 ± 0.22 (703)	0.03 ± 0.28 (647)	0.10 ± 0.21 (499)	0.03 ± 0.23 (241)
OCT (+228)	0.11 ± 0.22 (786)	0.24 ± 0.19 (102)	0.21 ± 0.39 (341)	0.14 ± 0.14 (208)	0.36 ± 0.14 (159)	0.14 ± 0.19 (199)
NOV (+258.4)	0.15 ± 0.20 (725)	0.27 ± 0.24 (121)	0.37 ± 0.22 (196)	0.17 ± 0.18 (602)	0.19 ± 0.18 (286)	0.24 ± 0.26 (255)
DEC (+288.8)	0.11 ± 0.29 (847)	0.26 ± 0.21 (136)	0.39 ± 0.43 (527)	0.26 ± 0.34 (910)	0.09 ± 0.26 (705)	0.11 ± 0.35 (453)
JAN (+319.2)	0.19 ± 0.35 (643)	0.10 ± 0.30 (161)	0.37 ± 0.45 (407)	0.18 ± 0.22 (313)	0.01 ± 0.31 (228)	0.46 ± 0.72 (516)
FEB (+349.6)	0.10 ± 0.44 (340)	-0.10 ± 0.18 (119)	0.33 ± 0.70 (72)	0.00 ± 0.34 (325)	-0.14 ± 0.20 (216)	-0.11 ± 0.62 (455)

5.6 Discussion

We have evaluated the performance of two retracking techniques currently presented in the literature: WfF (Kurtz et al., 2014) and $TFMRA40$ (Ricker et al., 2014b). The first assumes the surface is retracked at $\mathrm{Fb_i}$ and the second near $\mathrm{Fb_s}$. We also use $ESAL2$, a product for which we have limited information about its retracking procedure and assumptions therein. Here we discuss the extent to which our in situ observations support the assumptions in view of the mean and standard errors of the measured $\mathrm{Fb_{sup}}$

and Fb_{auto} datasets and information provided by the waveform responses to surface conditions.

As expected, the best agreement is found between in situ measurements and CS-2 freeboard retrieval techniques for $ESAL2$, WfF and $TFMRA40$ using a supervised SSH identification with the exception of WfF in 2011. For the latter, we attribute the anomalously high freeboard to two sources. The first is a low SSH estimate due to the reduced ability of the technique to establish SSH in the presence of differing surface types over a small segment of the SSH reference area. Secondly the introduction of a positive freeboard bias is noted which is forced by a smoother, thicker and morphologically more complex snow cover in 2011. These findings are supportive of other studies (Kwok, 2014; Kurtz et al., 2014) which also show that snow can introduce a positive elevation bias due to an increase in power returned from above the snow/ice interface. We also observe a higher Fb_{sup} for $ESAL2$ in 2011 when compared to 2013, and suggest a similar response to the change in snow properties has influenced the retrieval. Our observations show that the snow in the study area has higher mean densities and exhibits distinct layers with varying hardness, density and crystal size, as compared with the simplified assumptions in Kurtz et al. (2014). It is speculated that in combination with the larger grain size and higher salinity near the snow/ ice interface, the effective point of scattering is shifted even further away from the ice surface. The only way to quantify what impact the snow cover had on the retrieved freeboards would be to know the backscatter coefficients of the snow and ice. Lacking this information we are limited to more qualitative statements based on comparisons to in situ information. Our ability to convey qualitative information on the waveform interaction at the surface, as suggested in Section 5.4, is also restricted. In the presence of a snow cover that is fully transparent to the incident Ku-band radar energy, no bias is expected to be observed for retracking procedures. Attaining knowledge of the dominant backscattering surface is crucial to undertake any meaningful time-series assessment of sea-ice freeboard, permitting thickness estimation. Therefore the role of the heterogeneity of the snow cover on CS-2 freeboard retrieval requires further observational study.

Although we observe the influence of the snow cover in the freeboard retrieval, we are unable to fully quantify the error in the SSH identification, even under the supervised assessment. Experiments in which the influence of SSH misidentification is isolated will need to be carried out to completely quantify the positive bias introduced by a snow cover using WfF. In addition, the use of automatic SSH identification procedures can be expected to increase freeboard errors. Direct comparisons between supervised and automatic procedures suggest differences in excess of 0.05 m.

It was not possible to determine the accuracy of the established SSH_{sup}, and we can only evaluate the resulting freeboards. The SSH_{sup} of all three data products was independently

assessed without tuning to in situ measured freeboards. However, the characteristics of the study area made it necessary to modify the processing methods for sea surface identification currently used in the Arctic (Kurtz et al., 2014; Ricker et al., 2014a). The surface type polynya was added to the surface classification for $TFMRA40$ to improve ice-water discrimination. This surface type produces similar waveforms to sea ice, but more diffuse, with a leading edge that is typically flatter. The power threshold for retracking over this surface type was increased to 60 %. The fact that larger open-water areas can result in significantly different SSH estimates may introduce a significant inter-retracker difference in SSH establishment due to the inconsistent change along the leading edge. Future improvement of the WfF technique over varying surface types in close proximity (i.e. leads, open water, sea-ice floes within a few hundred meters) is required. These conditions cause noisy waveforms, and improvement of our understanding of the influence of this noise on the retracking procedure is a current research focus. It seems that the more sophisticated approach of WfF is more sensitive to these conditions than $TFMRA40$, and a more stringent data discard procedure may need to be adopted to reject such waveforms. Further, using automatic surface discrimination algorithms resulted in insufficient separation of sea-ice and water surface types. It may be of benefit to adopt procedures that account for the seasonal change in sea-ice/snow surface conditions which force alteration of surface discriminatory parameters (e.g. P, PP, SSD). This may improve the separation of surface types and $\mathrm{Fb_{auto}}$ results, both in this investigation area and when larger regions are considered for assessment.

With the aid of information gained in the supervised freeboard retrieval procedure, we were able to place in context and develop automatic freeboard retrieval procedures for each technique. Our results have shown the ability of CS-2 to record the development of a fast-ice cover in the Antarctic. Although our supervised analysis provides insight into the surface that is tracked with respect to $\mathrm{Fb_s}$ and $\mathrm{Fb_i}$ we do not have the confidence to estimate sea-ice thickness with an acceptable error margin. However, we do find the growth rate as recorded by $\mathrm{Fb_{auto}}$ over both years for all techniques, of 0.7 mm $\mathrm{d^{-1}}$ (mean of all rates displayed in Fig. 5.8), is in agreement with other studies of ice growth rates in McMurdo Sound(Gough et al., 2012; Purdie et al., 2006). By April, all retracking techniques identify positive freeboard values. Although we identify the onset and the trend in freeboard growth, we note that standard deviations of $\mathrm{Fb_{auto}}$ are typically twice that found over this area when it was assessed using ICESat from 2003 to 2009 (Price et al., 2013). There was an extensive multiyear sea-ice cover in McMurdo Sound from 2003 to 2009. However, we are not aware of any changes to the FY sea-ice surface conditions between the two satellite observation periods that could be responsible for the observed differences in standard deviations, although the CS-2 assessment area is smaller. Therefore, it is appropriate to look to instrumental and methodological sources to explain the observed noise. Findings from CS-2 presented here were attained using

SIN mode which acquires data at a reduced (by a factor of four) burst repetition interval compared to SAR mode which is used over the majority of the Antarctic sea-ice pack. The ability to average and reduce measurement noise in the SIN mask which occupies the entire coastal Antarctic, a key area of sea-ice production, is therefore reduced. Assuming normally distributed noise, the values for the standard deviations would reduce by a factor of two if data were acquired in SAR mode. Even with this restriction, there is no evidence that SIN mode is inadequate for sea-ice freeboard retrieval. Other studies (Armitage and Davidson, 2014) provide evidence in support of its usage, as SIN mode provides phase information which can be used to reduce the impact of snagging on height retrievals. This ability is beneficial, as a less stringent data discard is required to remove off-nadir range estimates which exhibit a positive range bias and subsequently height retrievals that are too low. The standard deviations of $\mathrm{Fb}_{\mathrm{auto}}$ using $TFMRA40$ are higher than those from the other two procedures, perhaps an indication of the noise introduced from the range bias as a result of omitting phase information. An additional source of scatter and an increased standard deviation could be introduced to the $TFMRA40$ procedure, as the slope of the leading edge at the tracking point is typically shallower in comparison to higher thresholds. This could force a higher noise if waveforms change significantly from one measurement to the next. The noise in $TFMRA40$ heights could also indicate that undulations or roughness of the snow surface was often higher than the ice surface beneath. These factors do not seem to have been influential along the validation line (Fig. 5.4), where $TFMRA40$ produced the least noisy $\mathrm{Fb}_{\mathrm{sup}}$ dataset of the three techniques.

The surface height that is tracked is dependent upon where on the leading edge each processor establishes its retracking point, which is selected on the basis of the assumed dominant backscattering interface (e.g. retracking at 40 %, 40-70 % or 50-90 %). This is a trivial consideration and, in the absence of any alteration of the waveform by surface conditions, these simple differences in range would cause the resultant differences in measured freeboard. Our results show that in McMurdo Sound using the supervised analysis in an optimal scenario, when there is a thin and homogeneous snow cover (mean = 0.05m), TFMRA40 approximates $\mathrm{F_s}$ well, WfF approximates $\mathrm{F_i}$ well, and $ESAL2$ identifies a horizon in between $\mathrm{F_i}$ and $\mathrm{F_s}$. Although we have identified that GR, RR and snow are influential on the leading edge, we cannot separate their influence with any certainty. It is evident from interpretation of the leading edge alone that no separation of the air/snow interface and ice/snow interface is directly achievable, which is expected due to the range resolution of CS-2 (Kwok, 2014; Kurtz et al., 2014; Bouzinac, 2012; Wingham et al., 2006). However, using a comparison between a snow-covered sea-ice area and an area with significantly less snow, the gradient of the leading edge becomes shallower and the width of the entire waveform is extended in the presence of snow. Based on the model assumptions of WfF, very small changes in the leading edge are expected

as a function of surface roughness, and insufficiencies in the fit of the leading edge as shown in Fig. 5.6b indicate a higher than expected influence of roughness and snow cover on the leading edge. This will alter the retracking position on the leading edge for every retracker in a different way. It is therefore reasonable to conclude that not only the trivial relationship of different retracking points is responsible for the observed differences in freeboards between methods, but variations in surface properties were also influential. Further work is required to separate and quantify these influences.

Relating our findings to the development of larger-scale Antarctic assessments outside the coastal band is hindered by the nature of our study area compared to the majority of the Antarctic sea-ice pack. However, the dynamic sea-ice area in the MSP is more representative of the wider Antarctic sea-ice zone. Although this area was not the focus of our assessment, automatic freeboard retrieval procedures which included this area have produced freeboards that are considered reasonable for Antarctic pack ice, i.e. 0.08-0.16 m (Table 5.2). We have identified certain issues within our analysis which are applicable at the larger scale which must be addressed in order to develop techniques. Given the abundance of large open-water areas in the Antarctic sea-ice zone which do not exhibit the typical 'peaky' response from leads, it is necessary to characterize them. If they are large enough and their sea-ice concentration is low, they can be masked using auxiliary satellite information. However, in regions of high ice concentration where leads are too large to be discernible from radar information, ice-water discrimination may be hindered. At what size a lead becomes too large to exhibit a typical waveform would need to be ascertained to conclude whether open-water areas may be an issue in the Antarctic sea-ice pack. The spatial and temporal heterogeneity of the snow cover, even in our small study area, highlights the challenge presented for freeboard retrieval algorithms to assess larger areas in the Antarctic. Further advances in retracking techniques guided by in situ validation will need to be made in order to attain freeboard measurements with improved accuracy. Further complications will be introduced by snow loading which typically suppresses sea-ice freeboard, resulting in a close to zero ice freeboard condition in the Antarctic sea-ice pack. This issue may be addressed using a combination of different retracking procedures that attempt to identify the air/snow interface as shown to be successful here. In any case, it is clear that data treatment may need to be altered for different regions, in particular retracker algorithms to cater for the variability of the Antarctic sea-ice regime.

5.7 Conclusion

Our in situ freeboard measurements reveal that retracking techniques based on the fitting of waveforms ($ESAL2$ and WfF) and a threshold retracker ($TFMRA40$) can be used to

derive freeboard estimates over Antarctic fast ice from CS-2. Although we find that the retrievals capture freeboard heights, the variability is expected to be high as indicated by the large standard deviations of mean freeboard values. In the validation area of McMurdo Sound, which harbors homogeneous fast ice, the results of the three separate techniques used for freeboard retrieval fall within the margins of expected freeboards as indicated by in situ measurements in austral spring 2011 and 2013. Mean freeboard values from 4ESAL24 are representative of a horizon between the air/snow and snow/ice interface. A smooth snow cover with multiple layers causes a bias of +0.14 m away from the ice freeboard using WfF. It should be noted that we are unable to identify any contribution from an inaccurate sea surface height establishment upon this bias. In the absence of such a snow cover, WfF-derived freeboards are 0.04 m lower than in situ measured ice freeboard. $TFMRA40$ produces mean freeboards 0.03 m higher than in situ measured snow freeboard. We observe higher standard deviations in automatic retrieval procedures, which could be reduced by spatial averaging if data at a higher sampling rate (e.g. in SAR mode) were available. Difficulties in the identification of sea surface height were noted for $TFMRA40$ over larger open-water areas and for WfF over areas inclusive of multiple surface types (e.g. leads, sea ice and open water) within the radar footprint. Automatic algorithms were tested through 2011 and 2013 and recorded the growth of the FY fast-ice cover in McMurdo Sound. The CS-2 trends recorded from each method of 0.7 mm d^{-1} are in line with sea-ice growth rates measured in situ in the region. Automatic surface type discrimination procedures may benefit from adjustments to account for spatial and temporal variations in snow/ice surface conditions, which could improve ice-water discrimination. In situ validation in the Antarctic pack ice is a fundamental component for the development of CS-2 freeboard retrieval techniques. The uncertainty of CS-2 freeboard datasets is expected to be improved over larger spatial scales than assessed here. We see our results as encouraging in this context, as expansion of spatial scales and further development of retracking techniques will likely improve Antarctic CS-2 freeboard products.

5.8 Acknowledgements

We thank all participants in the 2011 and 2013 Antarctica New Zealand field event K063 as well as Scott Base staff for their support. CS-2 data were provided by the European Space Agency for project AOCRY2CAL-4512. The TerraSAR-X image was provided through DLR (German Aerospace Center) project OCE1592. The work of V. Helm and S. Hendricks was funded by the German Ministry of Economics and Technology (grant 50EE1008). We appreciate the efforts of Alec Casey who provided technical assistance in data processing. A research stay for the first author at the University of Alberta was

supported by Air New Zealand. Further research support was provided by the National Institute of Water and Atmospheric Research, New Zealand, under contract CO1X1226. We thank Trimble NZ for the use of GNSS equipment, and Wolfgang Dierking for fruitful discussions. We are very grateful for the contributions of Nick Key and Justin Harrison in the design and preparation of field equipment. The comments of two anonymous reviewers and the sea-ice editor contributed to the manuscript. This work was collated at Gateway Antarctica, University of Canterbury, New Zealand.

Chapter 6

Preliminary results and outlook

Retrieving sea-ice freeboard and thickness from CryoSat-2 data is an ongoing process. This thesis focussed on uncertainties of the CryoSat-2 product for selected time periods. We aim to improve CryoSat-2 freeboard and thickness estimates in the future along with the prediction of trends in ice-volume time series. This also depends on the availability of better snow depth products. On the *Meereisportal* webpage `http://www.meereisportal.de/cryosat` first pre-operational products are already provided. Besides sea-ice freeboard and thickness, they contain auxiliary information, e.g. the distribution of leads as well as the sea-surface height. The availability of these parameters is yet unmatched in the Polar Climate Research community and we hope to stimulate other fields such as oceanography to use these data. Furthermore sea-ice thickness retrievals can be used for assimilation in model studies like Kauker et al. (2009) to provide a more realistic state of sea-ice thickness. However, some key fields of future work are addressed in the following sections.

6.1 Volume time series and combination with other satellite sea-ice thickness data

In Ricker et al. (2014b) we estimated the Arctic sea-ice volume with an initial sea-ice thickness retrieval algorithm. We filled the CryoSat-2 data gap above 88°N by linear interpolation and applied the same data mask as shown in Figure 3.5. By using the EASE 2.0 grid featuring an equal area projection, the monthly mean sea-ice volume V can be estimated as:

$$V = \sum_{j=1}^{M} c_j \cdot A \cdot \bar{T}_j \tag{6.1}$$

with the area A (625 km^2) of a 25 x 25 km grid cell, the sea-ice concentration c_j and the monthly mean thickness $\bar{T}_\mathrm{j}$ of grid cell j, added up over the total number

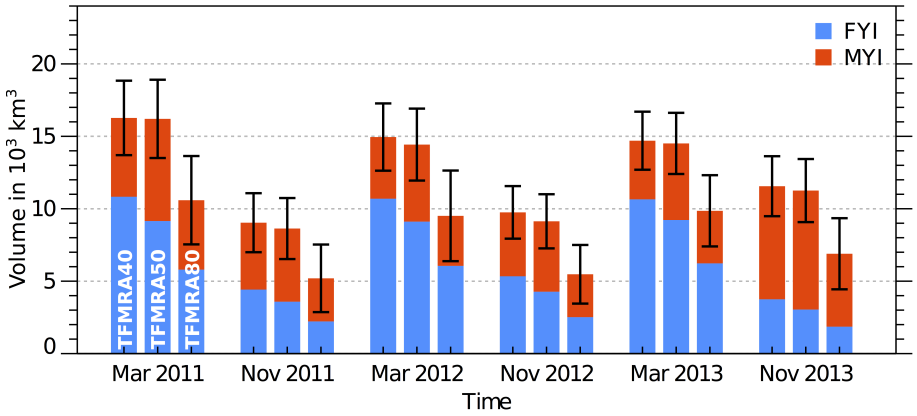

Figure 6.1. Arctic sea-ice volume estimates of March and November 2011-2013 by applying TFMRA retracker thresholds 40 % (TFMRA40), 50 % (TFMRA50) and 80 % (TFMRA80) of the waveform's first maximum peak power, separated between first-year (FYI) and multiyear ice (MYI). Credit: Ricker et al. (2014b).

M of grid cells. The sea-ice concentration c is adapted from OSI SAF (Eastwood, 2012).

We find declines of -9.7 % (TFMRA40), -10.9 % (TFMRA50) and -6.9 % (TFMRA80) from March 2011 to 2013 (Figure 6.1). In contrast, we find volume increases of 27.88 % (TFMRA40), 25.71 % (TFMRA50) and 32.65 % (TFMRA80) from November 2011 to 2013. The rise in November 2013 can be associated with a cold summer in 2013 and hence more young ice in November on the one hand, but also with the positive freeboard bias due to snow accumulation on the other hand (see Chapter 4). The uncertainty of the absolute volume is dominated by the choice of the retracker threshold. However, the main trends remain, regardless which threshold is used. Residual uncertainties, represented as black error bars in Figure 6.1 are still in the range of $\pm$ 2500 km^3. Thus, volume trends are smaller than current uncertainty ranges.

In order to improve uncertainty levels of long-term trends in sea-ice volume, the combination of data sets from subsequent satellite altimetry missions may be helpful. The challenge is to establish a consistent data set which considers the diverse spatial and range resolutions but also their different methodical approaches and limitations. Whereas ICESat, which carried a laser altimeter, provides estimates of the snow freeboard, radar altimeter satellites such as CryoSat-2 or Envisat deliver radar freeboard (see Chapter 3).

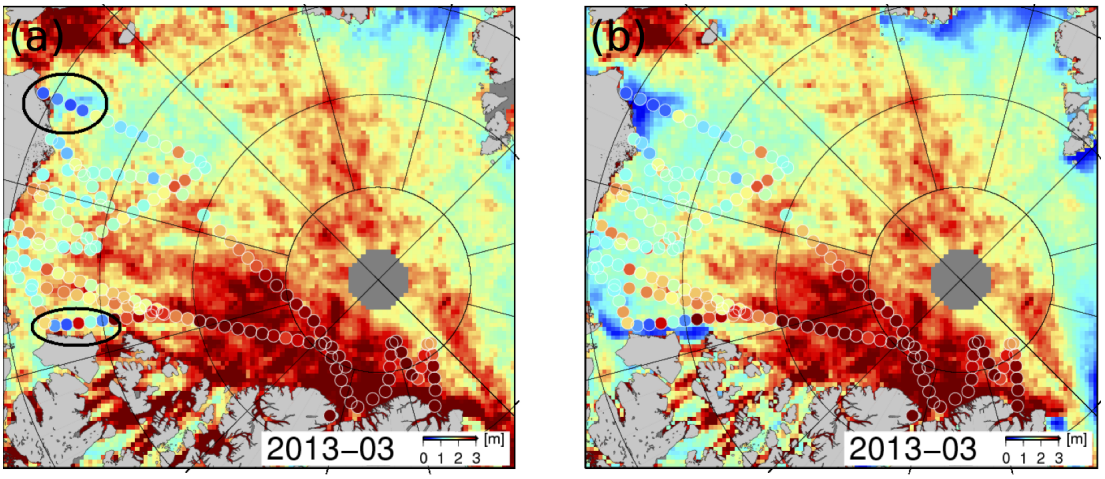

Figure 6.2. March 2013 Arctic mean-thickness retrievals from (a) CryoSat-2 and (b) a joint product from CryoSat-2 and SMOS. Colored circles show sea-ice thickness from NASA's Operation IceBridge in March 2013. The black ellipses represent areas of thin ice, where also IceBridge validation measurements are available. Credit: Kaleschke and Ricker (2012).

6.2 Radar altimetry/passive microwave synergy

As CryoSat-2, SMOS is part of ESA's Living Planet Program. It was launched in 2009 and provides brightness temperature observations at L-band, which are used to deliver sea-surface salinity. The thickness-dependency of brightness temperature enables to estimate the sea-ice thickness for thin ice regimes, in particular during the freeze up (Kaleschke et al., 2012; Huntemann et al., 2014). On the other hand, the primary goal of the CryoSat-2 mission is the determination of trends in perennial Arctic sea-ice thickness. Its relative uncertainty over thin ice (thickness $\leq$ 0.6 m) is particularly high and in the range of 100 % (see Chapter 3). Together with an additional snow depth retrieval by SMOS (Maaß et al., 2013), a merged sea-ice product of CryoSat-2 and SMOS observations has the capability to allow for thickness estimates, that are of higher accuracy than each single product. First results show that combining CryoSat-2 and SMOS ice thickness by applying a weighted average leads to significant improvements in thin ice regimes if compared to Operation IceBridge validation measurements (Figure 6.2). However, advanced data fusion methods like *Optimal Interpolation* (see next Section) will be considered within the framework of the SMOS+ Sea-Ice project.

6.3 Interpolation techniques

Currently we block the individual CryoSat-2 retrievals on a 25 x 25 km grid by calculating monthly averages that are weighted by the individual uncertainties. Though this is a robust method of data analyzing, other interpolation techniques should be evaluated. At the same time an increase of the temporal resolution of Arctic wide retrievals would be beneficial, especially for a joint inversion with SMOS thickness estimates, which are provided on a daily basis. This goes along with a lower CryoSat-2 orbit coverage for such a period which makes it necessary to find an adequate interpolation method. One approach could be an *Optimal Interpolation* (OI). For each grid cell where a value shall be estimated, a number of adjoining measurement points is sampled. In the following a matrix of weights is calculated, depending on the individual uncertainties and their distance between each other as well as to the grid cell. Specifically we calculate a matrix of covariances of the grid cell with the data used for the estimation, and another covariance matrix of the data with each other. Moreover, a *background field* is applied as a 'first guess'. Here we can use the CryoSat-2 product of the previous month or week. The differences between the background field and the actual data, multiplied by the weights, are then added up. This value again added to the background grid cell yields the estimate of the actual grid cell. More detailed descriptions of OI can be found in Bretherton et al. (1976); McIntosh (1990); Wilkin et al. (2002). Fieguth et al. (1995) use a multiresolution OI for the analysis of TOPEX/POSEIDON satellite radar altimetry data, providing interpolated estimates of different spatial resolutions. These techniques can be adapted for the CryoSat-2 processing, including also estimates from other sources (e.g. SMOS).

6.4 Validation of Antarctic CryoSat-2 freeboard and thickness retrievals

So far only few CryoSat-2 validation campaigns over Antarctic sea ice took place to investigate the radar backscatter of the snow layer at K_u-band frequency. We want to extend the CryoSat-2 calibration/validation to Antarctic sea-ice to investigate the prospect of CryoSat-2 and how the complex Antarctic snow stratigraphy is affecting the sea-ice freeboard retrieval. There are only few bases that allow flight operations that early in season, where sea ice is still present. We have chosen the British Antarctic research station Rothera as the starting point for our sea-ice surveys in November 2013, carried out in the framework of the AMASIM (Airborne Measurements for Antarctic sea ice monitoring) project. This site allows us to access the sea ice on both sides of the Antarctic peninsula. Figure 6.3 shows the flight tracks of the two accomplished sea-ice

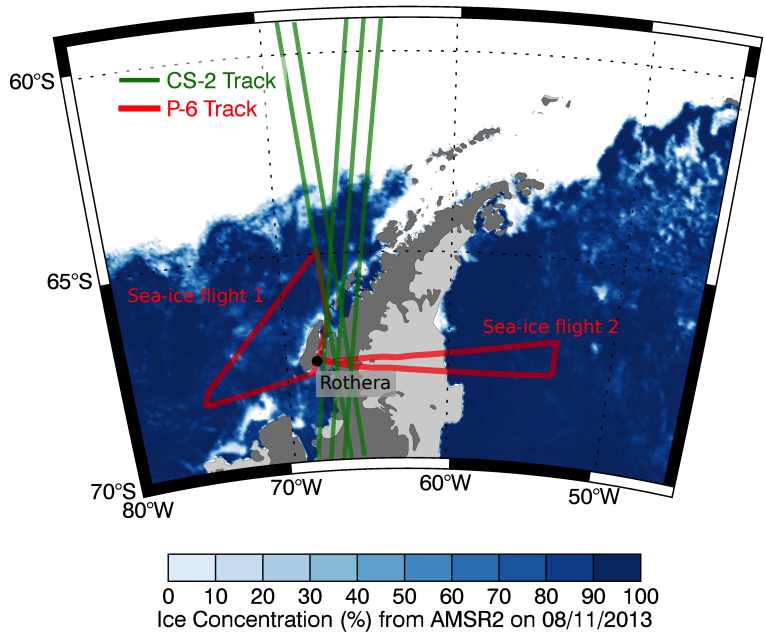

Figure 6.3. Accomplished sea-ice flights out of Rather, Antarctic Peninsula, during AMASIM 2013 together with CryoSat-2 ground tracks during 04/11/2013 and 10/11/2013. Source of sea-ice concentration: UHB-IUP (`http://www.iup.uni-bremen.de:8084/amsr2/regions-amsr2.php`).

surveys. The first took place over the Bellinghausen sea, the second over the Weddel sea. Besides other sensors, the AWI Polar-6 aircraft was equipped with a laser scanner and the ASIRAS radar altimeter (see Section 1.2.4). The analysis of these data will provide more information on the performance of K_u-band radar altimetry over Antarctic sea ice and scattering effects within the snow layer. It will complement findings of Willatt et al. (2010) and Chapter 5, so that in the future we may also estimate sea-ice freeboard and thickness of Antarctic sea ice with sufficient uncertainty estimates.

Chapter 7

Summary and concluding remarks

Sea-ice thickness has been required since decades by climate scientists, since it plays a key role for a large number of climate relevant processes. The knowledge of sea-ice thickness on a global scale allows us to evaluate the stability and variability of the global sea-ice cover, which is a sensitive indicator of climate change (Lemke et al., 2007; Kurtz et al., 2013). Unfortunately, sea-ice thickness cannot be observed directly from space. Satellite altimetry bases on range measurements and enables us to retrieve the sea-ice freeboard, the height of the sea ice above the sea level. By assuming hydrostatic equilibrium, satellite altimetry is the only technique capable of estimating the sea-ice thickness on a global scale and all thickness ranges. CryoSat-2 is the current radar altimeter mission that followed up the European Remote Sensing Satellites ERS-1 and ERS-2, the Environmental Satellite (Envisat) and the NASA's Ice, Cloud, and land Elevation Satellite (ICESat). CryoSat's onboard radar altimeter involves substantial improvements in spatial resolution and latitudinal coverage of up to 88°N.

The aim of this study was to assess CryoSat-2 freeboard and thickness retrievals, based on CryoSat-2 L1B waveforms, delivered by the European Space Agency (ESA). Therefore, we developed a processing chain and specifically described a waveform classification algorithm that is needed to distinguish between echoes of sea ice and leads, which are needed as tie points to construct the actual sea-surface height. The shape of the waveform characterizes where it is originated and we use shape-describing parameters to exclude waveforms that were biased by off-nadir leads.

A key role in interpreting CryoSat-2 retrievals over sea ice is given by the uncertainties that arise with each individual measurement, propagating to the monthly averages of sea-ice freeboard and thickness. A major contribution is the lack of knowledge about the exact retracking position at the leading edge of the waveforms to obtain the nadir range to the surface. In the CryoSat-2 scientific community different retracking algorithms and retracking thresholds are used to determine the distance to the main scattering horizon at the leading edge of the waveforms. But it is generally assumed that the major contribution

to the echo power originates at the snow/ice interface. We therefore conducted a sensitivity study to estimate the uncertainties that arise with the choice of the retracking threshold by applying thresholds of 40, 50 and 80 % of the first maximum peak power. Because of the limited range resolution of 0.47 m we are not able to distinguish between different backscatter contributors. Nevertheless, the application of all thresholds gives confidence that the freeboard retrieval represents the geographical distribution of sea-ice types. This was shown by direct comparisons with airborne laser altimetry on the local scale as well as with ASCAT backscatter data at basin scale. It is shown that changing the retracking threshold mostly affects the magnitude of the range retrieval, although we find differences between first- and multiyear ice. In Chapter 2 it is shown that multiyear ice waveforms feature a flatter leading edge than waveforms that originate from first-year ice which can be used to distinguish between both ice types.

We further evaluated the freeboard uncertainty budget for each individual measurement, but also for a gridded monthly product. Since knowledge about the covariances of the contributing variables is insufficient we separated into random and systematic (bias) uncertainties (see Figures 3.2, 3.10 and 3.11). Regarding the random uncertainties, the main driver of a geographical pattern is the density of CryoSat-2 ground tracks, which causes a latitude-dependent gradient. The magnitude of random uncertainties of the individual freeboard measurements are dominated by speckle noise and the density of leads along each CryoSat-2 ground track. With their absence, the uncertainty of the actual sea-surface height increases and hence the freeboard uncertainty. However, due to averaging, these uncertainties are reduced to a level of < 2 cm for the ice pack regions and < 5 cm for the marginal ice zones and land fast ice (e.g. Laptev Sea).

In contrast systematic freeboard uncertainties (biases) are not reduced due to averaging, although different components may have opposite effects and reduce the total bias. Regarding the gridded freeboard product we estimate 0.06 m (0.12 m) for first-year ice (multiyear ice) that arise from the choice of the retracking threshold. This bias is accompanied by systematic uncertainties due to scattering within the snow layer in conjunction with surface roughness effects. We acknowledge that scattering effects within the snow layer and surface roughness may also feature spatial variability, but their correlation length is expected to be higher than the size of a grid cell (25 x 25 km).

According to the sea-ice thickness, the random uncertainties are increased tenfold and show a similar geographical distribution (see Figure 3.12). Due to the usage of auxiliary products (e.g. snow depth, ice and snow densities and ice type) systematic uncertainties in the range between 0.01 and 0.2 m from each of this variables contribute to the thickness uncertainty budget (see Figure 3.13). Just as for the freeboard, the choice of the retracking threshold, accompanied by systematic uncertainties due to scattering within the snow

layer in conjunction with surface roughness effects, clearly dominate the current thickness uncertainty budget (0.6 m (1.2 m) for first-year ice (multiyear ice)). We conclude that the Warren snow climatology is not a sufficient representation of Arctic snow depth for the purpose of calculating CryoSat-2 freeboard and thickness estimates. Besides the fundamental changes of the Arctic ice cover during the last decades, the lack of information about inter-annual snow depth variability can highly bias the sea-ice freeboard and thickness estimates. We find a rise of 0.02 - 0.15 m of ice freeboard from March 2013 to November 2013 in the multiyear ice region north of Canada, that is likely caused by early snow accumulation in November, since thermodynamic ice growth is not to be expected during Arctic summer. A year-round linear-trend comparison between ice-mass balance buoy measurements from 2012 to 2014 and coincident CryoSat-2 freeboard retrievals showed that changes in CryoSat-2 freeboard correlate with those of the snow freeboard derived from the ice-mass balance buoy measurements, regardless of the used retracking threshold. Hence, snow accumulation can have a significant impact on CryoSat-2 range measurements and therefore on ice freeboard, thickness and volume estimates, though we cannot quantify the bias with the methods presented in this work. However, the assumption that the CryoSat-2 main scattering horizon is given by the snow-ice interface cannot be justified in regions with a thick snow layer and a potentially complex stratigraphy.

Finally we provided provisional freeboard and thickness estimates for the period 2011 – 2013 together with their uncertainties on the webpage `http://www.meereisportal.de/cryosat`. These datasets have been already used for other studies, for example to evaluate climate model simulations of Arctic sea-ice thickness (Stroeve et al., 2014) and for a report on altimeter sea-ice thickness errors within the Arctic Climate Change, Economy and Society (ACCESS) project (Doble, 2014).

In-situ measurements over Antarctic fast-ice in austral spring 2011 and 2013 at McMurdo Sound have been used to evaluate the performance of different retracking techniques based on the fitting of waveforms ($ESAL2$ and WfF) and our threshold retracker ($TFMRA40$). All three methods are capable to derive freeboard estimates over Antarctic fast ice from CryoSat-2. The $ESAL2$ freeboard retrieval is representative for an interface between the air/snow and snow/ice interface. The $TFMRA40$ freeboard shows a better agreement with the snow freeboard from in-situ measurements. In consistence with the findings in Chapter 4 the results of Chapter 5 indicate that also WfF, which tracks the main scattering horizon close to the peak power, is affected by the presence of a snow cover, causing a positive bias away from the ice freeboard. However, in the absence of snow, the WfF retrieval represents the ice freeboard. These findings are very promising in view of an Antarctic freeboard retrieval. One can speculate to estimate snow depth by

applying different retracking thresholds to track radar backscatter originating from both the air/snow and the snow/ice interface.

Arctic sea-ice volume estimates have been calculated in this study, but are subject to uncertainties of the thickness retrieval that lead to significant differences in magnitude between the different algorithm retrievals (see Chaper 6). With the promising approaches for retrieval improvements (Chaper 6) and a better snow product volume uncertainties may be reduced at such a rate that significant trends can be identified in the future.

List of Figures

1.1 Arctic sea-ice cover in Spring and autumn . . . 3
1.2 CryoSat-2 measurement principle over sea ice . . . 4
1.3 Exemplary images of leads and meltponds . . . 5
1.4 Pulse-limited and Delay Doppler/SAR radar altimeters . . . 6
1.5 Simulated CryoSat-2 beam stack over ocean . . . 7
1.6 Theoretical building of a Doppler/SAR waveform . . . 9
1.7 CryoSat-2 validation activities . . . 13

2.1 Scheme of CryoSat-2 measurements along track . . . 23
2.2 CryoSat-2 waveforms from different surface types . . . 24
2.3 CryoSat-2 mean radar freeboard from December 2013 . . . 27
2.4 Geolocated CryoSat-2 surface elevations and pulse peakiness . . . 30

3.1 Schematic diagram for CryoSat-2 measurements over sea ice . . . 36
3.2 Flowchart of the CryoSat-2 data processing algorithm . . . 37
3.3 CryoSat-2 waveforms for sea ice and leads . . . 39
3.4 Flowchart of the CryoSat-2 uncertainty budget . . . 43
3.5 CryoSat-2 ice-thickness data mask . . . 45
3.6 CryoSat-2 mean radar freeboard and ASCAT backscatter from April 2011 47
3.7 Airborne validation measurements . . . 49
3.8 Probability density functions for laser altimetry and CryoSat-2 retrievals . 50
3.9 Radar freeboard from different retracker thresholds . . . 51
3.10 Random freeboard uncertainties . . . 52
3.11 Range differences between different retracker thresholds . . . 53
3.12 CryoSat-2 Arctic sea-ice thickness from March and November 2013 . . . 54
3.13 Sea-ice thickness bias contributions . . . 55

4.1 Buoy tracks and CryoSat-2 Arctic modal freeboard differences . . . 68
4.2 Example of matched CryoSat-2 measurements in the vicinity of the buoy position . . . 69
4.3 Time-series of coincident CryoSat-2 and buoy freeboard . . . 70
4.4 Scatterplots of CryoSat-2 freeboard against IMB snow freeboard . . . 76

4.5 Operation IceBridge quick-look snow depths from Mar/Apr 2013 and 2014 77

5.1 Components relating to the interpretation of CryoSat-2 freeboard data . . 83
5.2 CryoSat-2 SIN mode waveform over snow covered sea ice in McMurdo Sound 84
5.3 Location of the study area 87
5.4 Comparison of each method along a validation line coincident with a CryoSat-2 overpass 95
5.5 Track segments overlaid upon a TerraSAR-X radar image 97
5.6 Mean waveform examples for sea ice with significant snow cover 98
5.7 Surface type discrimination as indicated by Level 2 parameter peakiness . 101
5.8 Development of the fast ice cover over the expected sea ice growth period 105

6.1 Arctic sea-ice volume of March and November 2011-2013 114
6.2 CryoSat-2 - SMOS joint sea-ice thickness product 115
6.3 Accomplished sea-ice flights during AMASIM 2013 116

List of Tables

1.1 SIRAL instrument characteristics 11

2.1 Waveform parameter and ice concentration thresholds 25
2.2 Left- and right-peakiness 28

3.1 Waveform parameters and ice concentration thresholds 38
3.2 Mean radar freeboard of gridded data for March and November 2013 . . . 50

4.1 List of linear trends along the ice-mass balance buoys 67

5.1 Mean freeboard values derived by the supervised procedure 94
5.2 Mean automatic procedure freeboard values for 2011 and 2013 104
5.3 Mean automatic procedure freeboard values binned into calendar month . 106

Bibliography

Aagaard, K. and Carmack, E.: The role of sea ice and other fresh water in the Arctic circulation, Journal of Geophysical Research: Oceans (1978–2012), 94, 14 485–14 498, 1989.

Alexandrov, V., Sandven, S., Wahlin, J., and Johannessen, O. M.: The relation between sea ice thickness and freeboard in the Arctic, The Cryosphere, 4, 373–380, doi: 10.5194/tc-4-373-2010, URL http://www.the-cryosphere.net/4/373/2010/, 2010.

Andersen, O. B.: The DTU10 Gravity field and Mean sea surface, second international symposium of the gravity field of the Earth (IGFS2), Fairbanks, Alaska, 2010.

Armitage, T. and Davidson, M.: Using the Interferometric Capabilities of the ESA CryoSat-2 Mission to Improve the Accuracy of Sea Ice Freeboard Retrievals, Geoscience and Remote Sensing, IEEE Transactions on, 52, 529–536, doi: 10.1109/TGRS.2013.2242082, 2014.

Arndt, S. and Nicolaus, M.: Seasonal cycle and long-term trend of solar energy fluxes through Arctic sea ice, The Cryosphere, 8, 2219–2233, doi: 10.5194/tc-8-2219-2014, URL http://www.the-cryosphere.net/8/2219/2014/, 2014.

Barber, D., Reddan, S., and LeDrew, E.: Statistical characterization of the geophysical and electrical properties of snow on landfast first-year sea ice, Journal of Geophysical Research: Oceans (1978–2012), 100, 2673–2686, 1995.

Barry, R., Serreze, M., Maslanik, J., and Preller, R.: The Arctic sea ice-climate system: Observations and modeling, Reviews of Geophysics, 31, 397–422, 1993.

Beaven, S. G., Lockhart, G. L., Gogineni, S. P., Hossetnmostafa, A. R., Jezek, K., Gow, A. J., Perovich, D. K., Fung, A. K., and Tjuatja, S.: Laboratory measurements of radar backscatter from bare and snow-covered saline ice sheets, International Journal of Remote Sensing, 16, 851–876, doi: 10.1080/01431169508954448, 1995.

Bintanja, R., Van Oldenborgh, G., Drijfhout, S., Wouters, B., and Katsman, C.: Important role for ocean warming and increased ice-shelf melt in Antarctic sea-ice expansion, Nature Geoscience, 6, 376–379, 2013.

Bouzinac, C.: CryoSat Product Handbook, ESA, UCL, URL https://earth.esa.int/documents/10174/125272/CryoSat_Product_Handbook, 2012.

Bretherton, F. P., Davis, R. E., and Fandry, C.: A technique for objective analysis and design of oceanographic experiments applied to MODE-73, in: Deep Sea Research and Oceanographic Abstracts, vol. 23, pp. 559–582, Elsevier, 1976.

Brodzik, M. J., Billingsley, B., Haran, T., Raup, B., and Savoie, M. H.: EASE-Grid 2.0: Incremental but Significant Improvements for Earth-Gridded Data Sets, ISPRS International Journal of Geo-Information, 1, 32–45, doi: 10.3390/ijgi1010032, URL http://www.mdpi.com/2220-9964/1/1/32, 2012.

Budikova, D.: Role of Arctic sea ice in global atmospheric circulation: A review, Global and Planetary Change, 68, 149 – 163, doi: http://dx.doi.org/10.1016/j.gloplacha.2009.04.001, URL http://www.sciencedirect.com/science/article/pii/S0921818109000654, 2009.

Colbeck, S. C.: An overview of seasonal snow metamorphism, Reviews of Geophysics, 20, 45–61, doi: 10.1029/RG020i001p00045, URL http://dx.doi.org/10.1029/RG020i001p00045, 1982.

Comiso, J. C.: A rapidly declining perennial sea ice cover in the Arctic, Geophys. Res. Lett., 29, doi: 10.1029/2002GL015650, URL http://dx.doi.org/10.1029/2002GL015650, 2002.

Comiso, J. C.: Large decadal decline of the Arctic multiyear ice cover, Journal of Climate, 25, 1176–1193, 2012.

Comiso, J. C. and Hall, D. K.: Climate trends in the Arctic as observed from space, Wiley Interdisciplinary Reviews: Climate Change, 5, 389–409, 2014.

Comiso, J. C., Parkinson, C. L., Gersten, R., and Stock, L.: Accelerated decline in the Arctic sea ice cover, Geophysical Research Letters, 35, URL http://www.agu.org/pubs/crossref/2008/2007GL031972.shtml, 2008.

Connor, L. N., Laxon, S. W., Ridout, A. L., Krabill, W. B., and McAdoo, D. C.: Comparison of Envisat radar and airborne laser altimeter measurements over Arctic sea ice, Remote Sensing of Environment, 113, 563 – 570, doi: 10.1016/j.rse.2008.10.015, 2009.

Cox, G. F. N. and Weeks, W. F.: Equations for Determining the Gas and Brine Volumes in Sea Ice Samples, J. Glaciology, 29, 306–316, 1982.

Cullen, R., Davidson, M. W. J., Drinkwater, M. R., Francis, C. R., Haas, C., Hawley, R. L., Mavrocordatos, C. M., Morris, E. M., Rack, W., Ratier, G., Viau, P., and Wingham, D. J.: Esa's New Range Of Radar Altimeters For The Extraction Of Geophysical Parameters From Land, Sea Ice And Ocean Surfaces, in: Proceedings of the Symposium on 15 Years of Progress in Radar Altimetry, 507, ESA, 2006.

Curry, J. A., Schramm, J. L., and Ebert, E. E.: Sea ice-albedo climate feedback mechanism, Journal of Climate, 8, 240–247, 1995.

Dempsey, D., Langhorne, P., Robinson, N., Williams, M., Haskell, T., and Frew, R.: Observation and modeling of platelet ice fabric in McMurdo Sound, Antarctica, Journal of Geophysical Research: Oceans (1978–2012), 115, 2010.

Doble, M.: Report on altimeter sea-ice thickness errors due to ice type, geometry and snow pack effects, Access, Arctic Climate Change, Economy and Society, 2014.

Drinkwater, M. R.: Ku band airborne radar altimeter observations of marginal sea ice during the 1984 Marginal Ice Zone Experiment, Journal of Geophysical Research: Oceans, 96, 4555–4572, doi: 10.1029/90JC01954, URL `http://dx.doi.org/10.1029/90JC01954`, 1991.

Drinkwater, M. R., Francis, R., Ratier, G., and Wingham, D. J.: The European Space Agency's earth explorer mission CryoSat: measuring variability in the cryosphere, Annals of Glaciology, 39, 313–320, 2004.

Eastwood, S.: OSI SAF Sea Ice Product Manual, v3.8 edn., URL `http://osisaf.met.no`, 2012.

Eicken, H.: From the Microscopic, to the Macroscopic, to the Regional Scale: Growth, Microstructure and Properties of Sea Ice, in: Sea Ice, pp. 22–81, Blackwell Science Ltd, doi: 10.1002/9780470757161.ch2, 2008.

ESA: CryoSat Mission and Data Description, ESA, 2007.

Fedotov, V., Cherepanov, N., and Tyshko, K.: Some features of the growth, structure and metamorphism of East Antarctic landfast sea ice, Wiley Online Library, 1998.

Fernández-Méndez, M., Wenzhöfer, F., Peeken, I., Sørensen, H. L., Glud, R. N., and Boetius, A.: Composition, Buoyancy Regulation and Fate of Ice Algal Aggregates in the Central Arctic Ocean, PloS one, 9, e107 452, 2014.

Fieguth, P. W., Karl, W. C., Willsky, A. S., and Wunsch, C.: Multiresolution optimal interpolation and statistical analysis of TOPEX/POSEIDON satellite altimetry, Geoscience and Remote Sensing, IEEE Transactions on, 33, 280–292, 1995.

Flanner, M., Shell, K., Barlage, M., Perovich, D., and Tschudi, M.: Radiative forcing and albedo feedback from the Northern Hemisphere cryosphere between 1979 and 2008, Nature Geoscience, 4, 151–155, 2011.

Forsberg, R., Keller, K., and Jacobsen, S.: Airborne lidar measurements for Cryosat validation, in: Geoscience and Remote Sensing Symposium, 2002. IGARSS '02. 2002 IEEE International, vol. 3, pp. 1756 – 1758, doi: 10.1109/IGARSS.2002.1026244, 2002.

Fraser, A. D., Massom, R. A., Michael, K. J., Galton-Fenzi, B. K., and Lieser, J. L.: East antarctic landfast sea ice distribution and variability, 2000-08, Journal of Climate, 25, 1137–1156, 2012.

Gautier, D. L., Bird, K. J., Charpentier, R. R., Grantz, A., Houseknecht, D. W., Klett, T. R., Moore, T. E., Pitman, J. K., Schenk, C. J., Schuenemeyer, J. H., et al.: Assessment of undiscovered oil and gas in the Arctic, Science, 324, 1175–1179, 2009.

Giles, K., Laxon, S., Wingham, D., Wallis, D., Krabill, W., Leuschen, C., McAdoo, D., Manizade, S., and Raney, R.: Combined airborne laser and radar altimeter measurements over the Fram Strait in May 2002, Remote Sensing of Environment, 111, 182 – 194, doi: 10.1016/j.rse.2007.02.037, URL `http://www.sciencedirect.com/science/article/pii/S0034425707002817`, remote Sensing of the Cryosphere Special Issue, 2007.

Giles, K. A., Laxon, S. W., and Ridout, A. L.: Circumpolar thinning of Arctic sea ice following the 2007 record ice extent minimum, Geophysical Research Letters, 35, L22 502, doi: 10.1029/2008GL035710, URL `http://dx.doi.org/10.1029/2008GL035710`, 2008.

Gloersen, P., Campbell, W. J., Cavalieri, D. J., Comiso, J. C., Parkinson, C. L., and Zwally, H. J.: Satellite passive microwave observations and analysis of Arctic and Antarctic sea ice, 1978-1987, Annals of Glaciology, 17, 1993.

Goodison, B. E., Brown, R. D., and Crane, R. G.: Cryospheric systems, in: EOS Science Plan: The State of Science in the EOS Program (NASA NP-1998-12-069-GSFC), edited by King, M., chap. 6, pp. 261–307, NASA Goddard Space Flight Center, Greenbelt, MD, 1999.

Gough, A. J., Mahoney, A. R., Langhorne, P. J., Williams, M. J., Robinson, N. J., and Haskell, T. G.: Signatures of supercooling: McMurdo Sound platelet ice, Journal of Glaciology, 58, 38–50, 2012.

Gow, A., Ackley, S., Govoni, J., and Weeks, W.: Physical and Structural Properties of Land-Fast Sea Ice in Mcmurdo Sound, Antarctica, Wiley Online Library, 1998.

Haas, C.: Dynamics versus Thermodynamics: The Sea Ice Thickness Distribution, in: Sea Ice, edited by Thomas, D. N. and Diekmann, G. S., vol. 2, chap. 4, pp. 113–151, Wiley-Blackwell, 2009.

Haas, C., Hendricks, S., Eicken, H., and Herber, A.: Synoptic airborne thickness surveys reveal state of Arctic sea ice cover, Geophysical Research Letters, 37, L09 501, doi: 10.1029/2010GL042652, URL http://dx.doi.org/10.1029/2010GL042652, 2010.

Hallikainen, M. and Winebrenner, D.: The physical basis for sea ice remote sensing, in: Microwave Remote Sensing of Sea Ice, edited by Carsey, F., pp. 29–46, American Geophysical Union, Washington, DC, USA, 1992.

Hallikainen, M., Ulaby, F., and Abdelrazik, M.: Dielectric properties of snow in the 3 to 37 GHz range, Antennas and Propagation, IEEE Transactions on, 34, 1329 – 1340, doi: 10.1109/TAP.1986.1143757, 1986.

Hawkins, J. D. and Lybanon, M.: GEOSAT altimeter sea-ice mapping, Oceanic Engineering, IEEE Journal of, 14, 139–148, 1989.

Heine, A. J.: Ice breakout around the southern end of Ross Island, Antarctica, New Zealand Journal of Geology and Geophysics, 6, 395–401, 1963.

Hellmer, H.: Impact of Antarctic ice shelf basal melting on sea ice and deep ocean properties, Geophysical Research Letters, 31, 2004.

Helm, V.: Airborne SAR/Interferometric Radar Altimeter System (ASIRAS) - Kalibrierung, Validierung und Interpretation der Messergebnisse, Ph.D. thesis, Universität Bremen, 2008.

Helm, V., Humbert, A., and Miller, H.: Elevation and elevation change of Greenland and Antarctica derived from CryoSat-2, The Cryosphere, 8, 1539–1559, doi: 10.5194/tc-8-1539-2014, URL http://www.the-cryosphere.net/8/1539/2014/, 2014.

Hendricks, S.: Validierung von altimetrischen Meereisdickenmessungen mit einem helikopter-basierten elektronischen Induktionsverfahren, Ph.D. thesis, Universität Bremen, 2009.

Hendricks, S., Stenseng, L., Helm, V., and Haas, C.: Effects of Surface Roughness on Sea Ice Freeboard Retrieval with an Airborne Ku-Band SAR Radar Altimeter, in: Geoscience and Remote Sensing (IGARSS 2010), IEEE International Symposium, 2010.

Hendricks, S., Ricker, R., and Helm, V.: CryoSat-2 Meereisprodukt, URL http://www.meereisportal.de/de/datenportal/karten_und_datenarchiv/, 2013.

Ho, J.: The implications of Arctic sea ice decline on shipping, Marine Policy, 34, 713–715, 2010.

Holland, P. R., Bruneau, N., Enright, C., Losch, M., Kurtz, N. T., and Kwok, R.: Modeled Trends in Antarctic Sea Ice Thickness, Journal of Climate, 27, 3784–3801, 2014.

Huntemann, M., Heygster, G., Kaleschke, L., Krumpen, T., Mäkynen, M., and Drusch, M.: Empirical sea ice thickness retrieval during the freeze-up period from SMOS high incident angle observations, The Cryosphere, 8, 439–451, doi: 10.5194/tc-8-439-2014, URL http://www.the-cryosphere.net/8/439/2014/, 2014.

Iacozza, J. and Barber, D. G.: An examination of the distribution of snow on sea,Äêice, Atmosphere-Ocean, 37, 21–51, doi: 10.1080/07055900.1999.9649620, URL http://dx.doi.org/10.1080/07055900.1999.9649620, 1999.

Jeffries, M., Weeks, W., Shaw, R., and Morris, K.: Structural Characteristics of Congelation and Platelet Ice and Their Role in the Development of Antarctic Land-Fast Sea-Ice, Journal of Glaciology, 39, 223–238, 1993.

Kaleschke, L. and Ricker, R.: Sea Ice Thickness from CryoSat-2 and SMOS, URL http://www.arcus.org/files/search/sea-ice-outlook/2013/07/pdf/regional/kaleschke_rickert.pdf, 2012.

Kaleschke, L., Tian-Kunze, X., Maaß, N., Mäkynen, M., and Drusch, M.: Sea ice thickness retrieval from SMOS brightness temperatures during the Arctic freeze-up period, Geophysical Research Letters, 39, 2012.

Kauker, F., Kaminski, T., Karcher, M., Giering, R., Gerdes, R., and Voßbeck, M.: Adjoint analysis of the 2007 all time Arctic sea-ice minimum, Geophysical Research Letters, 36, n/a–n/a, doi: 10.1029/2008GL036323, URL http://dx.doi.org/10.1029/2008GL036323, 2009.

Kurtz, N. and Markus, T.: Satellite observations of Antarctic sea ice thickness and volume, Journal of Geophysical Research: Oceans (1978–2012), 117, 2012.

Kurtz, N., Studinger, M. S., Harbeck, J., Onana, V., , and Farrell, S.: IceBridge Sea Ice Freeboard, Snow Depth, and Thickness in the Lincoln Sea, Northern Hemisphere, Tech. rep., Boulder, Colorado USA: NASA DAAC at the National Snow and Ice Data Center, 2012, updated 2014.

Kurtz, N., Studinger, M. S., Harbeck, J., Onana, V., and Farrell, S.: IceBridge Sea Ice Freeboard, Snow Depth, and Thickness. Arctic Ocean, Tech. rep., NASA National Snow and Ice Data Center Distributed Active Archive Center, Boulder, Colorado USA, URL http://dx.doi.org/10.5067/7XJ9HRV50O57, 2012, updated 2014.

Kurtz, N. T. and Farrell, S. L.: Large-scale surveys of snow depth on Arctic sea ice from Operation IceBridge, Geophysical Research Letters, 38, L20 505, URL http://dx.doi.org/10.1029/2011GL049216, 2011.

Kurtz, N. T., Farrell, S. L., Studinger, M., Galin, N., Harbeck, J. P., Lindsay, R., Onana, V. D., Panzer, B., and Sonntag, J. G.: Sea ice thickness, freeboard, and snow depth products from Operation IceBridge airborne data, The Cryosphere, 7, 1035–1056, doi: 10.5194/tc-7-1035-2013, URL http://www.the-cryosphere.net/7/1035/2013/, 2013.

Kurtz, N. T., Galin, N., and Studinger, M.: An improved CryoSat-2 sea ice freeboard retrieval algorithm through the use of waveform fitting, The Cryosphere, 8, 1217–1237, doi: 10.5194/tc-8-1217-2014, URL http://www.the-cryosphere.net/8/1217/2014/, 2014.

Kwok, R.: Simulated effects of a snow layer on retrieval of CryoSat-2 sea ice freeboard, Geophysical Research Letters, 41, 5014–5020, doi: 10.1002/2014GL060993, URL http://dx.doi.org/10.1002/2014GL060993, 2014.

Kwok, R., Zwally, H. J., and Yi, D.: ICESat observations of Arctic sea ice: A first look, Geophysical Research Letters, 31, 2004.

Kwok, R., Cunningham, G. F., Zwally, H. J., and Yi, D.: Ice, Cloud, and land Elevation Satellite (ICESat) over Arctic sea ice: Retrieval of freeboard, Journal of Geophysical Research: Oceans, 112, n/a–n/a, doi: 10.1029/2006JC003978, URL http://dx.doi.org/10.1029/2006JC003978, 2007.

Kwok, R., Cunningham, G. F., Wensnahan, M., Rigor, I., Zwally, H. J., and Yi, D.: Thinning and volume loss of the Arctic Ocean sea ice cover: 2003-2008, J. Geophys. Res., 114, doi: 10.1029/2009JC005312, 2009.

Laxon, S.: Sea ice altimeter processing scheme at the EODC, International Journal of Remote Sensing, 15, 915–924, doi: 10.1080/01431169408954124, URL http://www.tandfonline.com/doi/abs/10.1080/01431169408954124, 1994.

Laxon, S., Peacock, N., and Smith, D.: High interannual variability of sea ice thickness in the Arctic region, Nature, 425, 947–950, 2003.

Laxon, S. W., Giles, K. A., Ridout, A. L., Wingham, D. J., Willatt, R., Cullen, R., Kwok, R., Schweiger, A., Zhang, J., Haas, C., Hendricks, S., Krishfield, R., Kurtz, N., Farrell, S., and Davidson, M.: CryoSat-2 estimates of Arctic sea ice thickness and volume, Geophysical Research Letters, 40, 732–737, doi: 10.1002/grl.50193, URL http://dx.doi.org/10.1002/grl.50193, 2013.

Lemke, P., Ren, J., Alley, R. B., Allison, I., Carrasco, J., Flato, G., Fujii, Y., Kaser, G., Mote, P., Thomas, R. H., et al.: Observations: Changes in snow, ice and frozen ground., in: Climate change 2007: the physical science basis; summary for policymakers, technical summary and frequently asked questions. Part of the Working Group I contribution to the Fourth Assessment Report of the Intergovernmental Panel on Climate Change, pp. 337–383, Intergovernmental Panel on Climate Change, 2007.

Leonard, G., Purdie, C., Langhorne, P., Haskell, T., Williams, M., and Frew, R.: Observations of platelet ice growth and oceanographic conditions during the winter of 2003 in McMurdo Sound, Antarctica, Journal of Geophysical Research: Oceans (1978–2012), 111, 2006.

Leppäranta, M.: A review of analytical models of sea-ice growth, Atmosphere-Ocean, 31, 123–138, 1993.

Lindsay, R. and Schweiger, A.: Arctic sea ice thickness loss determined using subsurface, aircraft, and satellite observations, The Cryosphere, 9, 269–283, doi: 10.5194/tc-9-269-2015, URL `http://www.the-cryosphere.net/9/269/2015/`, 2015.

Lubin, D. and Massom, R.: Polar Remote Sensing, in: Atmosphere and Oceans, vol. 1, Praxis Publishing, 2006.

Maaß, N., Kaleschke, L., Tian-Kunze, X., and Drusch, M.: Snow thickness retrieval over thick Arctic sea ice using SMOS satellite data, The Cryosphere, 7, 1971–1989, doi: 10.5194/tc-7-1971-2013, URL `http://www.the-cryosphere.net/7/1971/2013/`, 2013.

Mahoney, A. R., Gough, A. J., Langhorne, P. J., Robinson, N. J., Stevens, C. L., Williams, M. M., and Haskell, T. G.: The seasonal appearance of ice shelf water in coastal Antarctica and its effect on sea ice growth, Journal of Geophysical Research: Oceans (1978–2012), 116, 2011.

Makynen, M. and Hallikainen, M.: Simulation of ASIRAS Altimeter Echoes for Snow-Covered First-Year Sea Ice, Geoscience and Remote Sensing Letters, IEEE, 6, 486 –490, doi: 10.1109/LGRS.2009.2015968, 2009.

Markus, T., C., J., Stroeve, ., and Miller3, J.: Recent changes in Arctic sea ice melt onset, freezeup, and melt season length, Journal Of Geophysical Research, 114, 2009.

Massom, R., Harris, P., Michael, K. J., and Potter, M.: The distribution and formative processes of latent-heat polynyas in East Antarctica, Annals of Glaciology, 27, 420–426, 1998.

Massom, R. A., Eicken, H., Haas, C., Jeffries, M. O., Drinkwater, M. R., Sturm, M., Worby, A. P., Wu, X., Lytle, V. I., Ushio, S., Morris, K., Reid, P. A., Warren, S. G., and Ian Allison: Snow On Antarctic Sea Ice, Reviews of Geophysics, 39, 413–445, 2001.

Massonnet, F., Mathiot, P., Fichefet, T., Goosse, H., König Beatty, C., Vancoppenolle, M., and Lavergne, T.: A model reconstruction of the Antarctic sea ice thickness and volume changes over 1980–2008 using data assimilation, Ocean Modelling, 64, 67–75, 2013.

Matzler, C. and Wegmuller, U.: Dielectric properties of freshwater ice at microwave frequencies, Journal of Physics D Applied Physics, 20, 1623–1630, doi: 10.1088/0022-3727/20/12/013, 1987.

Mauritzen, C. and Häkkinen, S.: Influence of sea ice on the thermohaline circulation in the Arctic-North Atlantic Ocean, Geophysical Research Letters, 24, 3257–3260, 1997.

Maykut, G. A.: Energy exchange over young sea ice in the central Arctic, Journal of Geophysical Research: Oceans, 83, 3646–3658, doi: 10.1029/JC083iC07p03646, URL http://dx.doi.org/10.1029/JC083iC07p03646, 1978.

Maykut, G. A.: Large-scale heat exchange and ice production in the central Arctic, Journal of Geophysical Research: Oceans, 87, 7971–7984, doi: 10.1029/JC087iC10p07971, URL http://dx.doi.org/10.1029/JC087iC10p07971, 1982.

McIntosh, P. C.: Oceanographic data interpolation: Objective analysis and splines, Journal of Geophysical Research: Oceans (1978–2012), 95, 13 529–13 541, 1990.

Meier, W. N., Hovelsrud, G. K., van Oort, B. E., Key, J. R., Kovacs, K. M., Michel, C., Haas, C., Granskog, M. A., Gerland, S., Perovich, D. K., Makshtas, A., and Reist, J. D.: Arctic sea ice in transformation: A review of recent observed changes and impacts on biology and human activity, Reviews of Geophysics, 52, 185–217, doi: 10.1002/2013RG000431, URL http://dx.doi.org/10.1002/2013RG000431, 2014.

Nghiem, S. V., Rigor, I. G., Perovich, D. K., Clemente-Colón, P., Weatherly, J. W., and Neumann, G.: Rapid reduction of Arctic perennial sea ice, Geophysical Research Letters, 34, L19 504, doi: 10.1029/2007GL031138, URL http://dx.doi.org/10.1029/2007GL031138, 2007.

Nicolaus, M., Haas, C., and Willmes, S.: Evolution of first-year and second-year snow properties on sea ice in the Weddell Sea during spring-summer transition, Journal of Geophysical Research: Atmospheres, 114, n/a–n/a, doi: 10.1029/2008JD011227, URL http://dx.doi.org/10.1029/2008JD011227, 2009.

Nicolaus, M., Katlein, C., Maslanik, J., and Hendricks, S.: Changes in Arctic sea ice result in increasing light transmittance and absorption, Geophysical Research Letters, 39, 2012.

Ozsoy-Cicek, B., Ackley, S., Xie, H., Yi, D., and Zwally, J.: Sea ice thickness retrieval algorithms based on in situ surface elevation and thickness values for application to altimetry, Journal of Geophysical Research: Oceans, 118, 3807–3822, 2013.

Parkinson, C. L. and Cavalieri, D. J.: A 21 year record of Arctic sea-ice extents and their regional, seasonal and monthly variability and trends, Annals of Glaciology, 34, 441–446, 2002.

Parkinson, C. L. and Cavalieri, D. J.: Antarctic sea ice variability and trends, 1979–2010, The Cryosphere, 6, 871–880, doi: 10.5194/tc-6-871-2012, URL `http://www.the-cryosphere.net/6/871/2012/`, 2012.

Parkinson, C. L. and Comiso, J. C.: On the 2012 record low Arctic sea ice cover: Combined impact of preconditioning and an August storm, Geophysical Research Letters, 40, 1356–1361, doi: 10.1002/grl.50349, URL `http://dx.doi.org/10.1002/grl.50349`, 2013.

Peacock, N. R. and Laxon, S. W.: Sea surface height determination in the Arctic Ocean from ERS altimetry, Journal of Geophysical Research: Oceans, 109, C07 001, doi: 10.1029/2001JC001026, URL `http://dx.doi.org/10.1029/2001JC001026`, 2004.

Perovich, D., Richter-Menge, J., Elder, B., Arbetter, T., Claffey, K., and Polashenski, C.: Observing and understanding climate change: Monitoring the mass balance, motion, and thickness of Arctic sea ice, URL `http://IMB.crrel.usace.army.mil`, 2013.

Perovich, D. K.: The Optical Properties of Sea Ice., Tech. rep., DTIC Document, 1996.

Perovich, D. K., Grenfell, T. C., Light, B., and Hobbs, P. V.: Seasonal evolution of the albedo of multiyear Arctic sea ice, Journal of Geophysical Research: Oceans, 107, SHE 20–1–SHE 20–13, doi: 10.1029/2000JC000438, URL `http://dx.doi.org/10.1029/2000JC000438`, 2002.

Pfaffling, A., Haas, C., and Reid, J. E.: Direct helicopter EM — Sea-ice thickness inversion assessed with synthetic and field data, Geophysics, 72, F127–F137, doi: 10.1190/1.2732551, URL `http://geophysics.geoscienceworld.org/content/72/4/F127.abstract`, 2007.

Price, D., Rack, W., Haas, C., Langhorne, P. J., and Marsh, O.: Sea ice freeboard in McMurdo Sound, Antarctica, derived by surface-validated ICESat laser altimeter data, Journal of Geophysical Research: Oceans, 118, 3634–3650, 2013.

Price, D., Rack, W., Langhorne, P. J., Haas, C., Leonard, G., and Barnsdale, K.: The sub-ice platelet layer and its influence on freeboard to thickness conversion of Antarctic sea ice, The Cryosphere, 8, 1031–1039, doi: 10.5194/tc-8-1031-2014, URL `http://www.the-cryosphere.net/8/1031/2014/`, 2014.

Purdie, C. R., Langhorne, P. J., Leonard, G. H., and Haskell, T. G.: Growth of first-year landfast Antarctic sea ice determined from winter temperature measurements, Annals of Glaciology, 44, 170–176, 2006.

Raney, R. K.: The delay/Doppler radar altimeter, Geoscience and Remote Sensing, IEEE Transactions on, 36, 1578–1588, 1998.

Rey, L., de Chateau-Thierry, P., Phalippou, L., Mavrocordatos, C., and Francis, R.: SIRAL, a high spatial resolution radar altimeter for the Cryosat mission, in: Geoscience and Remote Sensing Symposium, 2001. IGARSS '01. IEEE 2001 International, vol. 7, pp. 3080–3082, doi: 10.1109/IGARSS.2001.978261, 2001.

Richter-Menge, J. A., Perovich, D. K., Elder, B. C., Claffey, K., Rigor, I., and Ortmeyer, M.: Ice mass-balance buoys: a tool for measuring and attributing changes in the thickness of the Arctic sea-ice cover, Annals of Glaciology, 44, 205–210, 2006.

Ricker, R., Hendricks, S., Helm, V., Gerdes, R., and Skourup, H.: Comparison of sea-ice freeboard and thickness distributions from aircraft data and Cryosat-2, in: Proceedings of Earth Observation and Cryosphere Science, edited by Ouwehand, L., ESA SP-712, ESA, 2013.

Ricker, R., Hendricks, S., Helm, V., Skourup, H., and Davidson, M.: Sensitivity of CryoSat-2 Arctic sea-ice freeboard and thickness on radar-waveform interpretation, The Cryosphere, 8, 1607–1622, doi: 10.5194/tc-8-1607-2014, URL `http://www.the-cryosphere.net/8/1607/2014/`, 2014a.

Ricker, R., Hendricks, S., Helm, V., Skourup, H., and Davidson, M.: Sensitivity of CryoSat-2 Arctic sea-ice volume trends on radar-waveform interpretation, The Cryosphere Discussions, 8, 1831–1871, doi: 10.5194/tcd-8-1831-2014, URL `http://www.the-cryosphere-discuss.net/8/1831/2014/`, 2014b.

Ridley, J. K. and Partington, K. C.: A model of satellite radar altimeter return from ice sheets, International Journal of Remote Sensing, 9, 601–624, doi: 10.1080/01431168808954881, 1988.

Rothrock, D. A., Yu, Y., and Maykut, G. A.: Thinning of the Arctic sea-ice cover, Geophys. Res. Lett., 26, 3469–3472, doi: 10.1029/1999GL010863, 1999.

Schwerdtfeger, P.: The thermal properties of sea ice, J. Glaciol, 4, 789–807, 1963.

Semtner Jr, A. J.: A model for the thermodynamic growth of sea ice in numerical investigations of climate, Journal of Physical Oceanography, 6, 379–389, 1976.

Serreze, M. C. and Barry, R. G.: Processes and impacts of Arctic amplification: A research synthesis, Global and Planetary Change, 77, 85 – 96, doi: http://dx.doi.org/10.1016/j.gloplacha.2011.03.004, URL `http://www.sciencedirect.com/science/article/pii/S0921818111000397`, 2011.

Serreze, M. C., Holland, M. M., and Stroeve, J.: Perspectives on the Arctic's shrinking sea-ice cover, science, 315, 1533–1536, 2007.

Smith, I., Langhorne, P., Frew, R., Vennell, R., and Haskell, T.: Sea ice growth rates near ice shelves, Cold Regions Science and Technology, 83, 57–70, 2012.

Stroeve, J., Serreze, M., Holland, M., Kay, J., Malanik, J., and Barrett, A.: The Arctic's rapidly shrinking sea ice cover: a research synthesis, Climatic Change, 110, 1005–1027, doi: 10.1007/s10584-011-0101-1, URL `http://dx.doi.org/10.1007/s10584-011-0101-1`, 2012.

Stroeve, J., Barrett, A., Serreze, M., and Schweiger, A.: Using records from submarine, aircraft and satellites to evaluate climate model simulations of Arctic sea ice thickness, The Cryosphere, 8, 1839–1854, 2014.

Sturm, M. and Massom, R. A.: Snow and Sea Ice, in: Sea Ice, edited by Thomas, D. N. and Diekmann, G. S., vol. 2, chap. 5, pp. 153–204, Wiley-Blackwell, 2009.

Sturm, M., Holmgren, J., and Perovich, D. K.: Winter snow cover on the sea ice of the Arctic Ocean at the Surface Heat Budget of the Arctic Ocean (SHEBA): Temporal evolution and spatial variability, Journal of Geophysical Research: Oceans, 107, SHE 23–1–SHE 23–17, doi: 10.1029/2000JC000400, URL `http://dx.doi.org/10.1029/2000JC000400`, 2002.

Thomas, D. and Dieckmann, G., eds.: Sea Ice, John Wiley & Sons, 2010.

Tiuri, M. E., Sihvola, A., Nyfors, E., and Hallikaiken, M.: The complex dielectric constant of snow at microwave frequencies, Oceanic Engineering, IEEE Journal of, 9, 377–382, doi: 10.1109/JOE.1984.1145645, 1984.

Tonboe, R., Andersen, S., and Pedersen, L.: Simulation of the Ku-band Radar altimeter sea ice effective scattering surface, Geoscience and Remote Sensing Letters, IEEE, 3, 237 – 240, doi: 10.1109/LGRS.2005.862276, 2006.

Ulaby, F., Moore, R., and Fung, A.: Microwave remote sensing: active and passive. Radar remote sensing and surface scattering and emission theory. Vol. II, Remote

sensing, Addison-Wesley Publishing Company, Advanced Book Program/World Science Division, 1981.

Ulaby, F. T., Moore, R. K., and Fung, A. K.: Physical mechanisms and empirical models for scattering and emission, in: Microwave remote sensing: active and passive. Vol. II: Radar remote sensing and surface scattering and emission theory, Addison-Wesley Publishing CompanyAdvanced Book Program/World Science Division, 1982.

Ulander, L. M.: Interpretation of Seasat radar-altimeter data over sea ice using near-simultaneous SAR imagery, International Journal of Remote Sensing, 8, 1679–1686, 1987.

Vaughan, D., Comiso, J., Allison, I., Carrasco, J., Kaser, G., Kwok, R., Mote, P., Murray, T., Paul, F., Ren, J., Rignot, E., Solomina, O., Steffen, K., and Zhang, T.: Observations: Cryosphere, in: Climate Change 2013: The Physical Science Basis. Contribution of Working Group I to the Fifth Assessment Report of the Intergovernmental Panel on Climate Change, edited by Stocker, T., Qin, D., Plattner, G.-K., Tignor, M., Allen, S., Boschung, J., Nauels, A., Xia, Y., Bex, V., and Midgley, P., Intergovernmental Panel on Climate Change, Cambridge University Press, Cambridge, United Kingdom and New York, NY, USA, 2013.

Wadhams, P., Tucker, W. B., I., Krabill, W. B., Swift, R. N., Comiso, J. C., and Davis, N. R.: Relationship Between Sea Ice Freeboard and Draft in the Arctic Basin, and Implications for Ice Thickness Monitoring, J. Geophys. Res., 97, 20 325–20 334, doi: 10.1029/92JC02014, 1992.

Warren, S. G., Rigor, I. G., Untersteiner, N., Radionov, V. F., Bryazgin, N. N., Aleksandrov, Y. I., and Colony, R.: Snow depth on Arctic sea ice, Journal of Climate, 12, 1814–1829, 1999.

Wilkin, J. L., Bowen, M. M., and Emery, W. J.: Mapping mesoscale currents by optimal interpolation of satellite radiometer and altimeter data, Ocean Dynamics, 52, 95–103, 2002.

Willatt, R. and Haas, C.: CryoVEx 2011 Alert Sea Ice Ground Team Report, Tech. rep., ESA, 2011.

Willatt, R., Giles, K., Laxon, S., Stone-Drake, L., and Worby, A.: Field Investigations of Ku-Band Radar Penetration Into Snow Cover on Antarctic Sea Ice, Geoscience and Remote Sensing, IEEE Transactions on, 48, 365 –372, doi: 10.1109/TGRS.2009.2028237, 2010.

Willatt, R., Laxon, S., Giles, K., Cullen, R., Haas, C., and Helm, V.: Ku-band radar penetration into snow cover on Arctic sea ice using airborne data, Annals of Glaciology, 52, 197–205, 2011.

Wingham, D., Phalippou, L., Mavrocordatos, C., and Wallis, D.: The mean echo and echo cross product from a beamforming interferometric altimeter and their application to elevation measurement, IEEE T. Geoscience and Remote Sensing, 42, 2305–2323, doi: 10.1109/TGRS.2004.834352, 2004.

Wingham, D., Francis, C., Baker, S., Bouzinac, C., Brockley, D., Cullen, R., de Chateau-Thierry, P., Laxon, S., Mallow, U., Mavrocordatos, C., Phalippou, L., Ratier, G., Rey, L., Rostan, F., Viau, P., and Wallis, D.: CryoSat: A mission to determine the fluctuations in Earth's land and marine ice fields, Advances in Space Research, 37, 841 – 871, doi: 10.1016/j.asr.2005.07.027, 2006.

Wingham, D. J., Rapley, C. G., and Griffiths, H.: New techniques in satellite altimeter tracking systems, in: Proceedings of the IGARSS Symposium, edited by Guyenne, T. and Hunt, J., vol. SP-254,, pp. 1339–1344, European Space Agency, 1986.

Xie, H., Tekeli, A. E., Ackley, S. F., Yi, D., and Zwally, H. J.: Sea ice thickness estimations from ICESat altimetry over the Bellingshausen and Amundsen Seas, 2003–2009, Journal of Geophysical Research: Oceans, 118, 2438–2453, 2013.

Yi, D., Zwally, H. J., and Robbins, J. W.: ICESat observations of seasonal and interannual variations of sea-ice freeboard and estimated thickness in the Weddell Sea, Antarctica (2003–2009), Annals of Glaciology, 52, 43–51, 2011.

Zwally, H. J., Yi, D., Kwok, R., and Zhao, Y.: ICESat measurements of sea ice freeboard and estimates of sea ice thickness in the Weddell Sea, J. Geophys. Res., 113, doi: 10.1029/2007JC004284, 2008.

Zwally, H. J. ; Comiso, J. C., Parkinson, C. L., Campbell, W. J., and Carsey, F. D.: Antarctic Sea Ice 1973-1976 from Satellite Passive Microwave Observations, NASA, Washington, DC, 1983.

Zygmuntowska, M., Khvorostovsky, K., Helm, V., and Sandven, S.: Waveform classification of airborne synthetic aperture radar altimeter over Arctic sea ice, The Cryosphere, 7, 1315–1324, doi: 10.5194/tc-7-1315-2013, URL `http://www.the-cryosphere.net/7/1315/2013/`, 2013.

Acknowledgements

I would like to express my gratitude to my supervisor Prof. Rüdiger Gerdes (AWI, head of the sea ice physics section, and Jacobs University). I am grateful for his support throughout my PhD project and the scientific freedom he left me.

I am grateful to Prof. Joachim Vogt (Jacobs University) that he agreed to be my second supervisor and for his suggestions during my committee meetings.

Special thanks go to Stefan Hendricks (AWI) as my first advisor for his great supervision throughout my PhD project. He supported me in any situation and his door was always open to drop in for a minute or longer. In addition he supplied me with many Ideas that substantially contributed to this work.

Veit Helm (AWI) as my second advisor helped me a lot to with his knowledge about radar altimetry and CryoSat-2. His processing chain for CryoSat-2 data over land ice have been the base for this work. Moreover, he helped me with IDL programming and many suggestions that substantially contributed to this work.

The Earth System Science Research School ESSReS allowed me to study in an interdisciplinary framework and offered me many valuable soft skill courses as well as financial support for conferences. Therefore I would like to thank Klaus Grosfeld, Helge Meggers and Stefanie Klebe and furthermore all PhD students of class II.

I would like to thank my former and present sea-ice physics colleagues, particularly Giulia Castellani, Valeria Selyuzhenok, Marcel Nicolaus, Priska Hunkeler, Stefanie Arndt, Thomas Krumpen, Polona Itkin, Sandra Schwegmann, Malte Thoma, Karel Castro-Morales, Ingrid Linck-Rosenhaim, Kathrin Riemann-Campe, Hiroshi Sumata, Frank Kauker, Martin Schiller, and many other AWI colleagues for a nice working atmosphere that made me always feeling comfortable.

Special thanks go to my close friends for their moral support and the nice time beyond the daily hustle.

And finally I would like to express my deepest gratitude to my family for their moral support and that they were there for me at any time during this period.

Statutory declaration

I, Robert Ricker, hereby declare that I have written this PhD thesis independently, unless where clearly stated otherwise. I have used only the sources, the data and the support that I have clearly mentioned. This PhD thesis has not been submitted for conferral of degree elsewhere.

I confirm that no rights of third parties will be infringed by the publication of this thesis.

Bremen, February 12, 2015

Signature _____